DEFORMATION–INDUCED AMORPHIZATION
OF CU–TI INTERMETALLICS

Thesis by
Philip Douglas Askenazy

In Partial Fulfillment of the Requirements
for the Degree of
Doctor of Philosophy

California Institute of Technology
Pasadena, California

1992

(Defended March 30, 1992)

To my parents, for their unwavering support,

and

To Wendy, for more than I can express

ACKNOWLEDGMENTS

I would first like to thank my advisor, Professor William L. Johnson, for his patience, understanding, uncanny intuition, and for showing me how science should, and should not, be done. He is truly an outstanding scientist. I would also like to thank Professors Brent Fultz and Channing Ahn for their frequent advice and help with much of this work. Dr. Eduardo Kamenetzky performed the TEM on the rolled ribbons, for which I am grateful. Thanks also go to Professor Tom Christman for his valuable insight on nanocrystals and deformation.

I would like to express my deep appreciation to Carol Garland for her invaluable assistance with all aspects of the microscopy of the wear samples. Her tireless dedication and great technical ability were invaluable to me, and enabled me to finish this thesis.

I am grateful to Professors Christopher Lobb and Michael Tinkham and Dr. Michael Tenhover for introducing me to solid state physics, and for their continual encouragement.

Many of my fellow graduate students, past and present, and others I have known here not only have helped me in many ways with my research, but also have made life at Caltech much more enjoyable. A partial list includes Micky Atzmon, Steve Anlage, Xian–Li Yeh, Bruce Clemens, Konrad Samwer, Young–Shil Kim, Gordon Han, Angela Bressan, Andy Mutz, Dave Lee, Doug Pearson, Chuck Krill, Mo Li, Joe Holzer, Jürgen Eckert, Yoshio Abe, Lawrence Anthony, Reiner Birringer, Pascal Yvon, Don Montgomery, Brooke Anderson, Ted Woodward, Sheri Smith, Warren Kibbe, Peter Fisher, Chris

Guske, Brad Woods, Jeffrey Pugh, Jeff Ulin, Joe J. Rushanan, the Caltech hockey team, and the Not the Garveys softball team. I value their friendship, and I am grateful to all of them.

Finally I would like to remember some coworkers. Although I only met him a dozen times, Art Williams could not have been more free with his advice and open with his friendship. Barry Krueger kept everyone on their toes on the third floor; his winning personality made the monthly GUSH something I will always remember. And Concetto Geremia was not only a great technician but also truly one of the most joyous and giving people I have known. I will miss them.

ABSTRACT

Two methods of inducing amorphization in Cu–Ti intermetallic compounds by mechanical means have been investigated. Ingots of compositions $Cu_{35}Ti_{65}$ and $Cu_{33.3}Ti_{66.7}$ were rapidly quenched into ribbons. The microstrucure consisted largely of microcrystals in an amorphous matrix, which were either quenched in or grown by annealing. The ribbons were cold–rolled, which reduced their effective thickness by a factor of about 8. The status of the intermetallic compound $CuTi_2$ was monitored by x–ray diffraction and transmission electron microscopy (TEM). The crystals were found to amorphize as rolling progressed. This behavior was not reproduced in polycrystalline samples that had no amorphous matrix present initially. The presence of the amorphous phase is thus necessary for amorphization of the crystal: it eliminates the need to nucleate the new glass, and it prevents the ribbon from disintegrating at high deformation stages. It may also change the deformation mechanism that occurs in the crystals, retarding the onset of amorphization. Diffuse scattering in close-packed directions is similar to that seen in electron irradiation experiments. It is postulated that the chemical disorder present in antiphase boundaries caused by deformation raises the free energy of the crystal higher than that of the amorphous phase.

Ingots of the same compound were worn against each other in a custom-built wear apparatus. The design eliminates iron contamination of the wear sample and requires relatively small quantities of material. Alteration of the surface structure was monitored by plane–view and cross–sectional TEM. Larger subsurface crystals exhibit diffuse scattering, similar to that found in the rolled samples. A wide range of grain sizes was observed, due to the inhomogeneous nature of the wear process. An unusual phase was observed at the surface, consisting of a nanometer–scale mixture of aligned nanocrystalline regions and disordered areas. Some amorphous phase is possibly present as well. It is postulated a combination of high unidirectional strain rates and small grain sizes forces the nanocrystals to accommodate deformation by disordering in one direction. Deformation in additional directions might presumably cause the structure to go completely amorphous.

CONTENTS

LIST OF FIGURES

Chapter One

Chapter Two

Chapter Three

CHAPTER ONE: Introduction and Background

1.1 Introduction

Amorphous materials, or glasses, are solids whose atoms do not form a periodic arrangement, as do those of crystals. Their structure more closely resembles that of a liquid; they have no long–range order. Figure 1.1 shows idealized structures of a gas, a liquid, a glass, and a crystal, accompanied by their typical x–ray scattering patterns. The gas exhibits no order whatsoever; its scattered intensity is uniform for all scattering angles, showing that the atoms are randomly distributed. The sharp peaks of the crystal reflect the long–range, periodic ordering of its atoms. The broad peaks of the liquid and amorphous solid suggest that there exists some short–range order of the atoms due to local bonding preferences; there is, however, no periodicity.

Some glasses occur naturally, such as obsidian. This is formed by the rapid cooling of magma when it is driven toward the earth's crust during volcanic activity. The cooling rate must be high enough so that the atoms are configurationally frozen; i.e., they don't have time to order themselves into a more stable crystalline array. Although prehistoric man was able to flake off pieces of obsidian for use as tools and weapons, it wasn't until a few thousand years ago that humans discovered that soda and lime reduce the melting point of silica, i.e., common sand, low enough for simple furnaces to reach. Silica (SiO_2) has another property our ancestors could not have known about: the atoms are covalently bonded together, slowing the rate at which they are able to rearrange into a crystalline configuration. In fact, the cooling rate needed

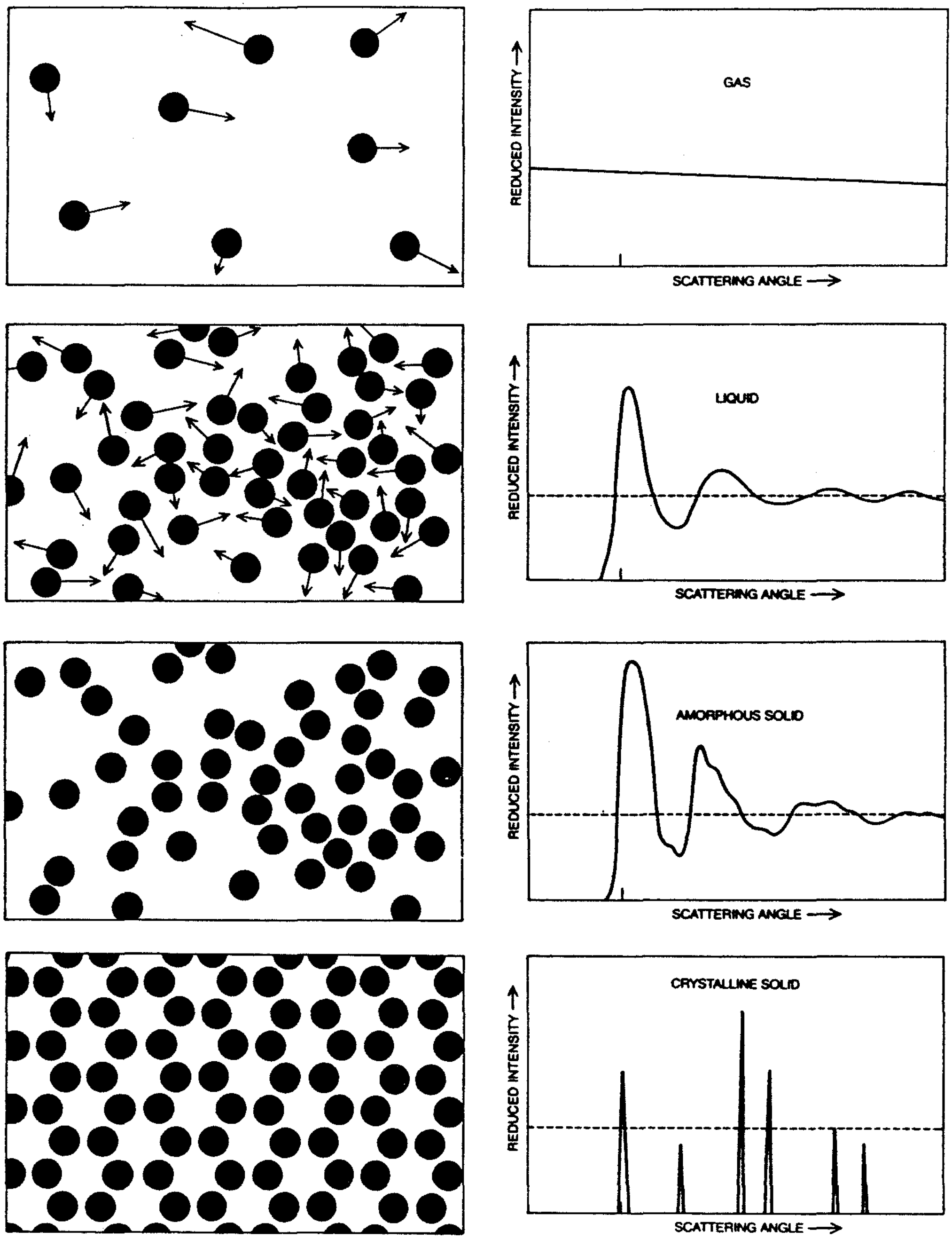

Figure 1.1. The atomic structures of a gas, a liquid, a glass, and a crystal, and their corresponding x–ray scattering patterns (taken from Ref. 1.1).

to prevent crystallization is only a few degrees per minute, achievable merely by letting the material cool in air. Furthermore, "room" temperature is low enough so that the atoms will effectively *never* rearrange. These facts resulted in the first manmade glass.

Just as oxide glasses have many desirable properties, scientists and engineers have discovered that many metallic glasses have improved characteristics over their crystalline counterparts, in such diverse areas as mechanical behavior, corrosion and wear resistance, and magnetic properties. However, synthesizing amorphous metals is a much more difficult undertaking. Metallic atoms rearrange far more quickly than those in oxides do; they are thus able to nucleate the crystalline phase far more easily than their oxide counterparts are able to. It wasn't until this century that techniques were developed to form metallic glasses. Rapid quenching techniques include vapor deposition (e.g., by sputtering) and liquid quenching (e.g., by melt spinning or splat quenching). Other methods of amorphizing crystals involve irradiating them with electrons, ions, or fast neutrons. In these cases, when the induced defects create enough disorder, some materials may amorphize. All of these techniques have a serious disadvantage, however: the samples produced must have one small dimension. (This is not true for neutron irradiation, but that method has other drawbacks instead.) Vapor quenching can produce only a thin film, while liquid quenching must rely on a ribbon or foil being sufficiently thin to allow rapid enough cooling to avoid crystallization. And electron and ion irradiation affect only the surface of the sample.

Within the last ten years, a new method of amorphizing metals has been developed. It employs an isothermal solid state reaction via interdiffusion of two (or more) elements. It also kinetically bypasses crystallization, but in a manner different from rapid quenching. Although the elemental layers must be thin, certain deformation methods have been shown to accomplish this while still producing a relatively large final sample. As an extension of this discovery, the present work represents one of the first reported attempts to amorphize intermetallic compounds, without utilizing interdiffusion, by mechanical means. Previously, irradiation was the only method of achieving this. Concurrently, mechanical alloying has succeeded in accomplishing this as well. It is a complementary technique to the two presented in this thesis: cold–rolling and wear. It is hoped that study of such deformation techniques will lead to the formation of bulk metallic glasses.

This chapter presents information regarding thermodynamics and kinetics of metallic glass formation, as well as a description of the system investigated. The second chapter describes the cold–rolling experiments and discusses the results obtained. Chapter three provides an introduction to wear processes, a description of the wear experiment, and the results thereof. Chapter four contains conclusions and suggestions for future research.

1.2 Rapid Quenching

The first modern study of metallic glass formation involved quenching metallic vapors onto a cryogenically cooled substrate.[1.2] The amorphous films thus produced were characterized by *in–situ* electron diffraction. However, these particular glasses crystallized far below room temperature. Five years later, Duwez et al.[1.3] rapidly quenched the first amorphous alloy from the liquid state. Their technique, in which a "gun" sprayed droplets of molten alloy onto a copper plate at room temperature, produced effective cooling rates of at least 10^6 °K/sec, fast enough to kinetically bypass crystal nucleation. Since then, many methods utilizing rapid quenching have been developed. Vapor quenching onto a cold substrate has an effective cooling rate of up to 10^{13} °K/sec., since deposition occurs atom by atom, and heat is removed rapidly through a thin film.[1.4] Laser melting, in which a picosecond laser pulse melts a thin surface layer of a solid (which then rapidly cools by conducting heat into the bulk), can achieve cooling rates of 10^{12} °K/sec.[1.5] Splat quenching, which consists of a copper piston and anvil smashing a molten drop of alloy between them, produces quench rates of 10^7–10^9 °K/sec, depending on the thickness of the resulting foil. And melt–spinning, in which a stream of liquid is forced onto a rapidly rotating copper wheel, can effect quench rates on the order of 10^6 °K/sec. The lower rates are sufficient to amorphize binary alloys in the vicinity of eutectic compositions.[1.6] The composition range can be extended by increasing the quench rate. The highest rates are necessary to form amorphous elemental metals, which are highly unstable, and crystallize readily at temperatures as low as tens of degrees Kelvin.

All of these techniques require cooling of the melt quickly enough to avoid nucleation of the more stable crystalline phase. The kinetics involved can be visualized best by use of a time–temperature–transformation (TTT) curve, as depicted in Figure 1.2. The solid curve represents the time required at a given temperature for a small (arbitrarily chosen) fraction of undercooled liquid to transform to a crystalline phase. (This is usually calculated for

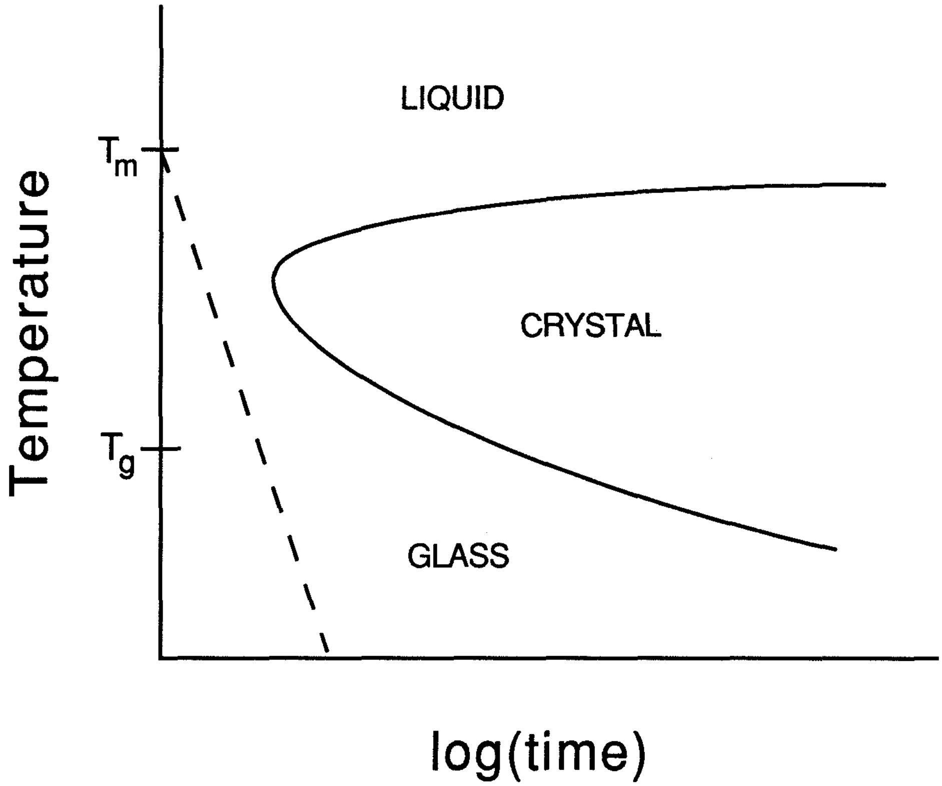

Figure 1.2. TTT curve representing a rapid solidification experiment. The slope of the dashed line (i.e., the cooling rate) must be steep enough to avoid crystallization. T_m is the melting point and T_g is the glass transition temperature (after Ref. 1.7).

isothermal anneals; dynamic heat treatments require a continuous–cooling-transformation diagram. The only difference of the latter from a TTT diagram, however, is a small shift of the curve to the right, i.e., toward longer time.) The dashed line represents a typical cooling curve for rapid quenching. The slope, or quench rate, must be steep enough to avoid the nose of the transformation curve, thus bypassing crystallization.

The shape of the TTT curve is due to the competition of kinetic and thermodynamic factors. At low temperatures, diffusion and atomic jump rates are low, increasing the time required for transformation. At temperatures near T_m the difference in Gibbs free energies of the liquid and solid, which is the thermodynamic driving force for the transformation, becomes quite small, slowing down the reaction as well. Thus at some temperature there is a maximum in the crystallization rate. For a detailed derivation of the TTT curve[1.8] see Appendix A.

1.3 Solid State Reactions

In rapid quenching, crystallization is kinetically bypassed by an extremely high cooling rate. It was recently found that in certain binary (or ternary) systems which contain one fast–diffusing component, equilibrium compound formation can also be bypassed by interdiffusion near room temperature. The first detailed experiment to demonstrate this involved hydriding the fcc solution Zr_3Rh; rather than phase separating into the two equilibrium crystalline phases ZrH_2 and Rh as expected, the system formed amorphous $(Zr_3Rh)H_{1.4}$ instead.[1.9] Soon after, in the first paper to explain the phenomenon, crystalline Au and La multilayers were reacted at 70° C to form an amorphous alloy.[1.10] Many binary systems have now been found to exhibit this behavior; for a comprehensive review of these (and amorphization in general), see Johnson.[1.11]

Amorphization in the latter experiment was explained by use of a free energy diagram, shown in Figure 1.3. The dotted line represents the average starting free energy of the unreacted elemental Au (α) and La (β) layers. The free energy of the amorphous phase (the solid curve) was calculated using Miedema's method.[1.12] Due to their large negative heat of mixing, when the elements interdiffuse they can lower the free energy of the system by forming a glass. The equilibrium intermetallic compounds are represented by γ, δ, and ϵ; being more stable, they occur at a lower free energy than that of the glass. The dashed lines represent the common tangents of the glassy free energy curve and those of the pure elements, and thus define two–phase regions where elemental Au or La exist in metastable equilibrium with the amorphous phase. These regions were observed experimentally and are indicated in the figure.

Extension of such solid state reactions to bulk glass production was accomplished by co–deforming layered alternating elemental foils in a rolling mill.[1.13] Such deformation was beneficial in three ways. First, it reduced the average layer thicknesses to the sub–micron range, allowing solid state amorphization to occur during subsequent annealing. Second, fresh interfaces were created throughout the sample, greatly facilitating the reaction. Third, in some cases, deformation caused enough intermixing at the interfaces to induce amorphization without subsequent annealing. The first two (at least) also occur during mechanical alloying of elemental powders.[1.14–1.16] The high

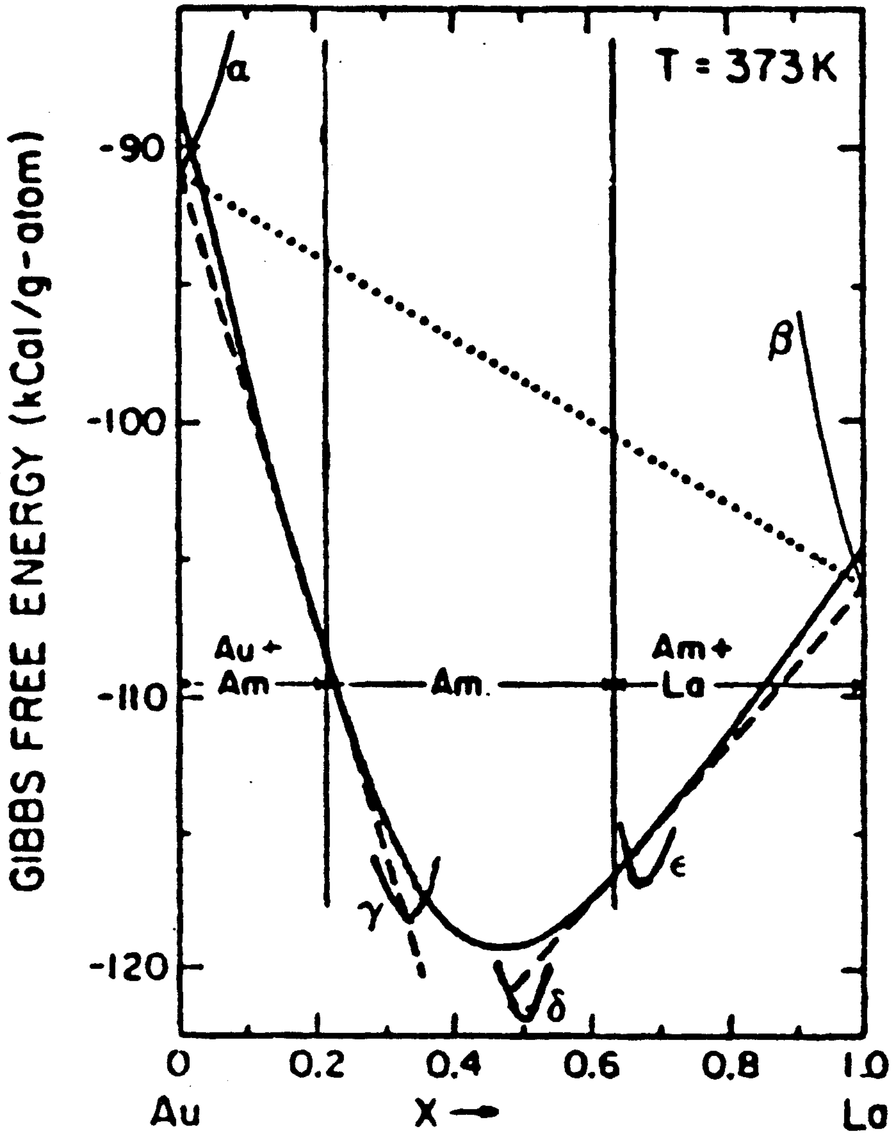

Figure 1.3. Free energy diagram of the solid state amorphization reaction of Au (α) and La (β) crystalline multilayers. The dotted line is the average free energy of the unreacted sample; the solid curve is the free energy of the amorphous phase. Equilibrium intermetallic compounds are γ, δ, and ϵ. Two–phase regions are indicated (taken from Ref. 1.10).

local temperatures produced by this method increase the mobility of the fast–diffusing species enough to complete the reaction without requiring subsequent annealing. This will be discussed in more detail in Section 1.4.2.

In such solid state reactions intermetallic compound formation is thermodynamically favored over glass formation; however, it is suppressed by kinetic constraints. Kinetically, amorphization occurs because one of the components in the system diffuses quickly enough to intermix the elements, at temperatures too low either for the long range diffusion necessary for phase separation to occur (as in the case of the Zr–Rh hydride), or for the crystalline phase to nucleate (as observed in the Au–La system). However, in the latter case, growth of the amorphous phase requires diffusion over distances much greater than the size of a crystalline nucleus. This apparent discrepancy has been explained by noticing that in glass forming systems, only one component actually diffuses; the other(s) remain relatively motionless.[1.11] It was postulated that crystal nucleation requires mobility of both species, not just one. Also, it has been suggested that homogeneous crystal nucleation is suppressed in environments with sharp concentration gradients, such as those that exist in multilayer solid state amorphization reactions.[1.40] In addition, it has been observed that the amorphous phase nucleates heterogeneously on grain boundaries.[1.11] This may occur more easily for the glass than for an intermetallic due to the former's lack of crystallographic constraints for forming a low energy interface with the original crystalline elements.

In the above experiments there is a kinetic "window" in which diffusion-driven amorphization can occur, obtained, for example, by comparing the relative interdiffusion rates of the component species. This window depends on the temperature at which the reaction takes place; if the temperature is raised to the point where an equilibrium intermetallic phase is able to nucleate, then the window disappears entirely. This temperature window was observed in the Au–La experiment,[1.10] and is represented by the shaded area of the hypothetical TTT diagram in Figure 1.4. At high enough temperatures, an isothermal reaction will lead to equilibrium compound formation. At intermediate temperatures, kinetic suppression of crystal nucleation results in formation of the amorphous phase. And at low temperatures, diffusion is too slow for any reaction to occur.

1.4 Amorphization of Intermetallic Compounds

In the last section the discussion centered on solid state reactions that are chemically driven. There has also been much work done on amorphizing crystals in the solid state without requiring long range diffusion. Elemental metals are for the most part too stable to be of more than limited interest; intermetallic compounds have thus been the most extensively studied. Figure 1.5 presents schematic free energy curves illustrating the amorphization of an intermetallic compound. In Figure 1.5a the equilibrium compound is situated below the metastable glass curve by an amount equal to the free energy of crystallization ΔG_{a-x}. By increasing the defect energy stored in the crystal by some means (e.g., irradiation or mechanical work), its free energy is hypothetically raised higher than that of the glass, as shown in Figure 1.5b. It is at this point thermodynamically favorable for the crystal to transform into the amorphous phase.

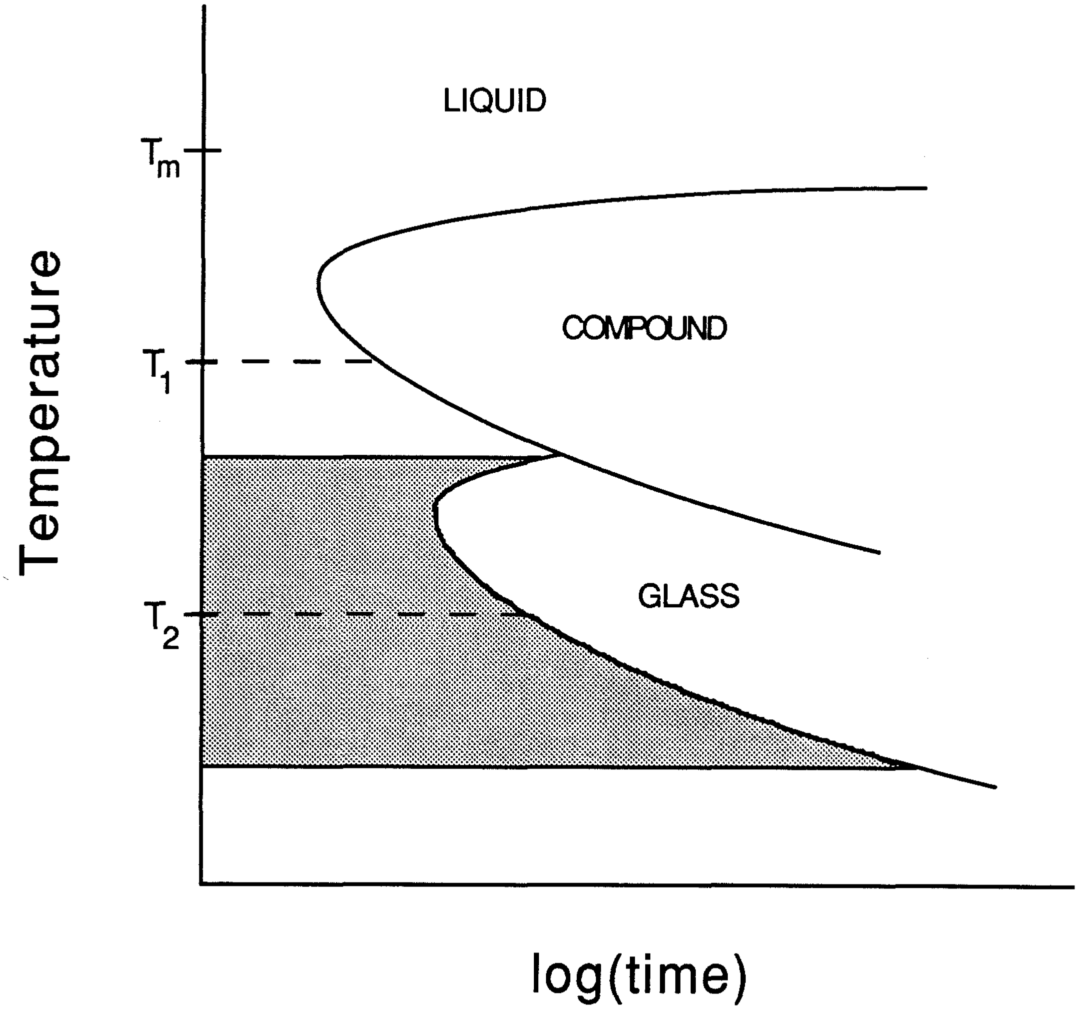

Figure 1.4. TTT diagram representing chemically driven amorphization. The horizontal dashed lines represent isothermal reactions. At T_1 the temperature is high enough to nucleate the equilibrium crystal. At T_2 this nucleation is suppressed, leading to glass formation. The shaded area represents the temperature window for amorphization (see text).

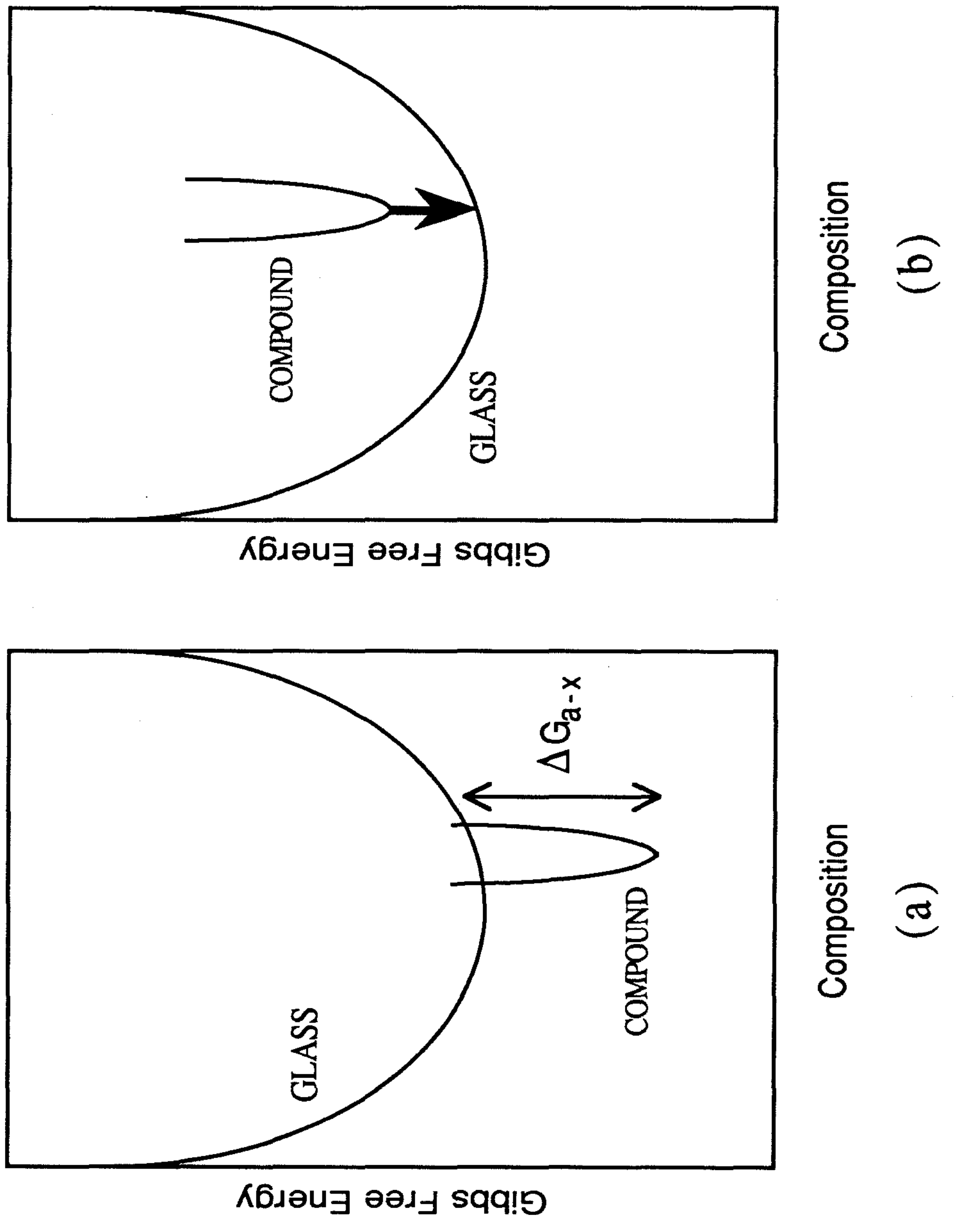

(b)

(a)

Figure 1.5. Schematic free energy diagrams depicting amorphization of an intermetallic compound. (a) Initial configuration, and (b) after disorder raises the compound's free energy higher than that of the amorphous phase. ΔG_{a-x} is the free energy of crystallization.

1.4.1 Irradiation

The predominant method of amorphizing intermetallic compounds until quite recently has been to irradiate them with ions, high energy electrons, or fast neutrons; for an recent review, see Okamoto and Meshii.[1.17] It has been found that not all compounds form glasses upon irradiation; only those that meet certain criteria are able to undergo the transition to amorphization. Easily amorphized compounds usually have no order–disorder transition; that is, the disordering temperature lies above the melting point.[1.11] Alloys of this type are not able to accomodate chemical disorder easily, and there is no disordered phase to compete thermodynamically with the glassy phase. Also, line compounds, or those with very narrow phase field widths, are more susceptible to amorphization.[1.18] These compounds generally have high chemical ordering energies; thus for a given amount of disorder their free energy is raised to a larger degree.

These somewhat general criteria point to the creation of chemical disorder as the driving force for amorphization. The reduction of chemical order with increasing electron irradiation was directly observed by Luzzi et al. in Cu_4Ti_3.[1.19] Additional support for this comes from Okamoto and Meshii who postulate that compounds whose Debye temperature is strongly dependent on the degree of chemical disorder are those most likely to undergo amorphization due to a shear instability.[1.17] When taking only their associated excess enthalpies into account, the vacancies and Frenkel pairs created by irradiation generally do not reach a sufficient concentration to raise the free energy of the crystal to that of the amorphous phase.[1.20] However, chemical disordering has been correlated with the atomic displacements and resultant volume strain directly produced by irradiation.[1.21] In addition, non-equilibrium concentrations of point defects often lead to formation of dislocation loops, which may encircle antiphase boundaries, increasing the stored enthalpy due to chemical disorder.[1.22] Finally, vacancies may recombine with an interstitial atom of the wrong species and thus create highly local chemical disorder.[1.23] However, care must be taken to irradiate the sample at a low enough ambient temperature, which effectively includes the phenomena of "beam heating" and radiation enhanced diffusion, to avoid defect recombination and subsequent reduction in atomic disorder.

1.4.2 Ball Milling

Recently, some powders of intermetallic compounds have been amorphized by high energy ball milling.[1.24] This process involves placing powders and hardened steel balls together into a sealed steel vial which is then vigorously shaken. The collisions of the balls trap powder particles, which are severely deformed, fractured, and cold welded in the process. Mixtures of elemental powders can also be used, with the objective of inducing a diffusion-driven solid state reaction (see Section 1.3). An illustration of this type of milling, also known as mechanical alloying, is shown in Figure 1.6. Mechanical alloying produces sizeable quantities of amorphous powders; research on methods of consolidating them into bulk glasses is currently in progress.

As with irradiation, not all compounds amorphize during ball milling.

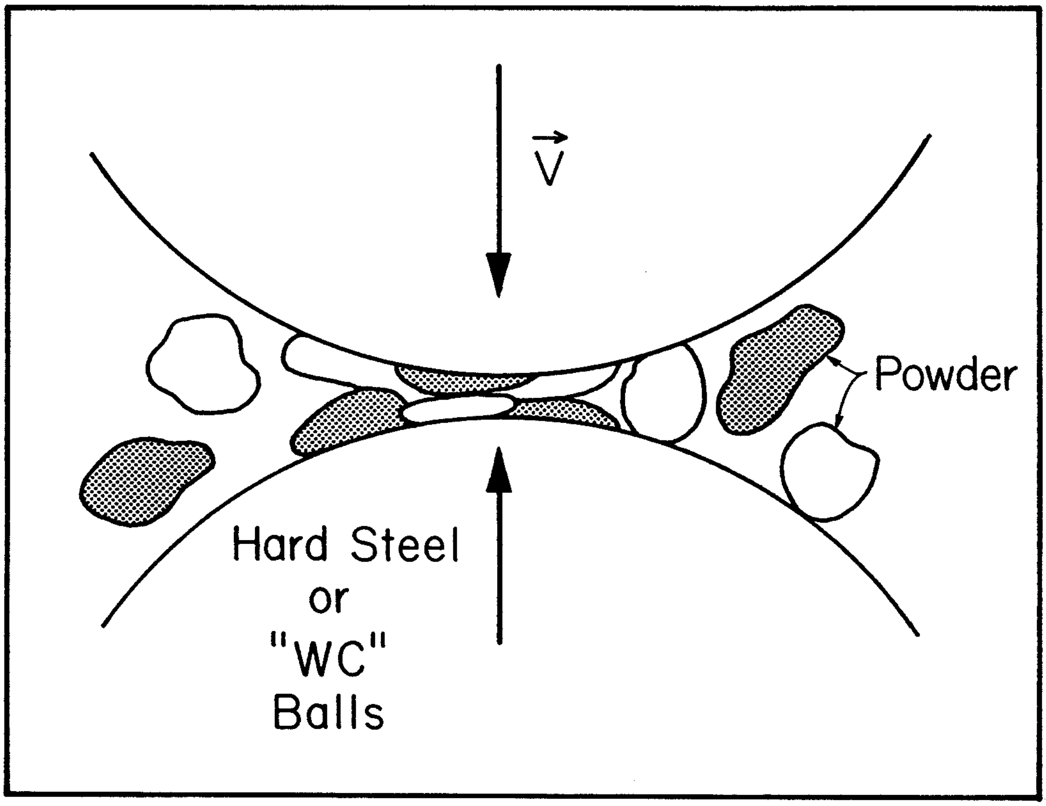

Figure 1.6. Mechanical alloying of two elemental powders produces both deformation and consolidation (taken from Ref. 1.11).

Seki and Johnson found that the line compound $CuTi_2$ amorphizes after ten hours, but CuTi does not.[1.25] In fact it remains crystalline even after fifty hours of milling.[1.26] Below 500° C the latter compound has a phase field width of over 2 atomic percent (at.%). This result might be expected after studying irradiation behavior, as discussed in Section 1.4.1. However, CuTi has successfully been amorphized by electron irradiation.[1.27] Interestingly, T_c^{rad} for CuTi is about 100° K lower than that for $CuTi_2$.[1.28] T_c^{rad} is defined as the temperature of the sample during irradiation at which ordering due to radiation enhanced migration of point defects overtakes chemical disordering, thus preventing amorphization from occurring no matter how high the irradiation dose. This effectively means that $CuTi_2$ can store more excess enthalpy due to chemical disorder than CuTi can at a given temperature (assuming that defect recombination rates are comparable in both alloys).

Seki and Johnson confirm this, measuring both the long–range order parameter S (using x–ray diffraction) and the stored enthalpy of both compounds. The former decreases from $S=1$ to about $S=0.5$ rapidly with milling in $CuTi_2$ but stays relatively constant in CuTi. The stored enthalpy in $CuTi_2$ increases to a value of almost 11 kJ/mole, but in CuTi saturates below 6 kJ/mole.[1.25] It is thus plausible that chemical disordering is responsible for amorphization during ball milling as well as irradiation. However, the behavior of CuTi demonstrates that it is more difficult to increase such disorder by mechanical deformation than by irradiation, perhaps because dislocations may form stable cellular substructures which resist further deformation, or because movement of superlattice dislocations will eventually sweep away antiphase boundaries that had been formed.[1.29,1.30]

This may be why S for $CuTi_2$ never dropped below 0.5, even for increased milling times. In other words, deformation–induced defects not only cause disorder but also may be partially responsible for reordering as well. They may thus be self–limiting with respect to enthalpy storage. (In addition, the actual defect production mechanisms activated by deformation may differ in both compounds). In contrast, the process of point defect creation during irradiation serves only to increase disorder. A different process, defect recombination (which is influenced most strongly by ambient temperature) is responsible for reducing the disorder. Of interest also is a molecular dynamics simulation that showed CuTi does not amorphize from an increase in chemical disorder alone, even when $S=0$; Frenkel pair production is required as well.[1.31] Since deformation does not produce very many Frenkel pairs, this result seems to be in agreement with experiment.

Research activity in ball milling has expanded widely in recent years; however, it does have certain disadvantages. The balls and vial chip and wear, contaminating the final powder product. In an attempt to solve this, tungsten carbide (WC) balls have been used; these, however, eventually fracture as well. Abe has used a titanium vial and balls on pure titanium powder; the powder cold welded to the balls, effectively stopping the experiment.[1.26] Similar experiments with Ti–Cu alloys are ongoing; it is expected that the composition of the alloy will change with increasing milling time. It is also common for the vial to be contaminated with oxygen or nitrogen, resulting in the formation of undesirable phases.

In addition, the process of ball milling involves highly localized depositions of energy at the collision sites. This has been hard to characterize because it is not known how much material is actually being impacted, how many collisions per unit time a given particle undergoes, and because there are three concurrent processes occurring: deformation, fracture, and cold welding. The collisions result in a sharp rise in the local temperature, the magnitude of which is strongly dependent on the type of mill and the speed setting used, as well as the powder being processed. Two typical estimates for the effective temperature of the powders between the the colliding balls are approximately 280° C [1.32] and 407° C.[1.33] However, Lee et al. found that raising the *ambient* temperature to 200° C did not induce any drastic changes in the milling behavior of their samples. Thus it is unlikely that transient temperatures exceeded the crystallization temperature of the glasses. It is clear, however, that whatever the actual temperature rise produced, ball milling, like irradiation, is not an isothermal method of amorphization.

1.4.3 Compound Selection for Deformation

Mechanical deformation has been shown to be an excellent method for studying glass formation in bulk samples. It was the purpose of the present work to be the first to attempt to amorphize an intermetallic compound by rolling and by wear. Cold–rolling is a nearly isothermal process,[1.13] unlike ball milling, and the overall deformation process is more easily characterized. However, in ball milling fracture of the particles is permitted, perhaps even desirable. In rolling, the sample must remain in one piece for as long as possible. Thus ductility and fracture toughness are important to the selection of a candidate compound. In a wear experiment this criteria need not be as rigorously applied (see Chapter 3).

In general, dislocation densities have never been observed high enough for the free energy of the sample to exceed that of the amorphous phase, when solely taking into account accumulated dislocation strain energy. Only rarely does the stored energy due to deformation of a metal reach 1.5–2.0 kJ/mole.[1.35,1.36] However, when the sample is an initially ordered intermetallic (for example Cu_3Au) this value can rise as high as 4 kJ/mole.[1.37] This result unequivocally shows that for deformation experiments, increasing chemical disorder is the most likely way to raise the free energy of an intermetallic by an amount comparable to ΔG_{a-x}.

Cu–Ti was an excellent choice for a system; Figure 1.7 presents the phase diagram. It has been well studied, and it has a large negative heat of mixing, which makes it suitable for amorphization.[1.12] The glass has been melt spun successfully over the wide composition range of 30–75 at.% Cu,[1.39] so it is known as a good glass former. This makes sample preparation by rapid quenching easier and more controllable. It is ductile in both the glassy and crystalline phases, allowing it to be rolled to a relatively large extent. As required, there are many ordered compounds present in this system. From the above discussions, a line compound with no observed order–disorder transition was preferable to study. This left the choice of $CuTi_2$, Cu_3Ti_4, or Cu_2Ti_3. All of these phases have similar structures: body–centered tetragonal lattices consisting of varying numbers of distorted bcc subcells stacked along the c–axis.[1.39] The simplest of these is $CuTi_2$, which has three subcells (see Figure 1.8). This was the compound selected.

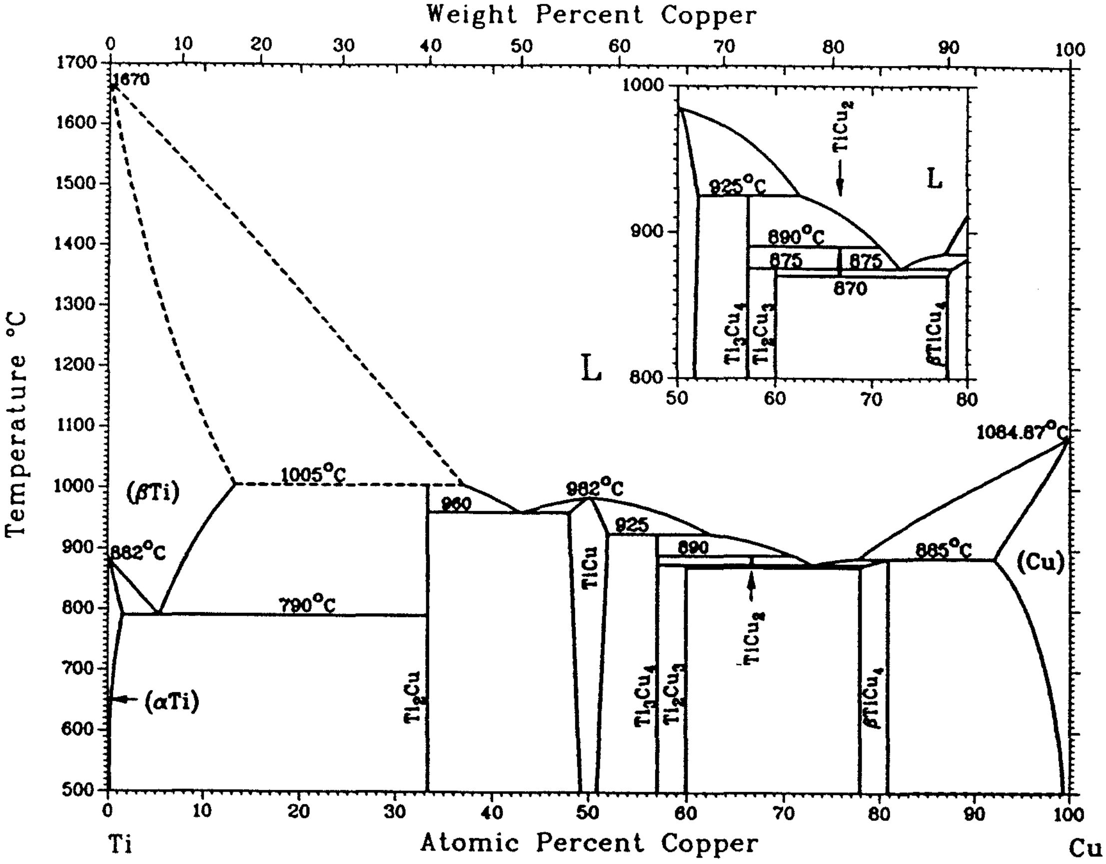

Figure 1.7. Phase diagram for the Cu–Ti system (taken from Ref. 1.38).

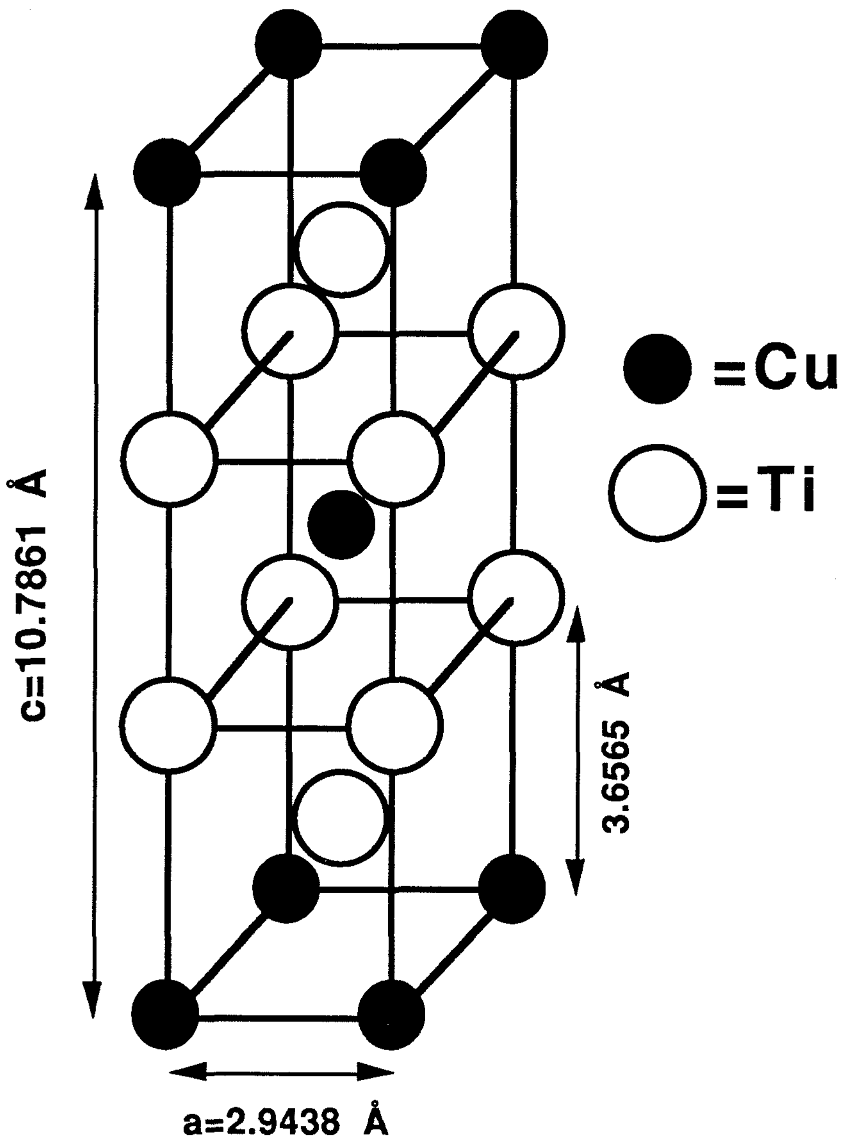

Figure 1.8. The crystal structure of $CuTi_2$ (body–centered tetragonal, $MoSi_2$ prototype; Pearson symbol *tI*6, space group *I*4/*mmm*, Strukturbericht designation $C11_b$).[1.39]

CHAPTER TWO: Deformation of Ribbons

2.1 Sample Preparation

Pieces of copper rod (99.999% pure) and titanium ingot (99.93% pure) were levitation melted on a silver boat in an argon atmosphere. The titanium was premelted to reduce surface impurities. The geometry of the silver boat allows the metals to levitate while alloying (Figure 2.1). The sample was turned over and melted two additional times after alloying to insure homogeneity. The resulting ingot of composition $Cu_{35}Ti_{65}$ was then rapidly quenched by melt–spinning in a helium atmosphere, forming ribbons approximately 40 μm thick and 3 mm wide.

A melt–spinner (Figure 2.2) consists of a vertical RF coil located over a copper wheel. Small pieces of ingot are placed in a quartz tube fabricated with a 3 mm wide slot in the bottom. This is then placed within the coil so that the slot is lined up perpendicular to the direction of travel of the wheel. The open top of the tube is connected via a valve to a pressurized He gas supply. The sample is melted by induction heating and the valve is opened, forcing the liquid onto the rapidly spinning copper wheel. (The surface of the wheel moves at about 30 m/sec.) The large thermal mass of the wheel permits rapid solidification of the melt, at rates of about 10^6 °K/sec.[2.1] The rotation of the wheel causes the melt to form a ribbon. Melt–spinning is something of an art; among the parameters that need to be balanced are wheel speed, heating rate, relative gas pressure, size and shape of the slot, and distance of the slot from the wheel. When working with an unfamiliar alloy, dozens of attempts may be

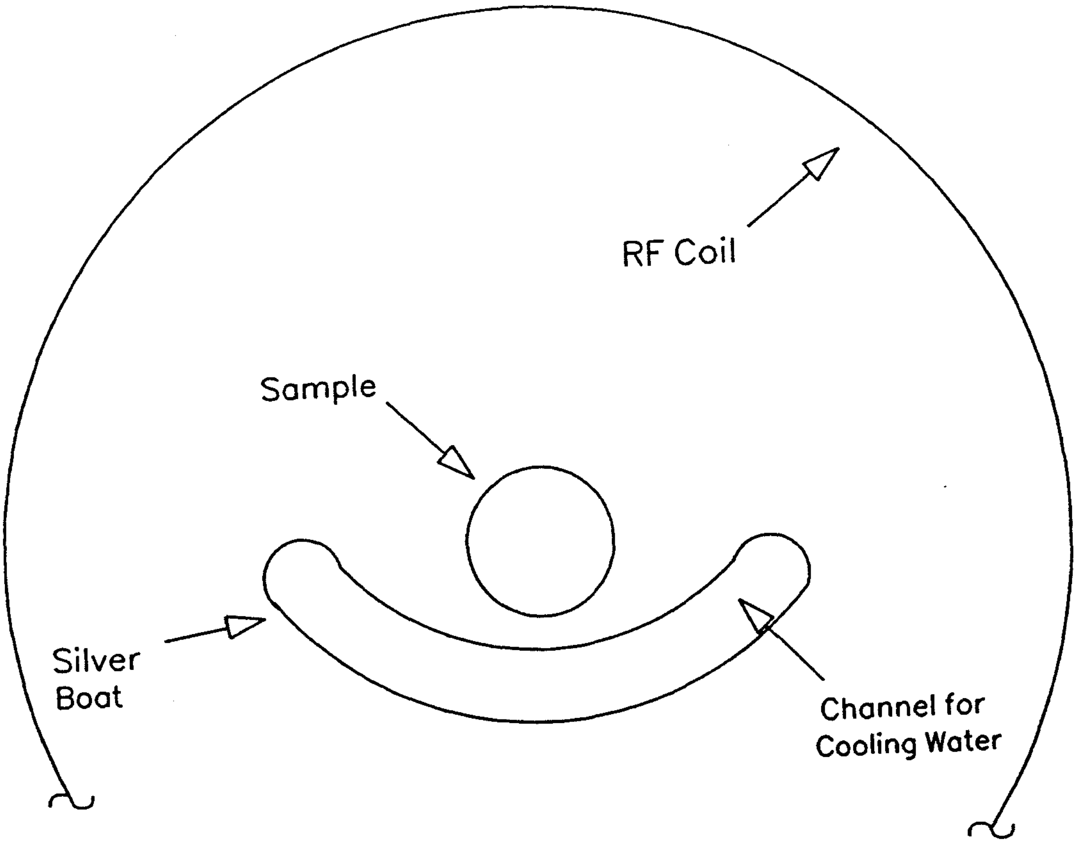

Figure 2.1. Cross section of a silver boat melting apparatus.

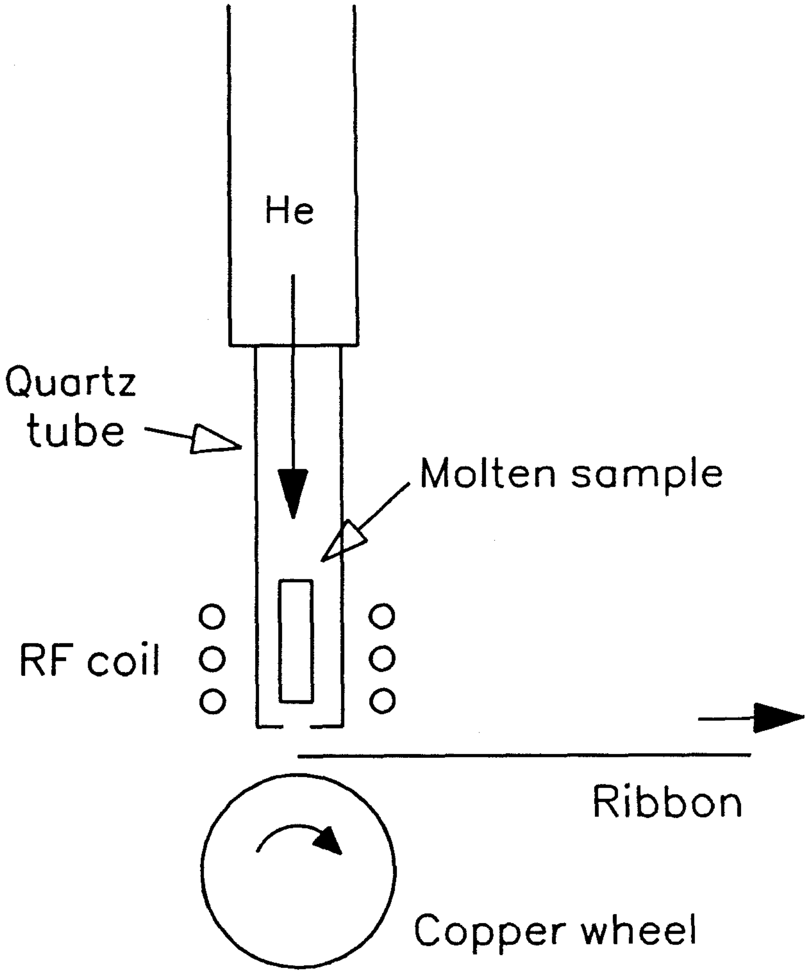

Figure 2.2. Schematic illustration of a melt–spinning apparatus.

required to obtain well–formed ribbons.

Pieces of ribbon were stacked between two plates of 24 guage stainless steel (i.e., a sheath) and rolled. The rolling mill used (Figure 2.3) consists of two parallel steel rollers that rotate in opposite directions. The sample is placed next to the rollers, which employ friction to pull it between and through them. Plastic deformation occurs due to the compression of the rollers, which reduces the thickness of the sample. The distance between the rollers is adjustable and is decremented in increasingly smaller steps as a sample is thinned. This is necessary both to suppress crack formation in the ribbons as well as to avoid excess heating. It has been found that when this procedure is employed the temperature rise is less than 25° C and lasts for only a fraction of a second.[2.2] Also, a constant rolling direction in the ribbons was maintained to minimize both formation of dislocation tangles caused by changing the slip direction as well as lateral spreading of the sample due to inhomogeneous lateral frictional forces.[2.3] Both of these make the sample crack and shatter relatively early in the deformation process, ending the experiment prematurely.

The final pass through the mill is made when the rollers are actually touching (they are spring loaded to permit the sample to pass through). At this point the sample is too thin to be deformed and is removed from the old sheath, folded in half to increase its thickness, and inserted into a new sheath. The halves of the sample cold weld together as rolling proceeds, effectively forming one layer. Eventually the sample cracks enough to make further rolling impossible, and often simply disintegrates. During the experiment, the average relative degree of deformation experienced by the sample is given by

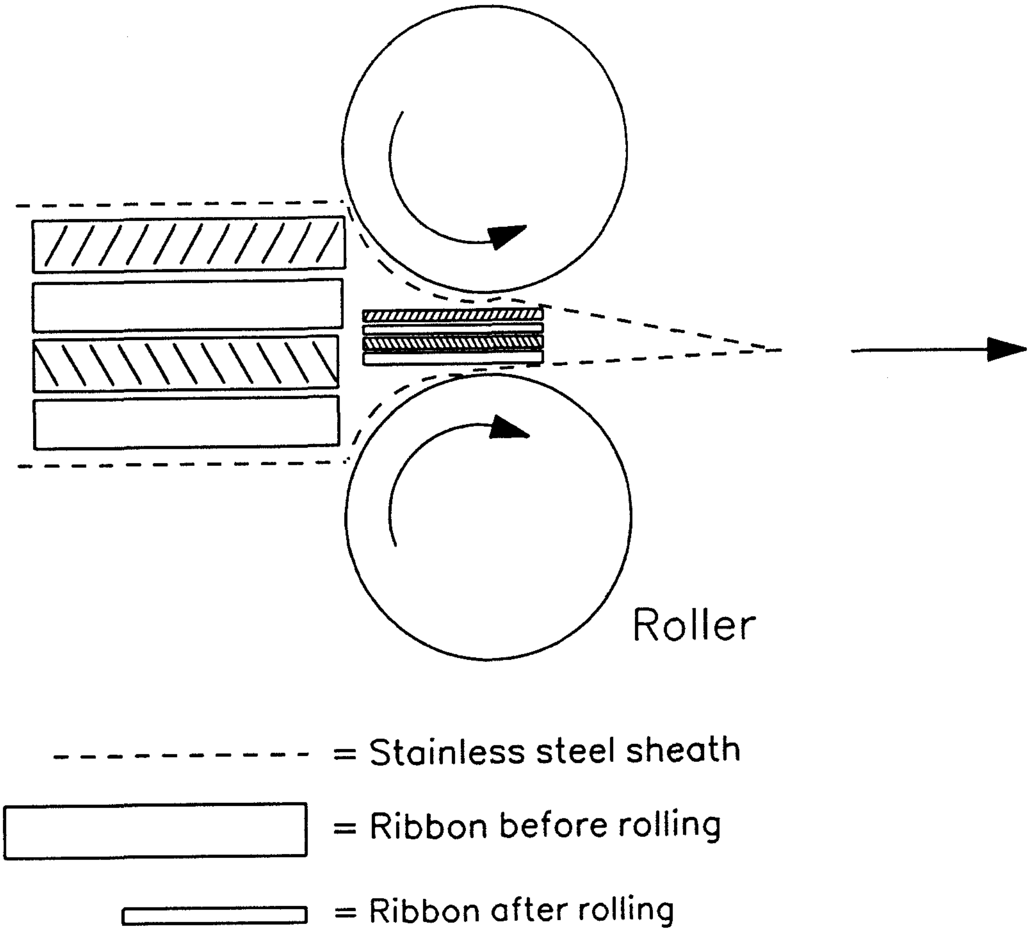

Figure 2.3. Depiction of a rolling mill experiment. Ribbons are stacked in a stainless steel sheath and passed through the mill, reducing their thickness.

the reduction ratio RR, as follows:

$$RR = \frac{t_i}{t_f} \times 2^n ,$$

where t_i is the initial sample thickness, t_f is the final thickness, and n is the number of folds made in the sample (i.e., 2^n is eqivalent to the number of ribbon layers in the sample). Thus, RR increases as the amount of deformation increases.

2.2 X–ray Diffraction

During the rolling process the sample was monitored by x–ray diffraction (XRD) using Cu–Kα radiation. The diffractometer utilized the θ–2θ reflection geometry (Figure 2.4). Cu–Kβ radiation was eliminated by using a nickel filter. The interplanar spacing corresponding to a peak in the diffraction pattern is given by the Bragg law:

$$d = \frac{\lambda}{2\sin\theta} ,$$

where λ is the wavelength of the x–ray source and θ is the angle at which the peak occurs.

In this geometry it is important to know the penetration depth of the x–rays. The fraction of the diffracted signal coming from a depth d or less is given by:[2.4]

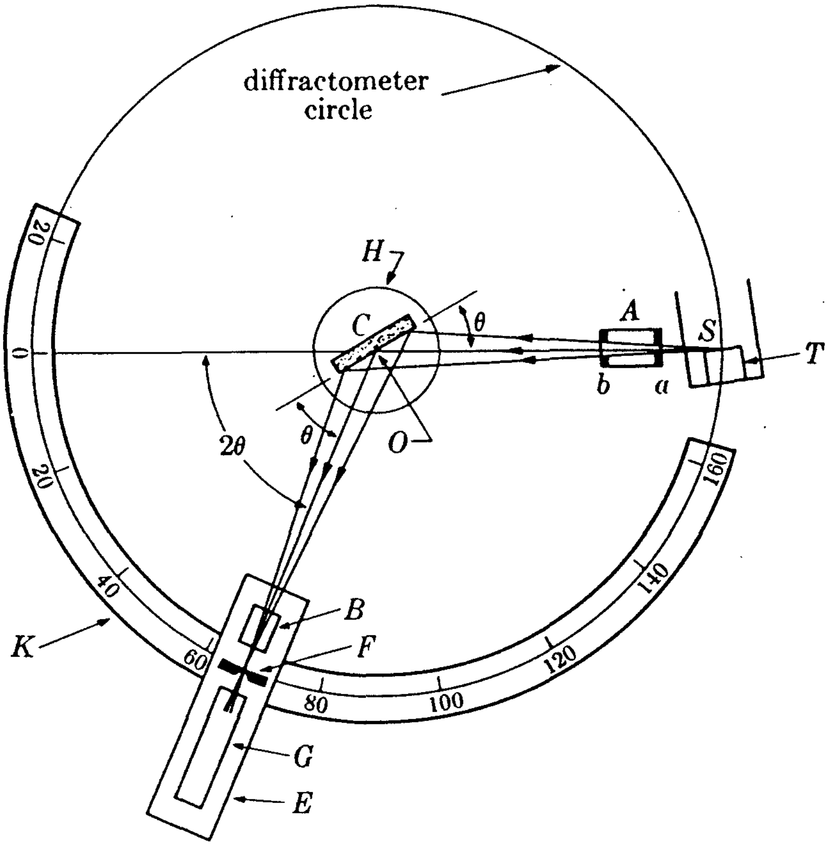

Figure 2.4. Schematic illustration of a θ–2θ x–ray diffractometer. The x–rays are produced at source S, pass through slit A, and strike the sample C. The reflected beam passes through slits B and F and are registered by the detector G. The sample is mounted on shaft H which rotates at half the angular velocity of the detector, in order to maintain the relative θ–2θ configuration depicted (taken from Ref. 2.5).

$$F_D = 1 - e^{-\frac{2\mu d}{\sin\theta}} ,$$

where θ is the diffraction angle and μ is the linear absorption coefficient. For a two–component alloy,[2.5]

$$\mu = \rho\left[w_1\left[\mu_{m_1}\right] + w_2\left[\mu_{m_2}\right]\right] ,$$

where ρ is the density of the alloy, w_i are the weight fractions of the elements, and μ_m are their mass absorption coefficients, which can usually be found tabulated in x–ray reference books. For $CuTi_2$, $\rho = 5.676\ g/cm^3$. This gives an effective penetration depth of about 2–8 μm, depending on θ.

Since the as–quenched ribbons were about 40 μm thick, both the wheel surface and the free surface of the ribbon were examined. This was necessary because the solidification of the melt depends on the distance from the wheel; the quench rate is highest where the ribbon has contacted the wheel, and lowest on the opposite, or free, surface.[2.6] Figure 2.5 shows the XRD patterns of both surfaces of the as–quenched ribbon. The free surface of the ribbon is mostly crystalline, comprised of the intermetallic phases $CuTi_2$ and Cu_3Ti_2. Although CuTi is the equilibrium phase which would be expected to appear, nucleation of Cu_3Ti_2 may have been more favorable under non–equilibrium solidification conditions. It has been observed at other compositions in this system that non–equilibrium crystal structures compete with glass formation during rapid quenching.[2.7] Indeed, the intermetallics $CuTi_2$, CuTi, Cu_4Ti_3, and Cu_3Ti_2 are all tetragonal, differing only in the stacking sequence of Cu

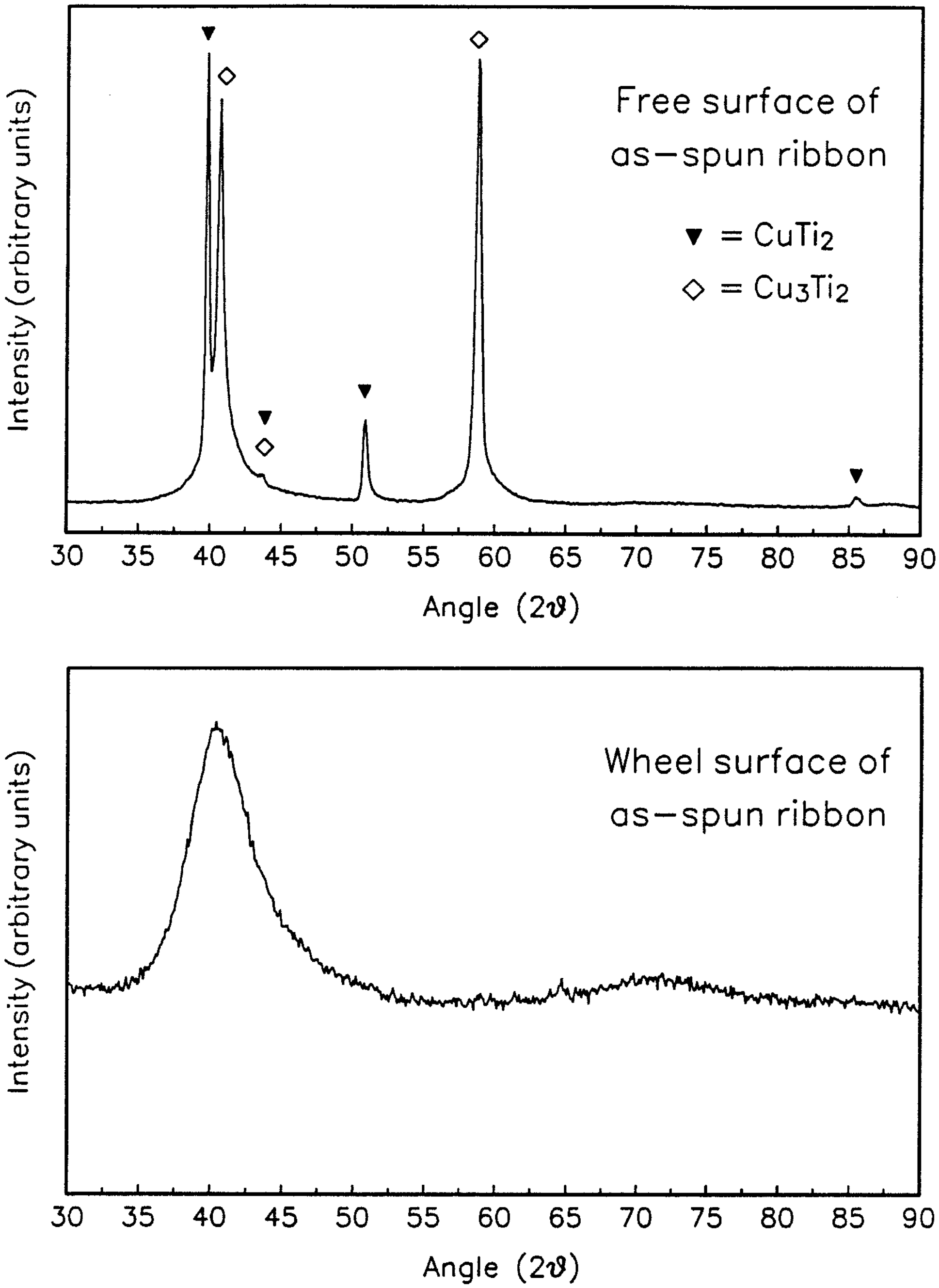

Figure 2.5. X–ray diffraction patterns of the free surface and the wheel surface of the as–quenched ribbon.

and Ti layers along the c–axis.[2.8,2.9] Thus it should be possible to nucleate a competing phase instead of the equilibrium one in the presence of high cooling rates and local compositional fluctuations. On the free surface there does appear to be some amorphous phase present as well. The wheel surface of the ribbon is completely amorphous.

The XRD patterns in Figure 2.6 monitor the progression of the ribbon as it is rolled (i.e., as RR increases). Because the ribbons fracture during the experiment, it is not always possible to determine whether the free or wheel surface, or both, are being observed. Thus the initial pattern for the as–spun sample was taken from a mixture of both the wheel and the free surfaces. As deformation increases, the crystalline peaks decrease in intensity, and the amorphous peak becomes more well defined. After about RR=2, the ribbons started to fracture. The pieces later consolidated into an amorphous foil, probably due to the exposure of new clean metallic surfaces and the transformation of the intermetallic to the more ductile amorphous phase. At RR=8.5, we see that amorphization has been completed.

2.3 Transmission Electron Microscopy

The microstructural evolution during the deformation of the ribbons was studied using transmission electron microscopy (TEM) techniques. Thin foils suitable for TEM were produced from the ribbons by cold–stage ion milling to minimize introduction of point defects and other damage. Two guns were used so that it was possible to examine the middle of the ribbon as well as either surface (which may be accomplished by using only one of the guns).

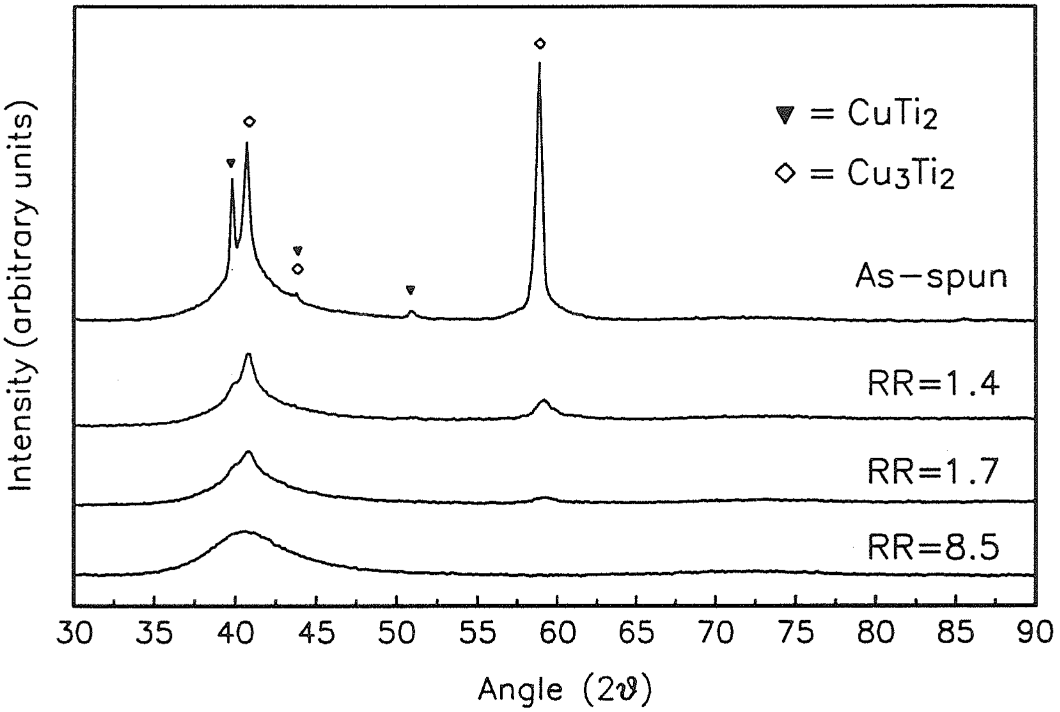

Figure 2.6. XRD patterns of the $Cu_{35}Ti_{65}$ ribbon taken as rolling progresses. RR is the reduction ratio.

The milling conditions were 5kV and an incidence angle of 14° was chosen to avoid differential thinning.

The results of TEM show that the as–spun ribbon consisted of microcrystals of $CuTi_2$ embedded in an amorphous matrix. The crystals are smaller and fewer near the wheel surface of the ribbon, where the quench rate was highest (Figure 2.7). The microcrystals in the middle of the ribbon range in size from 10 nm to 100 nm (Figure 2.8). Both the particle size and number increase until there is a microcrystalline layer at the free surface, with a grain size of .2 μm (Figure 2.9). The phase Cu_3Ti_2 was observed only here, and only in very small amounts. Its pronounced contribution to the x–ray diffraction intensity (see Figure 2.5) is probably due to a strong crystallization texture formed upon rapid solidification with a unidirectional temperature gradient.

Figure 2.10 shows a bright–field/dark–field (BF/DF) pair of micrographs of a $CuTi_2$ microcrystal at RR=1.4. An amorphous, halo–like region appears around the crystal. This new glassy phase has grown inward, proceeding from the original particle/matrix interface. There is a boundary observable between the matrix and the new glassy region, marking the outline of the original crystal. This indicates that the newly–formed amorphous phase and the glassy matrix are slightly different with respect to their structures and/or compositions. (Energy Dispersive X–ray Analysis gave similar compositions for the crystal, halo, and matrix, although the accuracy of this technique is only a few atomic percent, and the spatial resolution was hampered by the small size of the particle.) Note that a crack is visible nearby, as is a faint shear band actually passing directly through the particle. The shear band mode of deformation of the amorphous matrix clearly plays an

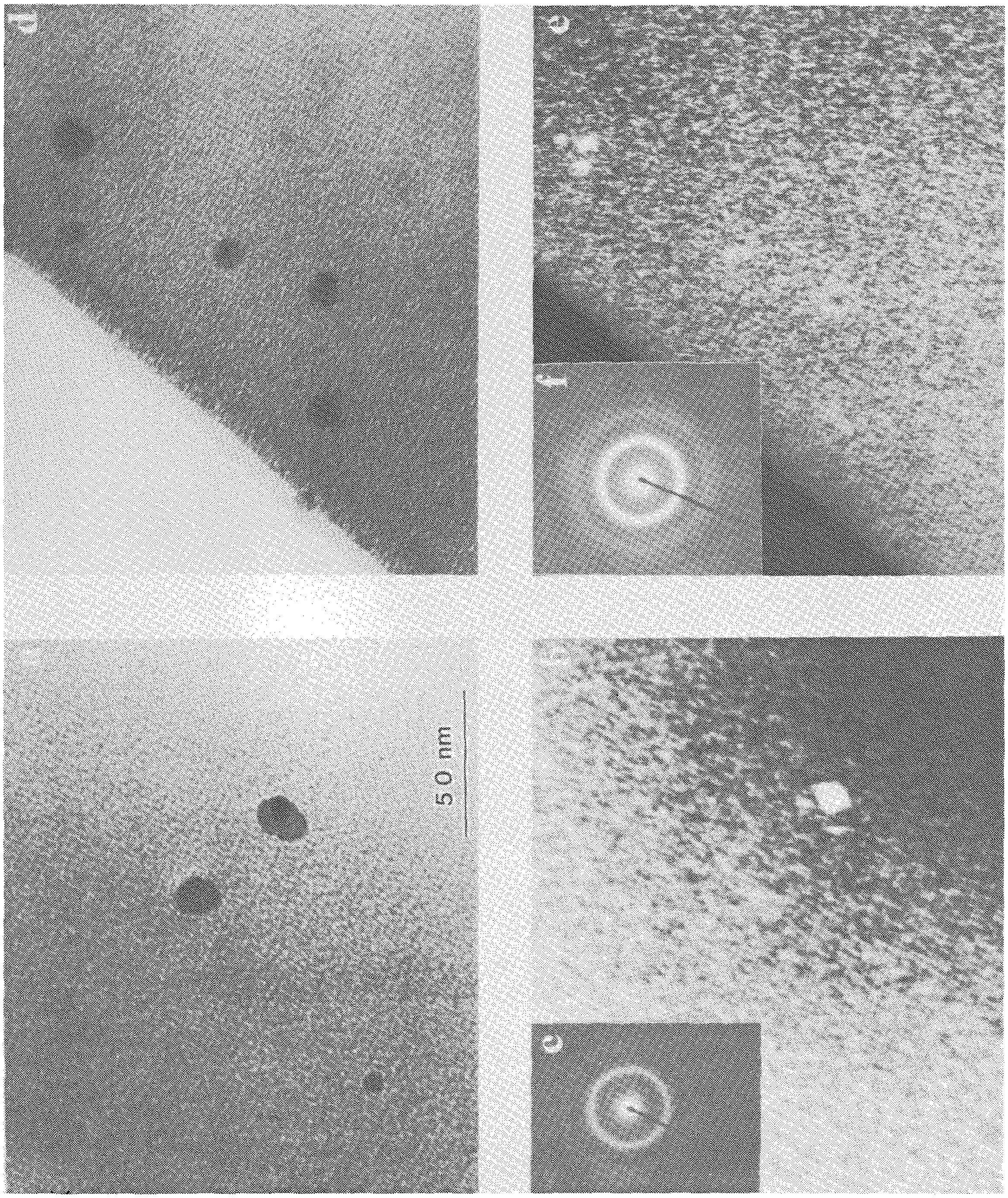

Figure 2.7. As–quenched ribbon, wheel surface. (a),(b),(c) are a bright–field (BF)/ dark–field (DF)/selected–area diffraction (SAD) trio of micrographs of an ellipsoidal 18 nm particle embedded in an amorphous matrix. (d) and (e) are a BF/DF pair of another area; (f) is an SAD of the amorphous matrix.

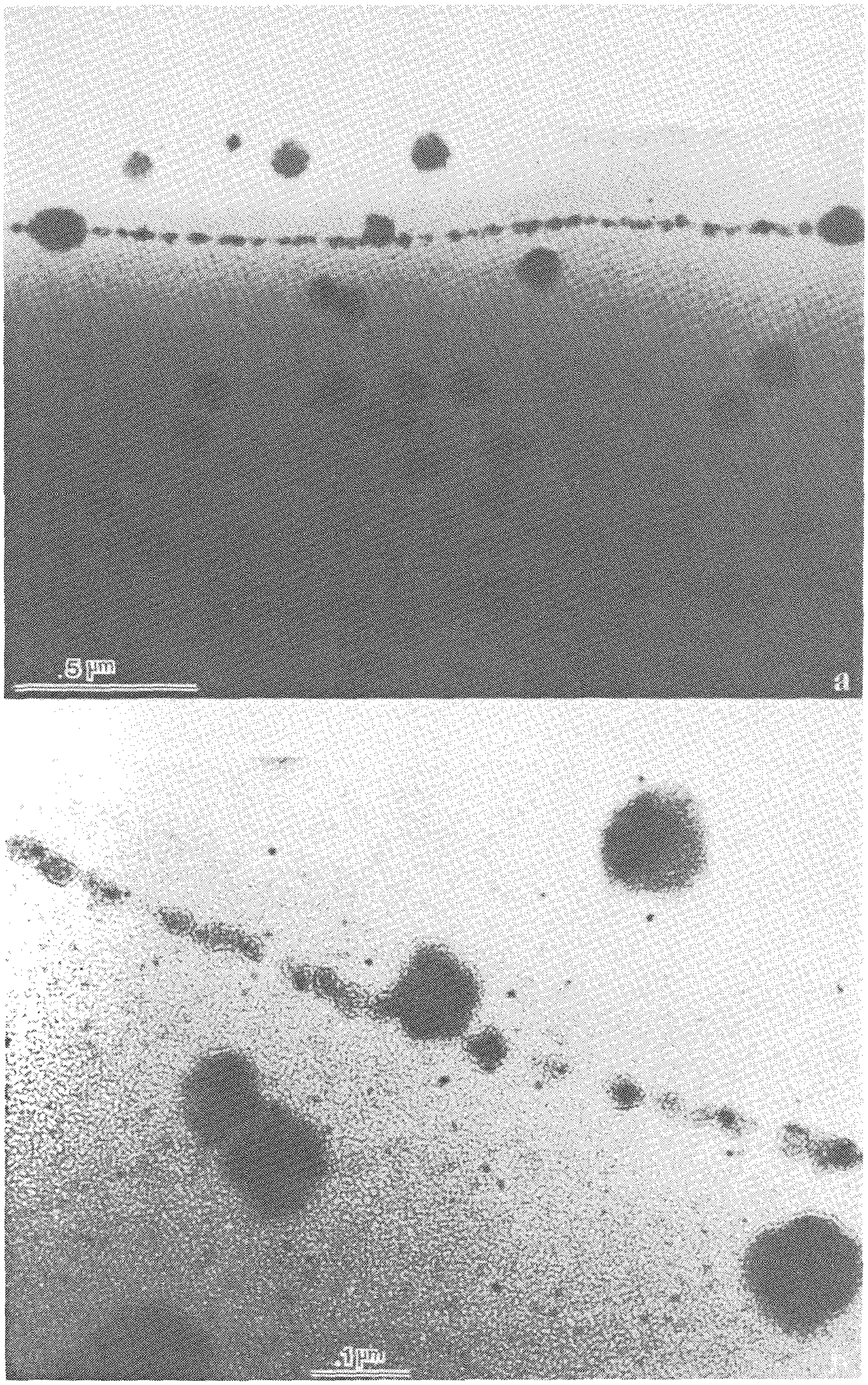

Figure 2.8. As–quenched ribbon, middle of the ribbon. Figure (b) is an enlargement of the bright–field image (a).

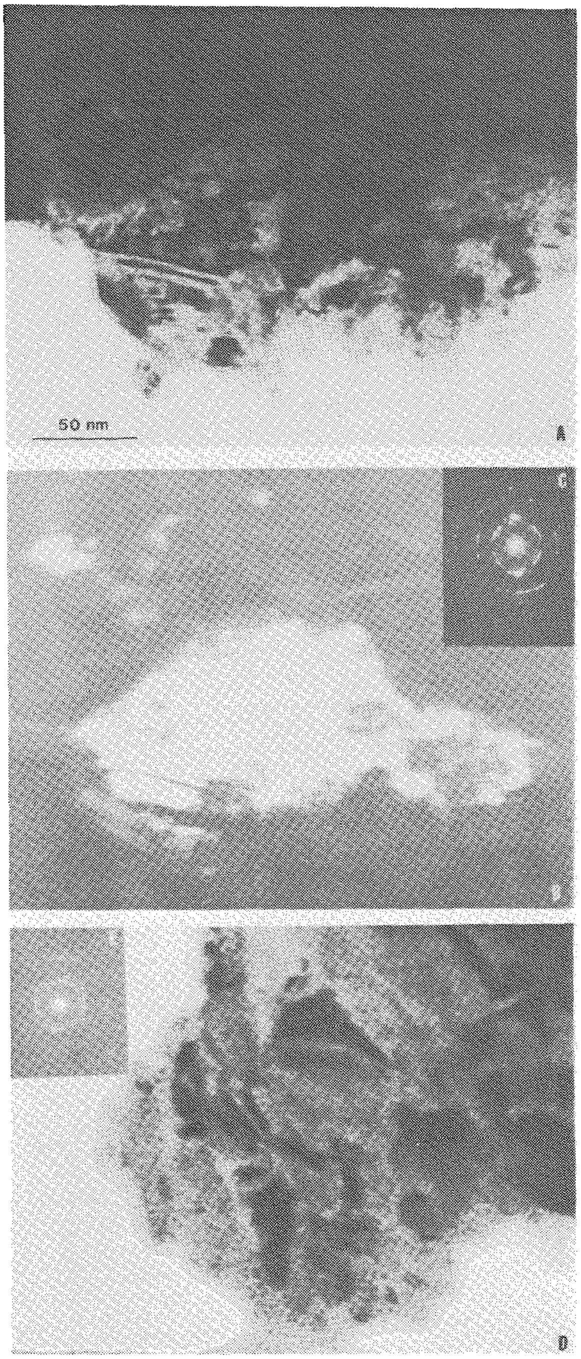

Figure 2.9. As–quenched ribbon, free surface. (A),(B),(C) are a BF/DF/SAD trio. (D) and (E) are a BF/SAD pair of another area of the surface.

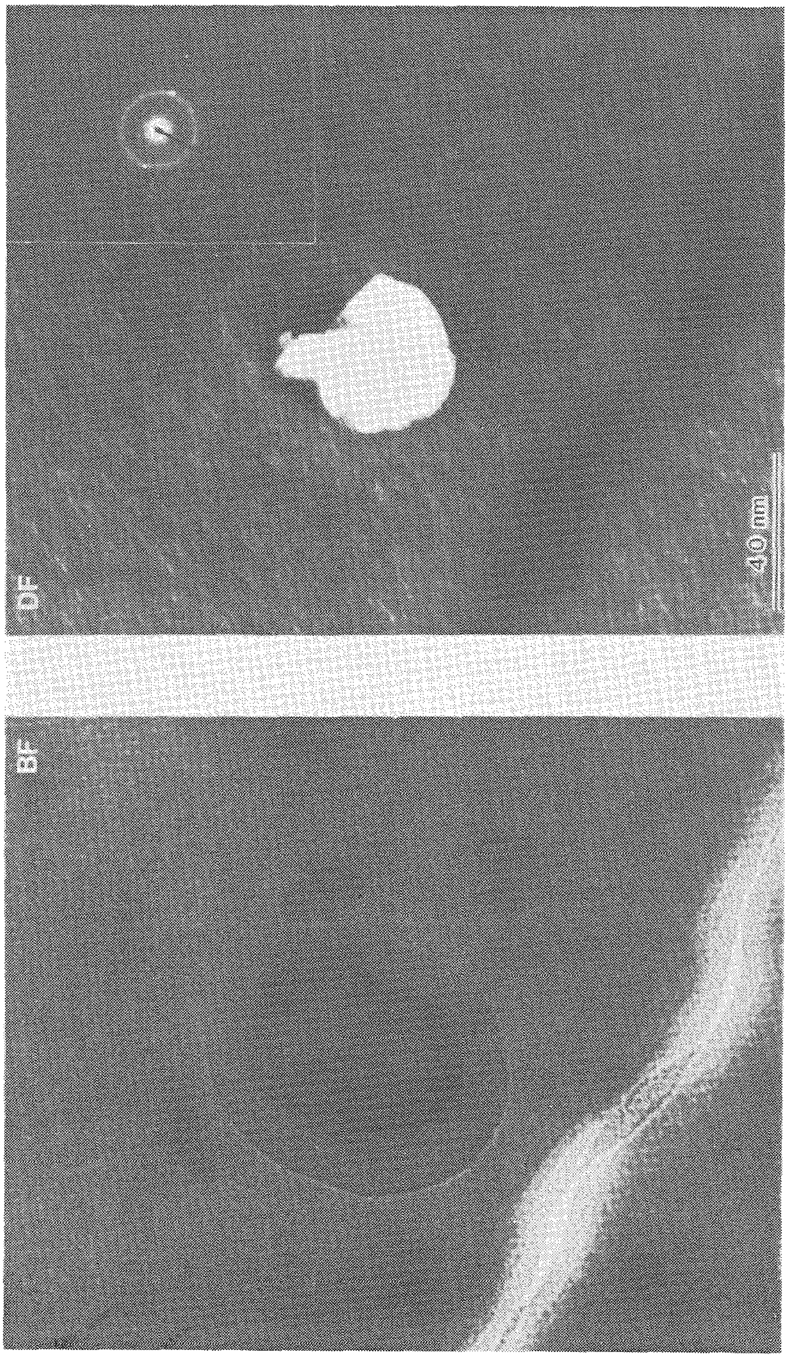

Figure 2.10. BF/DF/SAD trio of a $CuTi_2$ particle in the middle of the ribbon at RR=1.4. Note the boundary between the amorphous matrix and the newly transformed glassy phase. The remaining crystal is sharply delineated in DF; SAD implies it is a single crytal.

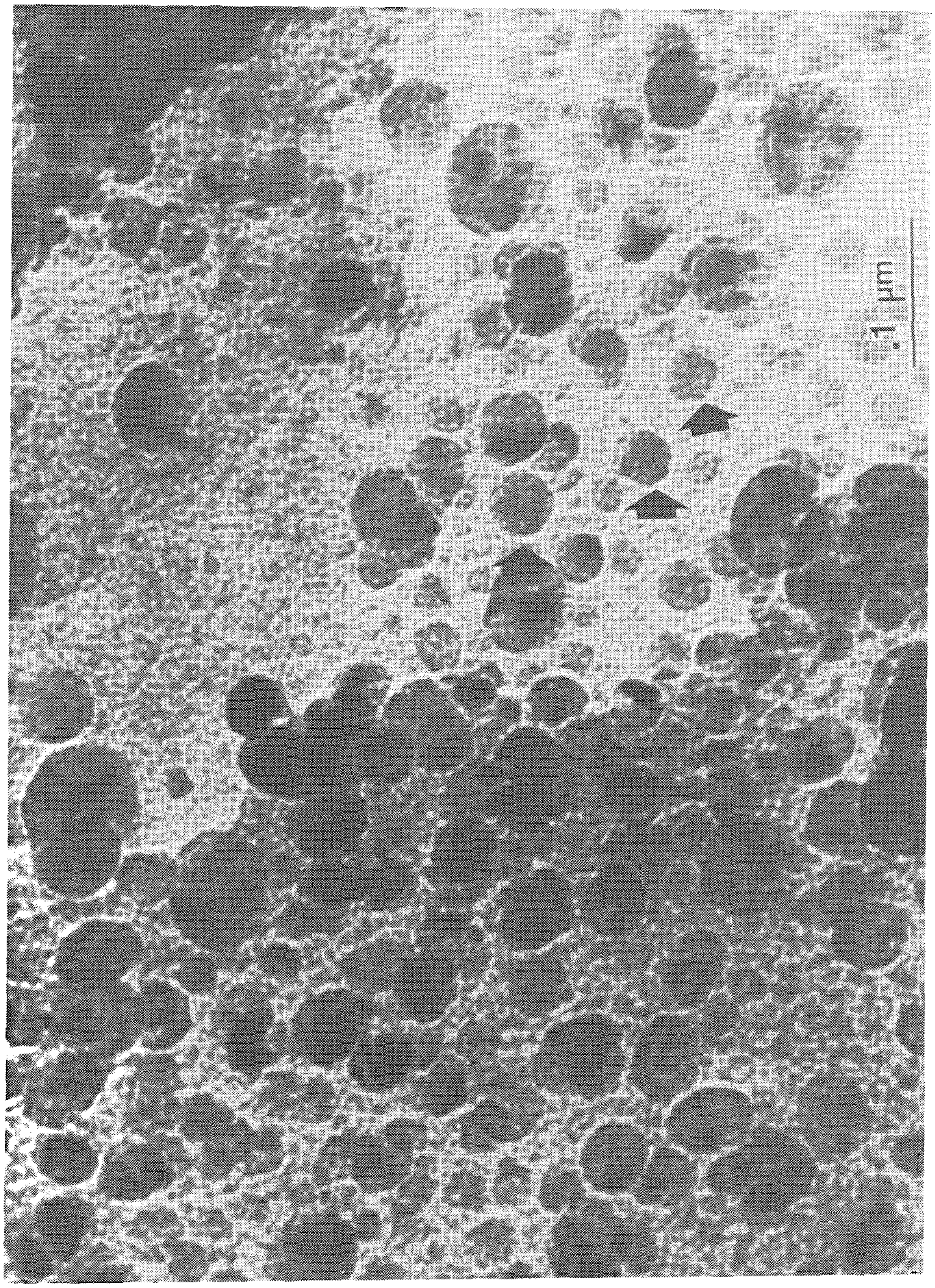

Figure 2.11. Middle of the ribbon at RR=1.4. The arrows indicate particles that seem to be completely amorphized.

important role in the amorphization process.

Figure 2.11 shows the typical microstructure of the middle of the ribbon at this deformation stage. Notice that some of the particles still contain some crystalline regions, while other halos (indicated by the arrows) seem to be completely amorphous. However, microdensitometer traces of microdiffraction pattern negatives show that nanocrystalline regions possibly exist within these halos at this reduction ratio.[2.10] It is presumed that these regions amorphize as the ribbon homogenizes after more deformation. The wheel surface of the ribbon at RR=1.4 is shown in Figure 2.12. Shear bands are visible throughout the material, which is completely amorphous.

The bright–field/dark–field pair of micrographs in Figure 2.13 depicts the middle of the ribbon at RR=1.7. There is a dispersion of microcrystals (about 10 nm in size) in an amorphous matrix, with halos only faintly present (indicated by the arrows). The free surface appears similar (Figure 2.14); the polycrystalline layer has been transformed into a layer of nanocrystals and amorphous phase. There are also some large grains remaining in the sample; one is depicted in Figure 2.14. High angle tilting in Figure 2.14d and e suggests it may be composed of more than one grain.

At the final deformation stage (RR=8.5), the ribbon is observed to be fully amorphous. A large number of parallel shear bands can be seen (Figure 2.15). Since glassy halos are not observed in the final, fully amorphous ribbon, it would seem that after extensive deformation the glass has homogenized. There are some regions containing microcrystals observed (indicated by the arrows in Figure 2.16), probably due to the inhomogeneous nature of the deformation. It is probable that these microcrystals would amorphize with

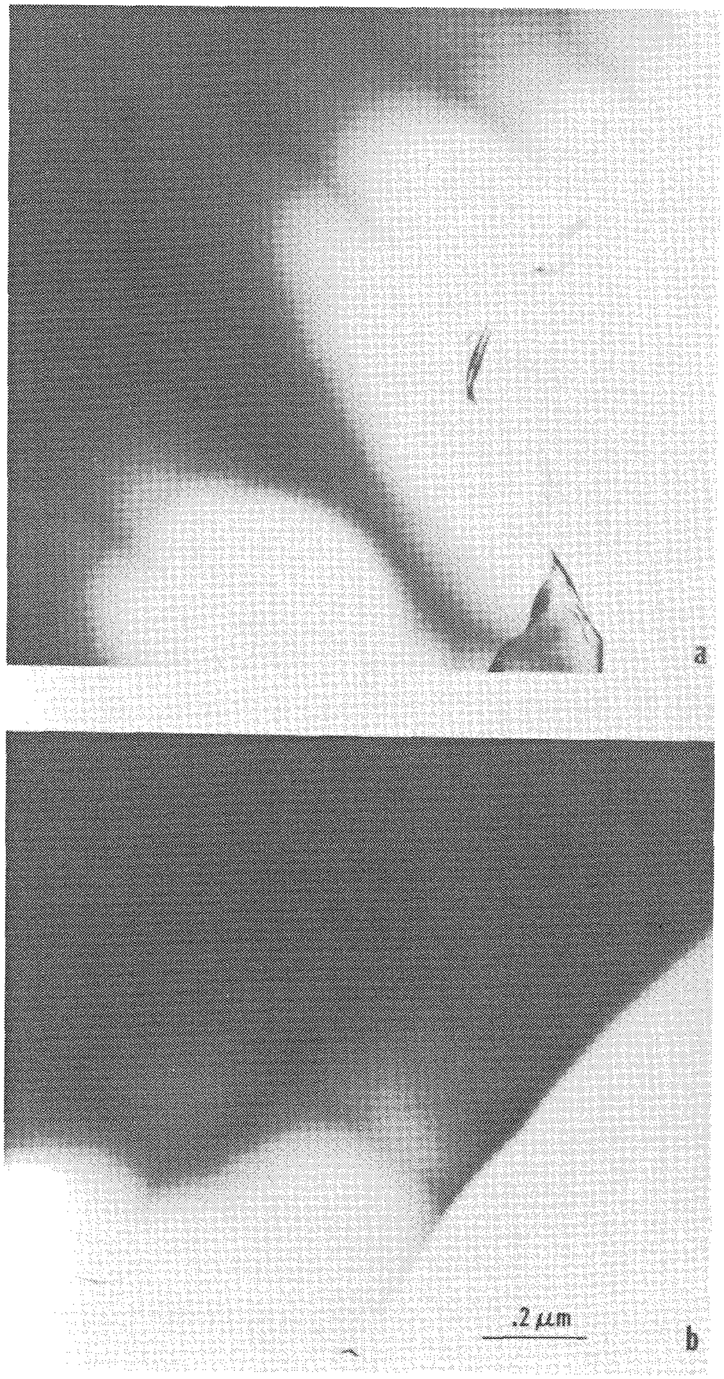

Figure 2.12. Wheel surface at RR=1.4. This surface is completely amorphous; shear bands are visible.

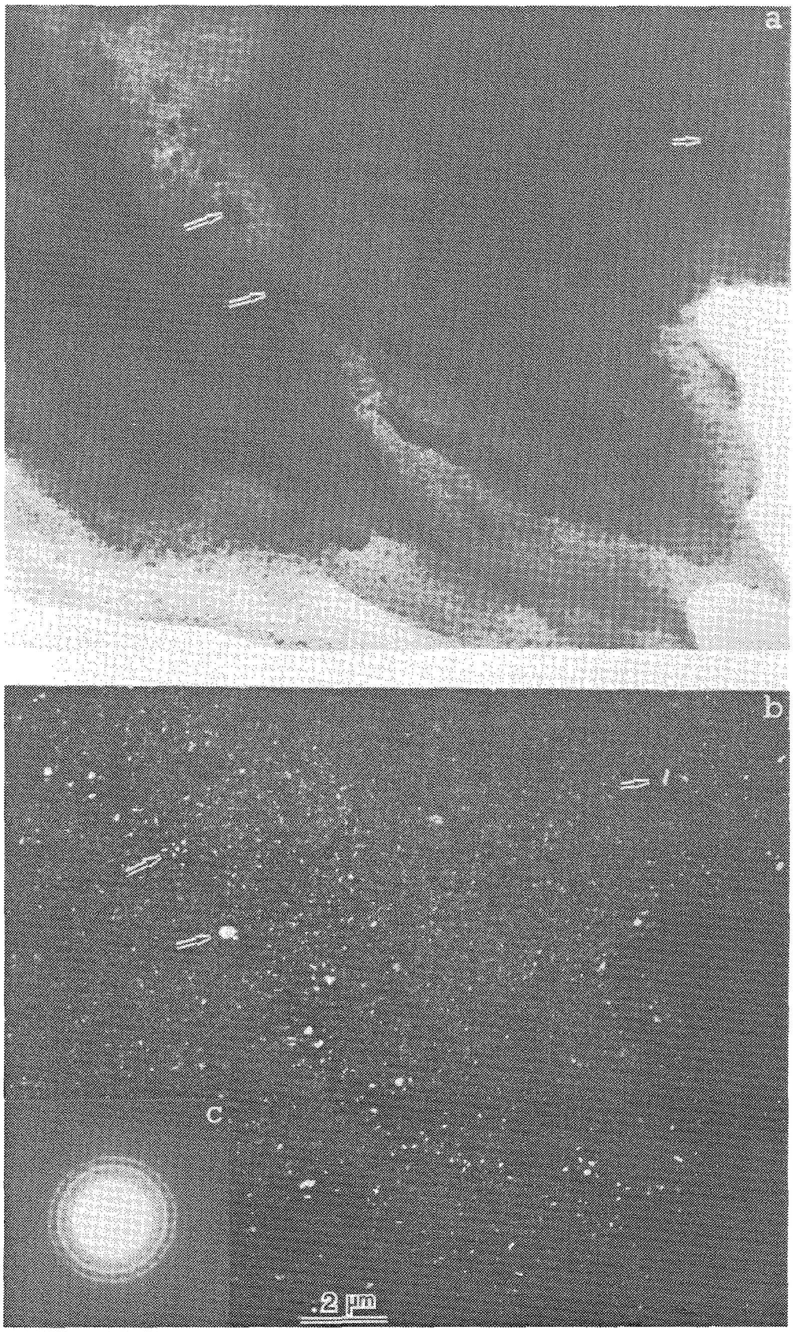

Figure 2.13. Middle of the ribbon at RR=1.7. BF/DF/SAD trio shows dispersion of microcrystals. Arrows indicate faint amorphous halos remaining.

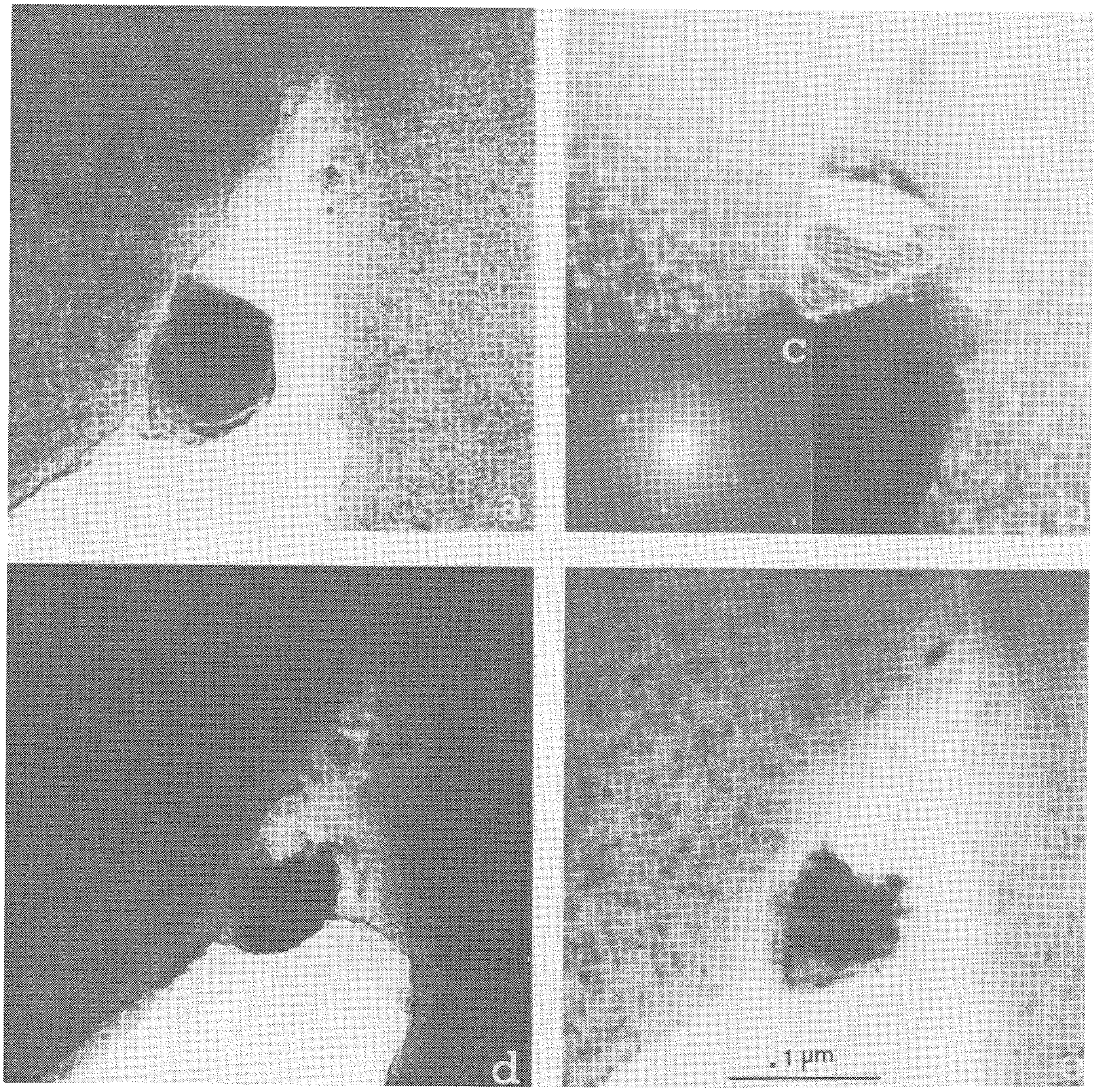

Figure 2.14. Free surface at RR=1.7. (a),(b),(c) are a BF/DF/SAD trio; (d) and (e) are bright–field images taken after large angle tilts.

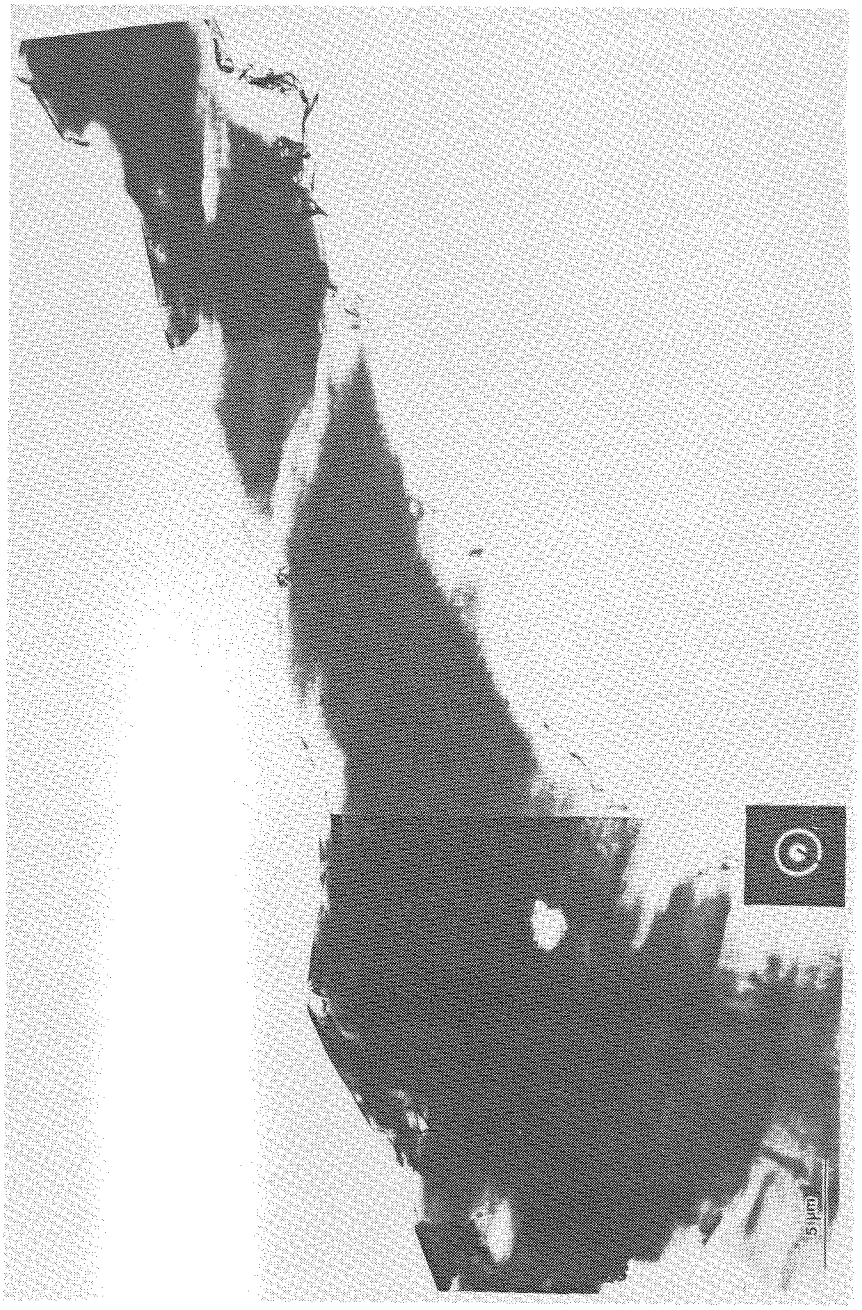

Figure 2.15. Fully amorphous ribbon at RR=8.5. Composite picture shows the large extent of parallel shear bands caused by cold rolling.

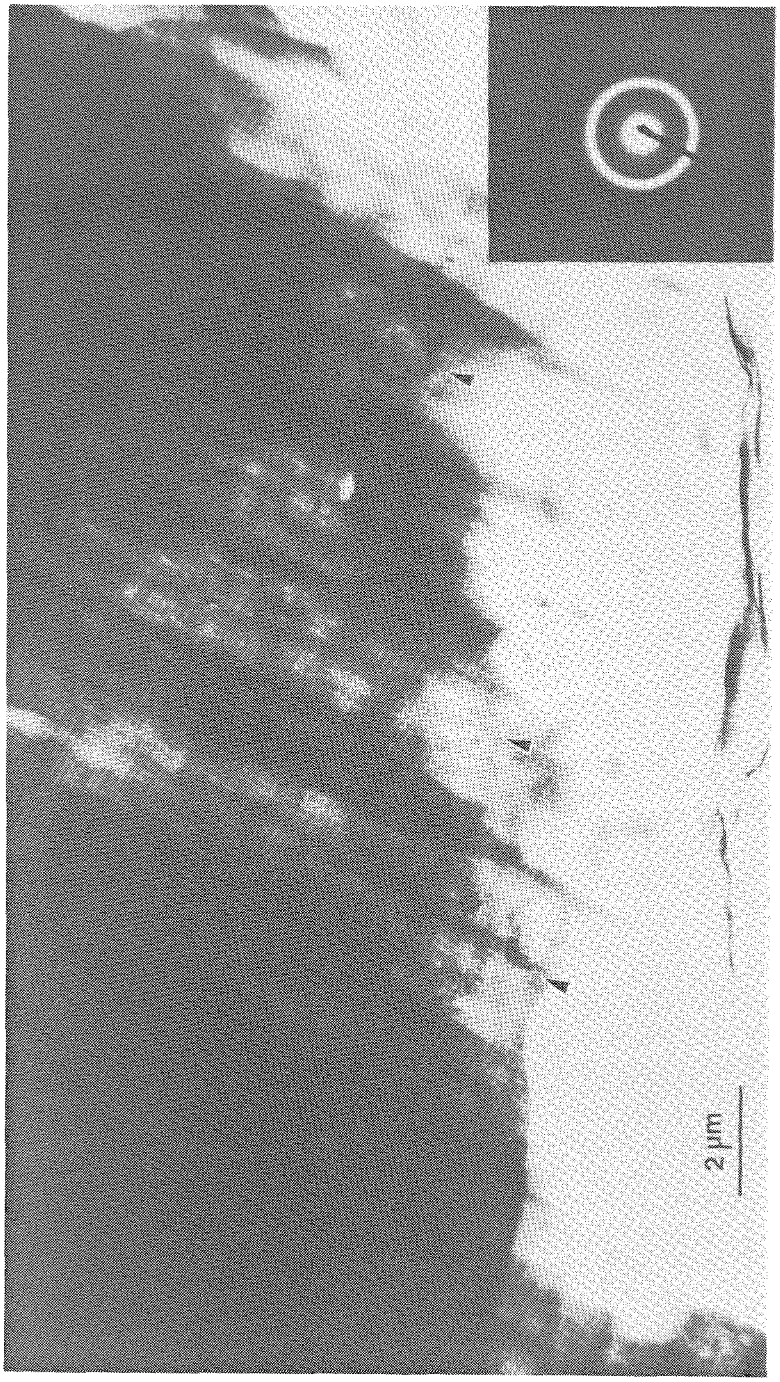

Figure 2.16. Ribbon at RR=8.5. Arrows indicate partially crystalline regions.

further rolling of the ribbon, assuming the density of shear bands increases with further deformation. Another common morphology observed is that of overlapping regions of glass (Figure 2.17). This is due to reconsolidation of the ribbon after it had fractured at earlier levels of deformation.

2.4 Further Experiments

Amorphization has been observed proceeding from the interface between the microcrystals and the glassy matrix. In order to determine whether or not this interface is necessary for amorphization to occur, a rolling experiment was performed on a melt–spun $CuTi_2$ ribbon which was annealed for 11 hours at 715°C. The progress of the sample during rolling was again monitored by XRD, as shown in Figure 2.18. The initial sample was fully crystalline, with no amorphous matrix present. The annealing treatment also should have eliminated the quenched–in defects present. The XRD patterns show no evidence of amorphization occurring while rolling progresses, even though the amount of deformation was over twice that which was needed to start to amorphize the microcrystals in the samples discussed above. Instead, a rolling texture is observed to develop, signified by the increase in the relative intensity of the (116) peak at 69.1°. The sample was rolled to RR=3.3, at which point the ribbon effectively disintegrated. Unlike the microcrystalline samples, the annealed ribbon never reconsolidated; thus, the presence of a significant quantity of the amorphous phase may be required to provide enough adhesion to allow cold welding and reconsolidation to occur.

In order to determine how important the non–equilibrium solidification

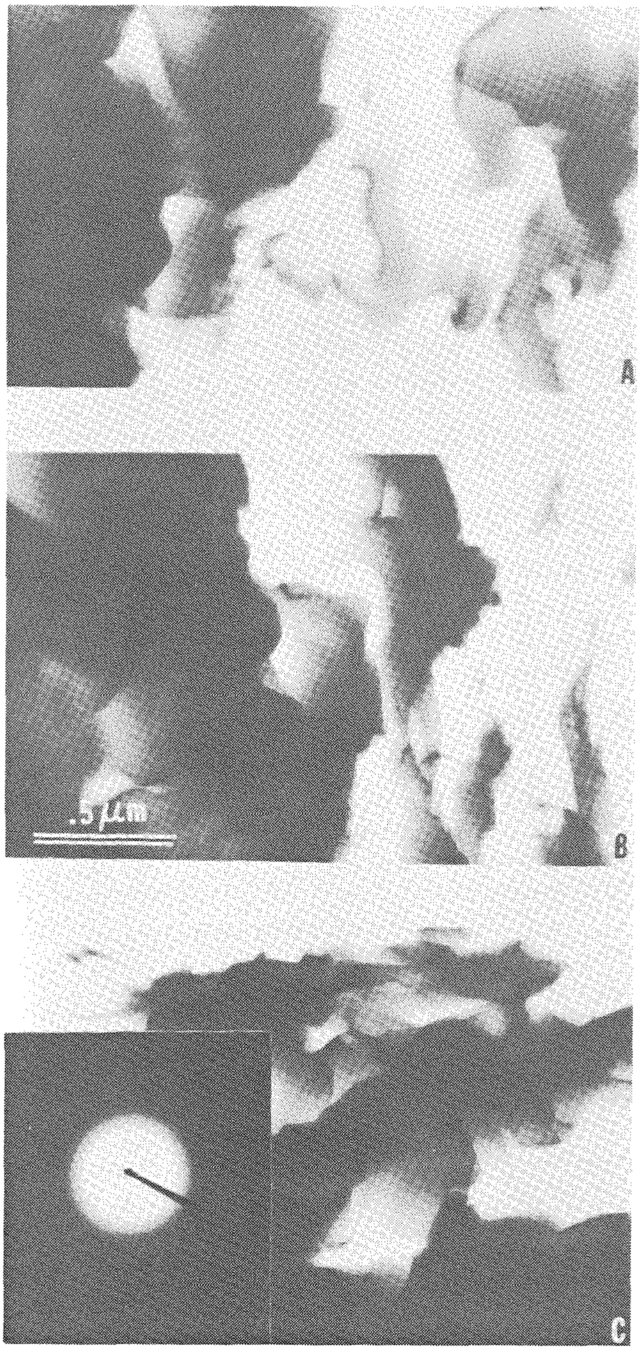

Figure 2.17. Overlapping laminations of amorphous ribbon at RR=8.5. Differences in contrast are due both to overlapping regions and to changes in specimen thickness.

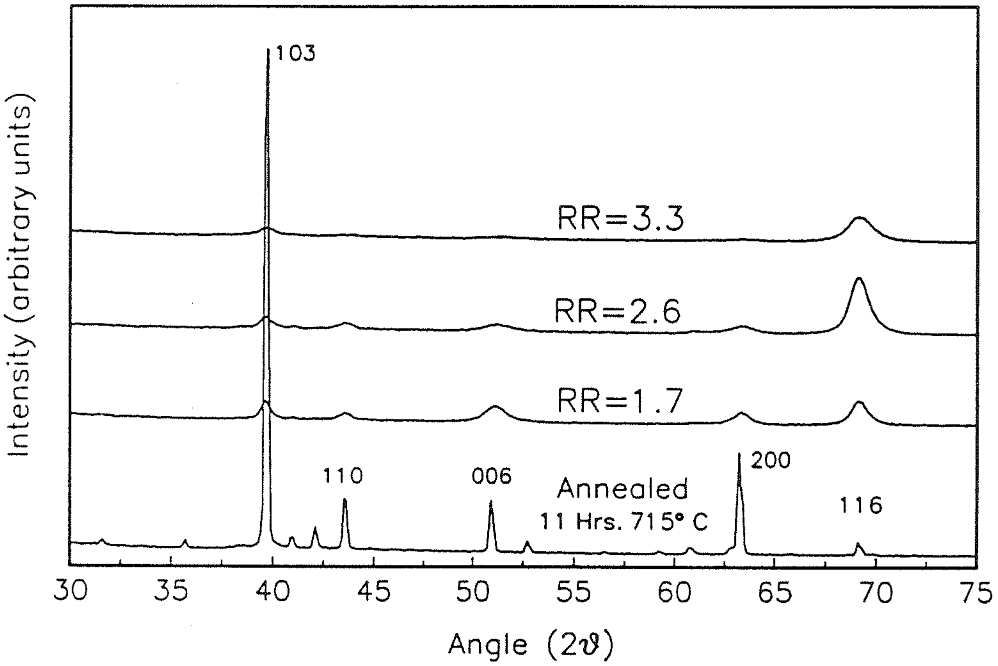

Figure 2.18. XRD patterns of a $CuTi_2$ ribbon after annealing at 715° C for 11 hours and after subsequent deformation.

of the microcrystals is to amorphization, a rolling experiment was performed on a $Cu_{35}Ti_{65}$ melt–spun ribbon that was initially completely amorphous. It was then annealed at 228°C for 3 hours in order to nucleate and grow equilibrium microcrystals while still retaining the amorphous matrix. The XRD patterns of the experiment are displayed in Figure 2.19. The INEL diffractometer used for this experiment utilizes CoKα radiation and a position-sensitive detector. As rolling progresses, the crystalline peaks broaden and shrink until they disappear; simultaneously, a broad peak characteristic of the amorphous phase grows until it dominates the pattern at RR=7.5.

2.5 Discussion

It has been shown that deformed $CuTi_2$ will amorphize when the sample morphology consists of microcrystals in an amorphous matrix. It is postulated that defects produced by deforming the crystals raise their free energy higher than that of the amorphous phase, resulting in vitrification. Because we are deforming an ordered intermetallic compound, the most likely way to store enough energy in the lattice to destabilize the crystal is the production of antiphase domain boundaries. As discussed in Chapter One, far more energy can be stored due to the chemical disorder associated with antiphase boundaries than by other deformation–induced defects such as dislocations. Antiphase boundaries are also sites of local non–stoichiometry; a high enough density may help destabilize a line compound such as $CuTi_2$.

In order to study the amorphization process in more detail it is necessary to examine the defects induced by deformation. Figure 2.20 shows

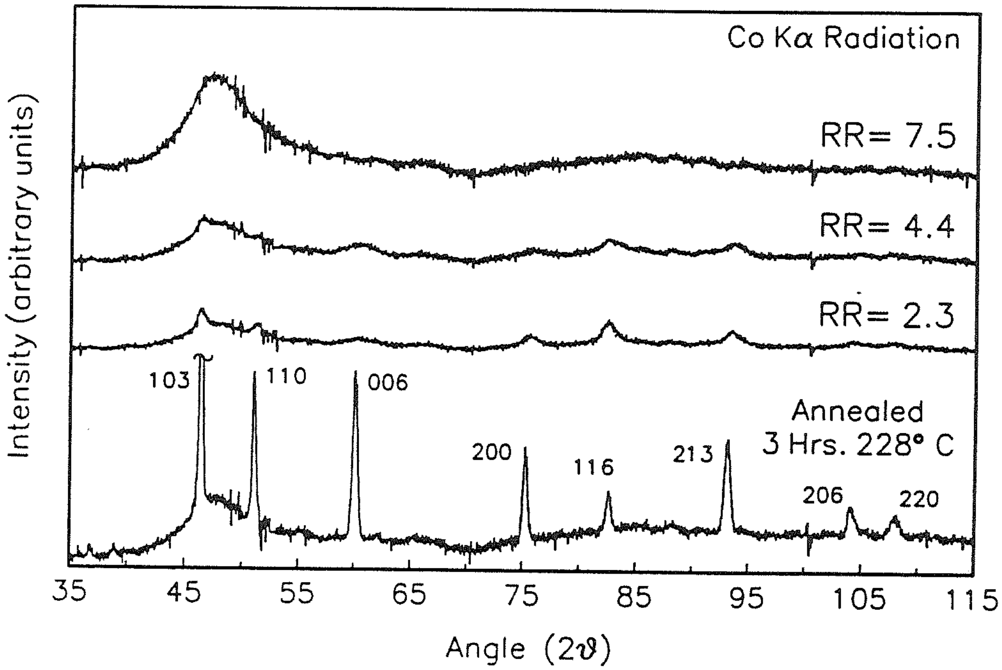

Figure 2.19. XRD patterns of a $Cu_{35}Ti_{65}$ ribbon after annealing at 228° C for 3 hours and after subsequent deformation. The [103] peak has been truncated for clarity of viewing.

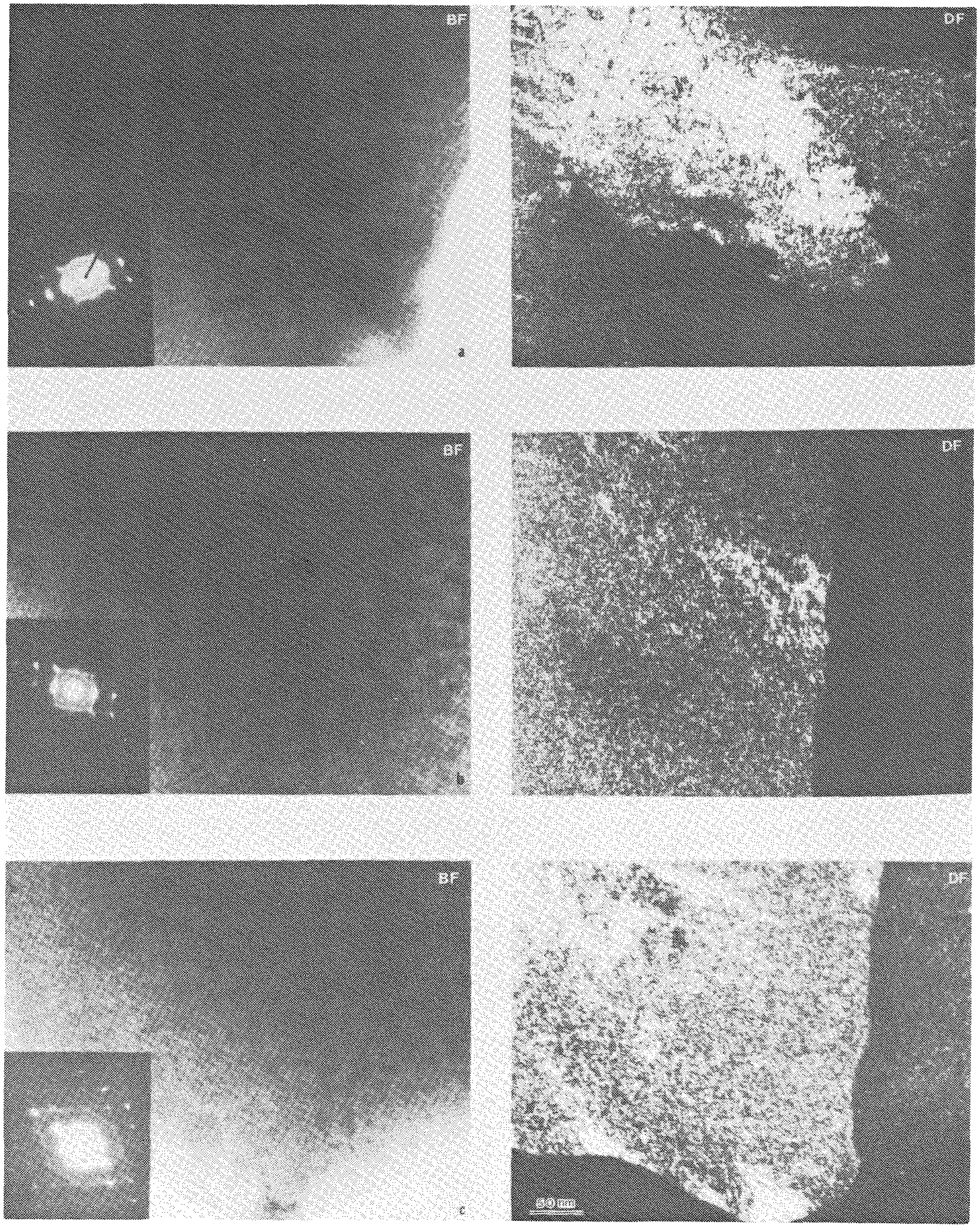

Figure 2.20. Three BF/DF/SAD trios show the high defect density present in large crystals at the free surface at RR=1.4. Note the sheets of diffuse scattering in the SAD patterns.

three bright–field/dark–field pairs of large crystals on the free surface of the ribbon at RR=1.4. The defect density observed is already too large to permit an individual study of the defects present. Sheets of diffuse scattering are observed in the diffraction patterns, ocurring in the {103} directions. These sheets are similar to those seen by Luzzi et al. during electron irradiation of γ–CuTi.[2.11] They may be due to strain or chemical disorder in the ordered crystal caused by the deformation–induced formation of antiphase boundaries (delineated by a superdilocation pair) lying on [103] slip planes. The [103] planes are equivalent to the [101] planes in one of the three bcc subcells present in the ordered $CuTi_2$ unit cell. These are the close–packed planes in bcc crystals and are the predominant slip system therein.[2.12] Antiphase domain formation would be expected on these planes if the crystals deform as if they were chemically disordered. This may be the case; the superlattice spots [002], [004], [008], and [0010] are effectively invisible in the diffraction patterns. Although the [116] planes seem to be the primary planes when a completely crystalline sample is deformed (see Figure 2.18), they are equivalent to bcc [112] planes, which are also a prominent slip system present in bcc materials.[2.12] Also, there are no isolated microcrystals in the latter sample, so it will probably deform differently than the other samples.

Luzzi et al. have suceeded in amorphizing the intermetallic compound Cu_4Ti_3 by electron irradiation.[2.13] They correlated the degree of chemical disorder, as measured by the Bragg–Williams long–range order parameter, with the onset of amorphization, concluding that chemical disordering plays the dominant role in this phase transformation. They also found this result during irradiation of the compound $CuTi_2$.[2.14] Although the defects produced by electron irradiation (predominantly point defects) are different than those produced by cold–rolling, both result in the creation of chemical disorder in an otherwise ordered intermetallic compound. Their conclusion is supported by their observations that the amorphous phase nucleates at antiphase boundaries. However, in this work amorphization is observed proceeding inwards from the crystal–glass interface. This is not unexpected, since it would be easier to grow the new glassy phase there than to nucleate it at antiphase boundaries, which are chemically but not topologically disordered. Luzzi et al. did not observe this because no such crystal–glass interfaces were initially present in their samples. In fact, in a rolling experiment the existence of an interface between the amorphous matrix and crystalline phase is necessary to initiate amorphization of the sample. The amount of deformation that can be accommodated in an ordered intermetallic is determined by the complicated interactions of the superdislocations and antiphase boundaries which are created. Thus, it may be difficult to store enough enthalpy in a fully crystalline sample to amorphize it solely by cold–rolling, especially when the same rolling direction is maintained. Even if the free energy of the crystal is raised high enough, because the majority of deformation–induced defects are linear and planar (and not point defects) there may still be a nucleation barrier which cannot be overcome unless the amorphous phase is already present. In ball milling, the higher temperatures may enhance atomic jump rates and thus facilitate nucleation. (Also, in ball milling the higher strain rates at which deformation occurs may result in the formation of defect structures different than those created during rolling. See Section 3.5 for a more detailed discussion.) In rolling, an interface between the crystal and amorphous matrix provides an existing site from which the new glassy phase may grow without storing the additional free energy required to overcome a nucleation barrier. Without such sites present, amorphization by cold–rolling does not occur before the crystalline ribbon disintegrates.

The non–equilibrium method of solidification used seems to be important only in determining how quickly amorphization proceeds. The initial samples, depicted in Figure 2.6, contained microcrystals that were grown during melt–spinning. Such rapid solidification not only may create non–equilibrium concentrations of defects such as vacancies, dislocation loops, and stacking faults,[2.15] but also may cause the resulting crystals to be slightly non–stoichiometric. Since $CuTi_2$ is a line compound, these two conditions could effectively result in a starting free energy which is already very close to that of the amorphous phase, meaning only a very small amount of additional chemical disorder would be needed to initiate amorphization. However, the samples monitored in Figure 2.19 also amorphize; in this case, the annealing presumably has both eliminated excess concentrations of the above defects and allowed the crystals to reach their equilibrium concentration. Thus, rapid solidification affects only the rate of amorphization, not whether or not it occurs.

Another factor which is important to amorphization is the mode of deformation in both sample morphologies. In the first samples, the majority of the ribbon consists of microcrystals embedded in an amorphous matrix. Here, the relative shear strengths and ductilities of the matrix and the crystals, as well as the nature of the interface between the two, is important. The amount of deformation measured for the entire sample may not be the same as that which the crystals undergo. In the annealed, polycrystalline ribbon, however, grain boundaries play an important role in the deformation process (note the development of a rolling texture in Figure 2.18). The fracture behavior of the crystal in the two environments will also be different; this means the maximum possible amount of free energy stored due to deformation before fracture of the crystal occurs will vary as well. The fully crystalline ribbon could be rolled to only RR=3.3 before disintegrating. The partially amorphous samples were rolled to deformation levels over twice that (although, as stated above, the actual deformation experienced by each grain or microcrystal may not be so exactly correlated). In ball milling, disintegration of the sample is actually favorable. In a rolling experiment, however, the crystals cannot continue to be deformed after significant fracture of the ribbon occurs. This is perhaps why glass need not be present for an intermetallic to amorphize during ball milling. In a rolling experiment, the initial presence of amorphous material is thus doubly important: it not only prevents fracture, allowing deformation to continue, but also eliminates the need to nucleate new glass as the microcrystals destabilize.

CHAPTER THREE: Wear

3.1 Introduction to Tribology

Wear is the change of a surface due to moving contact processes; the study of wear is called tribology. There are different types of wear: lubricated, adhesive, abrasive, etc. This introduction will focus on unlubricated adhesive wear, which is the category in which the present work lies. Adhesive wear is loosely defined as that which occurs under certain conditions during the rubbing together of two macroscopic bodies of comparable hardnesses. The adhesive force provides resistance against the separation of the two bodies, and is normal to their interface. Adhesion, or cold welding, is a result of surface atoms of one body lowering their energy by bonding to atoms on the surface of the other body. Friction is the force which resists movement in a direction parallel to the interface. Unlubricated simply means that there is no fluid used to reduce friction and wear by resisting the contact of the two surfaces.

Metallic surfaces are usually microscopically rough. When two macroscopically flat surfaces interact, contact actually occurs between the asperities which protude the most from the surface. Figure 3.1 presents a schematic representation of such contact. Two asperities approach each other at relative velocity v. There is a normal load F_n forcing the two together (a). There is a geometrical resistance to motion when they meet (b), increasing the frictional force. There is also resistance to further travel due to the shear and/or fracture toughness of the materials (c); this also contributes to friction. Both asperities deform a certain amount; for metals, this deformation is

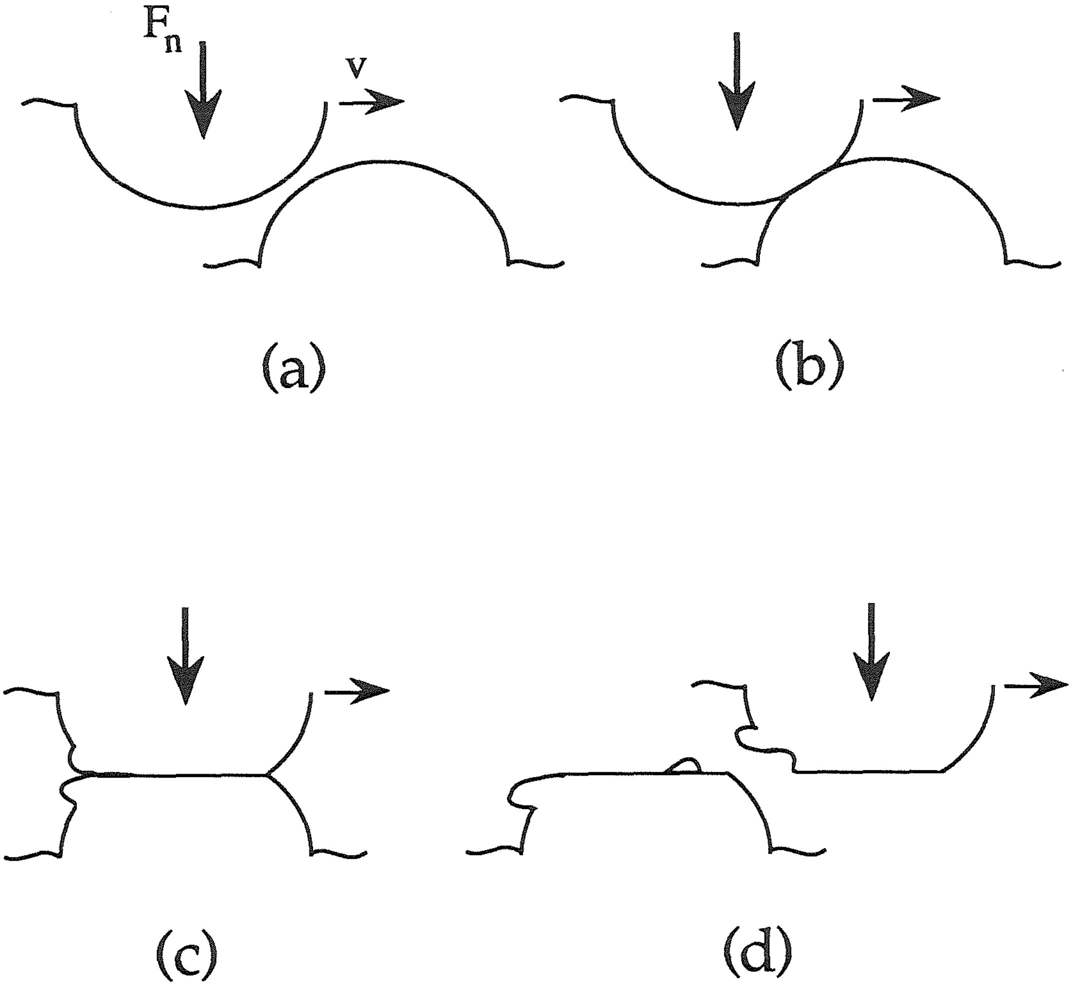

Figure 3.1. Asperity contact at the wear surface.

almost always plastic (d). The largest asperities are thus worn down or sheared off, and contact occurs between their remains and smaller asperities.

Sliding wear is a very inhomogeneous process. Many phenomena occur concurrently, and local conditions are determined by, for example, which areas of the surface are fractured or ploughed out by wear debris. The debris is composed of asperities and other material that has sheared off due to the large local plastic strains induced.[3.2] This material is then cold welded back to the surface, and undergoes more deformation. It is clear that the wear rate is highly dependent on the shear strength and fracture toughness of the material. Thus the asperities and debris at the surface experience a continual cyclical process of deformation, fracture, and cold welding. Because of this behavior, two nearby areas on the surface can have very different structures.

Because large strains are localized in the asperities, the local temperature can rise quite high. In his comprehensive review Quinn reports that local hot-spot temperatures can rise as high as 500° C.[3.3] This is highly dependent on the wear conditions, however. It is possible to perform a wear test at low speeds and loads, and thus substantially decrease the likelihood of locally high temperatures. Unfortunately, the few existing wear testing standards are poorly characterized and hard to compare directly; slightly different experimental setups, and even a small amount of surface oxide, give dramatically different outcomes.[3.4]

There have been few studies of phase transformations at the wear surface. Wert et al. found that the long–range order parameter in ordered Cu_3Au was reduced to $S=0.33$ by wear.[3.5] Wear–induced martensitic phase transformations have been observed as well.[3.6] Nanocrystalline phase formation in wear debris has been reported,[3.7] and may in fact be quite common.[3.2,3.4] It may thus be possible to induce amorphization at the wear surface. There is some interest in determining under which conditions this might occur: studies have shown that metallic glasses have favorable wear properties when compared with their crystalline counterparts.[3.8,3.9] Using the criteria discussed in Chapter One, $CuTi_2$ was chosen as a good candidate alloy to examine wear–induced amorphization.

3.2 Sample Preparation: Wear Testing

Typical wear testing is done with a pin–on–disk type machine, shown in Figure 3.2a. The "pin" is actually a steel ball which is forced onto the rotating disk of the material to be studied. A variant of this is often used when the subject material is more easily formed into a sheet; in this case the pin moves back and forth along the sample (Figure 3.2b). There are three disadvantages to these methods. First, the ability to form the subject material into large disks or strips is required. Second, just as in ball milling, the pin wears and contaminates the sample. Third, the damage is localized in a wear scar, which makes analysis by x–ray diffraction impossible and doesn't provide enough material for TEM.

To avoid these problems a unique wear testing configuration was employed. Samples consisted of ingots of the same alloy whose cut faces were worn against each other. An ingot of alloy was melted three times on a silver boat (see Chapter 2), with care being taken to turn the sample over between melts to insure homogeneity. The central section of the ingot was nearly

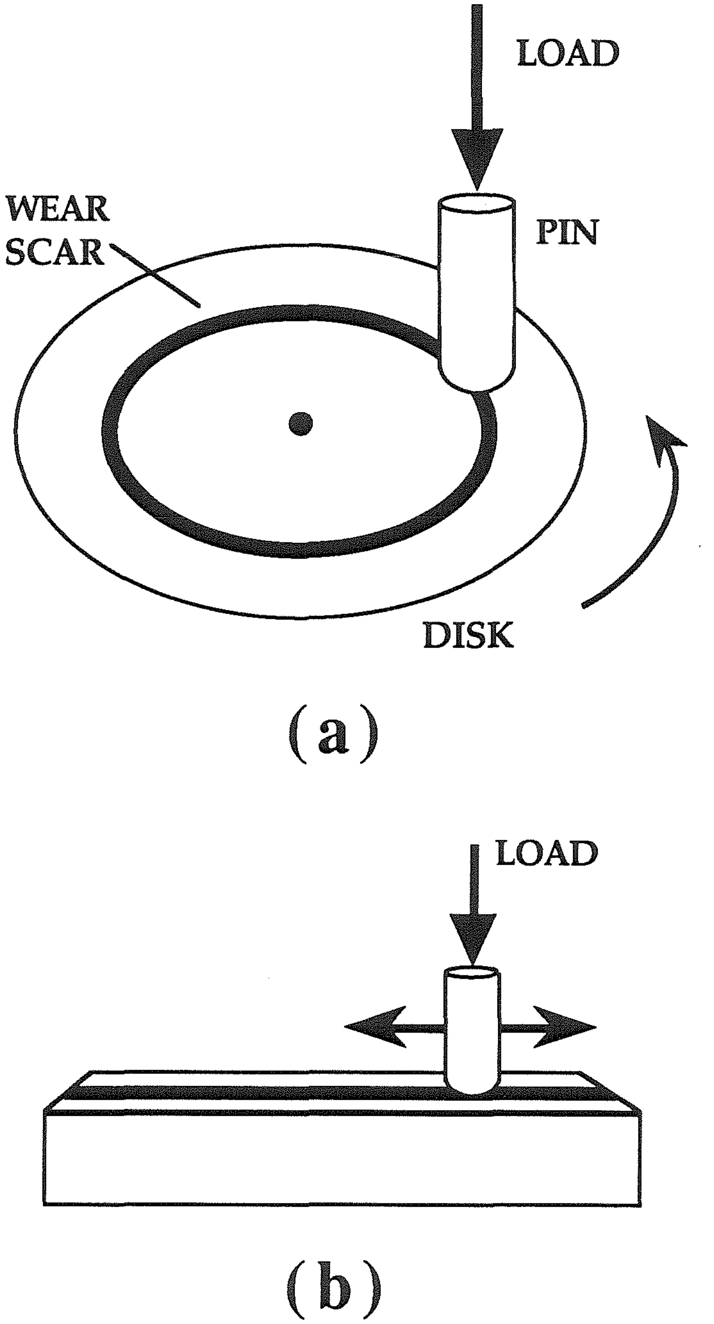

Figure 3.2. Two common wear testing setups: (a) pin–on–disk, and (b) pin–on–strip.

cylindrical in shape, with a radius of 3–4 mm. An ingot was sliced in half using a Buehler Isomet low speed circular saw with an Isocut blade. On each half another parallel cut was then made, resulting in two "slabs" of sample approximately 3 mm thick. These slabs were cleaned in acetone and methanol and affixed to aluminum sample holders with Duco cement. As depicted in Figure 3.3, they were then mounted in the ends of two aluminum cylinders and held in place by a retaining ring.

Figure 3.4 is a drawing of the wear apparatus. One of the cylinders was mounted on the shaft of a high speed motor (Dayton model #2M145, rated at 1/2 HP and 10,000 RPM); the other one was placed directly above such that the two sample slabs were touching. There is a pin pressure-welded to the second cylinder that rides in a vertical groove in a stationary collar and prevents rotation due to friction. The normal force could be varied by placing different weights on top of the cylinder; with no load the cylinder and sample weigh approximately 285 g. The angular velocity of the bottom cylinder was controlled with a variable transformer, and measured using a digital tachometer. The ambient humidity and temperature were also recorded. The entire device was placed inside a glove bag, and the experiment was performed in a flowing helium atmosphere. The bag was flushed twice before each run; the oxygen concentration near the sample was measured using a GC Industries 501 portable oxygen monitor and found to lie between 0.7 and 0.9%.

The temperature of the sample during typical wear conditions was measured as follows. Two thermocouple (Chromel–Alumel) leads were spot welded onto the side of the stationary ingot, approximately 3 mm from the surface. The average steady–state temperature at the wear surface was

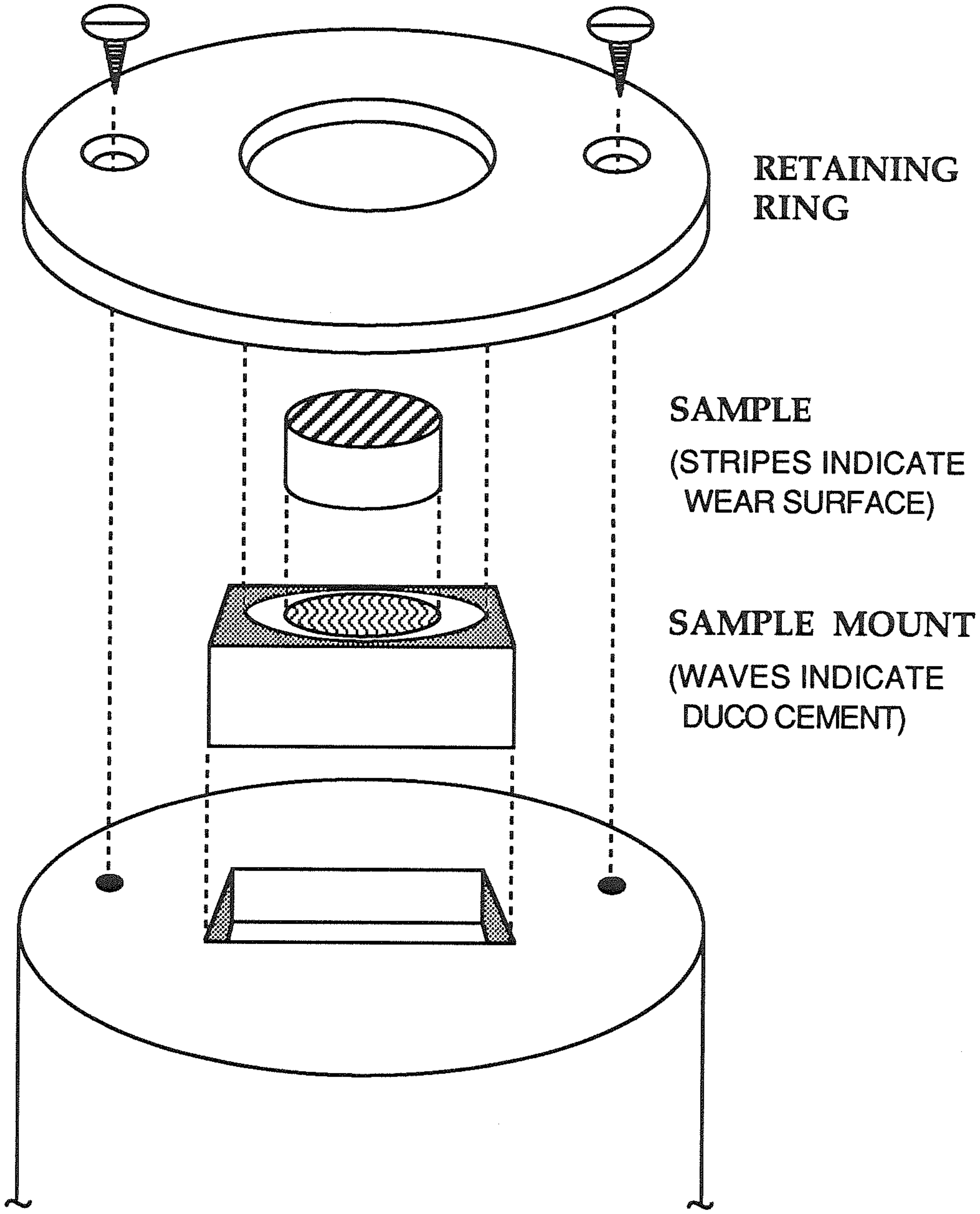

Figure 3.3. Sample holder for the wear apparatus.

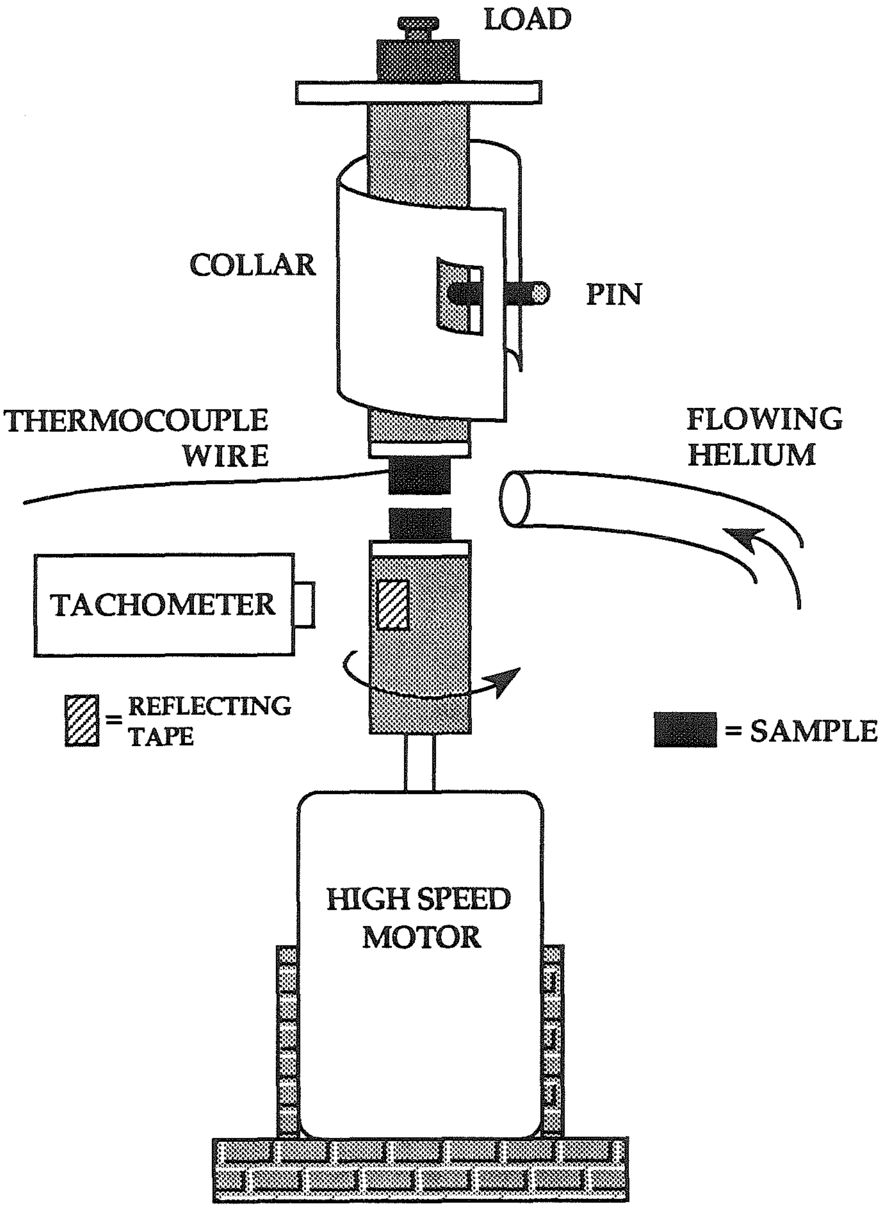

Figure 3.4. Schematic illustration of the wear apparatus.

estimated using the formula for a semi–infinite rod with the end maintained at the constant temperature T_{surf}:[3.10]

$$T_{surf} = T_{meas} \exp\left(x \cdot \sqrt{\frac{Hp}{aK}} \right) ,$$

where T_{meas} is the temperature measured at a distance x from the wear surface, a is the cross–sectional area of the rod and p is its circumference, K is the thermal conductivity of the ingot, and H is the coefficient of linear surface heat transfer. Although K has not been measured for Cu–Ti intermetallics, the thermal conductivities for most copper and titanium alloys have a published value of about 0.2 W/cm-°K. H is about 1.5×10^{-2} W/cm^2-°K for the He flow rate used.[3.10] The perimeter p of a typical ingot is about 2.67 cm with a=0.56 cm^2. The highest recorded value of T_{meas} was 38° C, which was reached after about fifteen minutes into the experiment. This gives the average temperature of the wear surface as 44° C. (This is actually an overestimate, because the sample rod is not semi–infinite and the deposition of heat at the surface increases with radial distance from the central axis of rotation.) Of course, temperatures at asperities could be considerably higher.

Initially it was thought that x–ray diffraction could be used to monitor the progress of the experiment, as in the cold rolling studies. The sample holder configuration allows samples to be removed and replaced quickly for just this purpose. This was reasonable because in most published work wear damage of varying degrees is shown to extend tens of microns below the wear surface itself.[3.11] This is much greater than typical x–ray penetration depths (see Chapter Two). When XRD was performed on the present samples, however, there was very little difference between the patterns taken before and after wearing. To sample more of the surface and less of the bulk, XRD patterns were taken at a low fixed incident angle α of 10°–15°. In this case the fraction of signal coming from a depth d below the surface is given by[3.12]

$$F_D = 1 - e^{-\mu d\left[\frac{1}{\sin\alpha} + \frac{1}{\sin(2\theta-\alpha)}\right]} .$$

(Note that for the θ–2θ geometry, $\alpha=\theta$ and this formula reduces to the one given in Chapter Two.) For the lowest α practical, $\alpha=10°$, the range of penetration depths is $1\frac{1}{2}$ –3 μm. Unfortunately, this configuration did not produce more acceptable results; there was a very slight broadening of the diffraction peaks of the worn sample, but not enough for an effective crystal size or strain broadening analysis to be performed.

It seems that the most severe wear effects and extensive subsurface deformation are widely distributed over the sample. This may be due to the wear configuration used; unlike more commmon wear setups, such as pin–on–disk, the load is distributed over the entire area of both surfaces. Figure 3.5 is an optical micrograph of the wear surface. Rather than one wear scar, many grooves and ridges a few microns wide are formed. Also visible are areas consisting of material that has been fractured off, deformed, and cold–welded back onto the surface. Although some of these worn regions are undoubtedly more than three microns deep, and subsurface deformation has occured, they may be small in volume fraction relative to the whole surface layer and thus

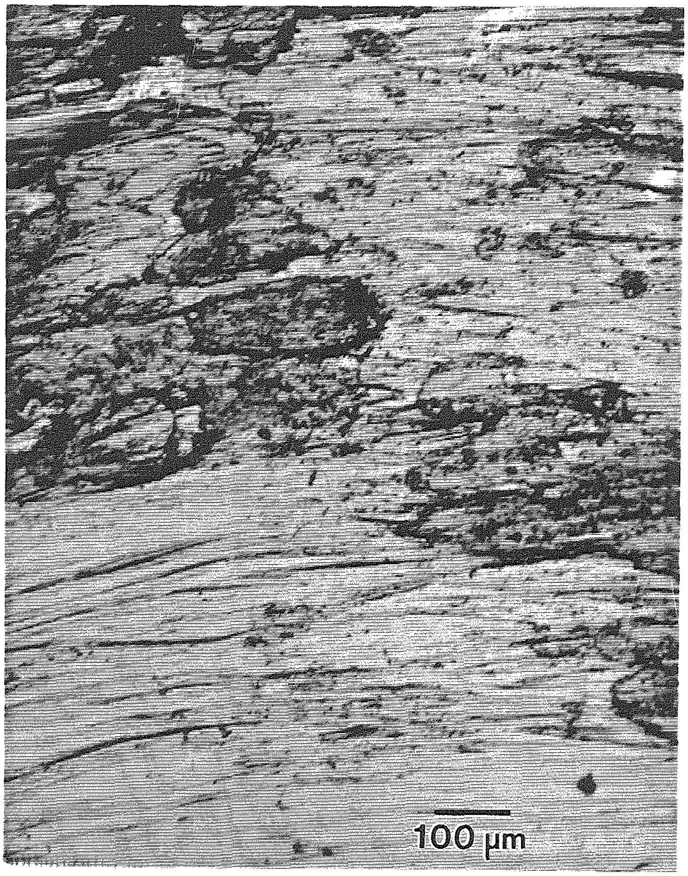

Figure 3.5. Optical micrograph of the wear surface (magnification = 100×).

do not contribute significantly to the x–ray diffraction signal.

For the pictured sample, the parameters of the experiment were representative. The temperature was 21° C with about 25% relative humidity. The load was 500g, and the rotation speed ranged from 1000 to 1900 RPM. The sample was worn for about $1\frac{1}{2}$ hours. The speed varied because of the creation and destruction of asperities due to material fracture and transfer, varying the coefficient of friction. Also note that the relative contact speed experienced by a given area of the wear surface varied with its radial distance from the center of the ingot. However, no significant differences were found between surface areas at different radii or between samples whose rotational speed remained in the above range.

3.3 Sample Preparation: Transmission Electron Microscopy

An excellent way to examine the structure of the wear surface is by TEM. There are two methods that can be used. The surface can be sliced off; the resulting sample is then back–thinned from the opposite side only, leaving a specimen whose thinnest areas are presumably right at the surface. This technique has the advantage of creating relatively large thin areas of the surface for viewing. However, because of the unevenness of a wear surface, plane–view microscopy is not able to provide accurate depth information. This can be obtained by using cross–sectional TEM. The illustration in Figure 3.6 compares these two techniques. Cross–sectional TEM involves thinning the sample perpendicular to the desired surface, giving a complete depth profile of the sample. However, sample preparation is much more

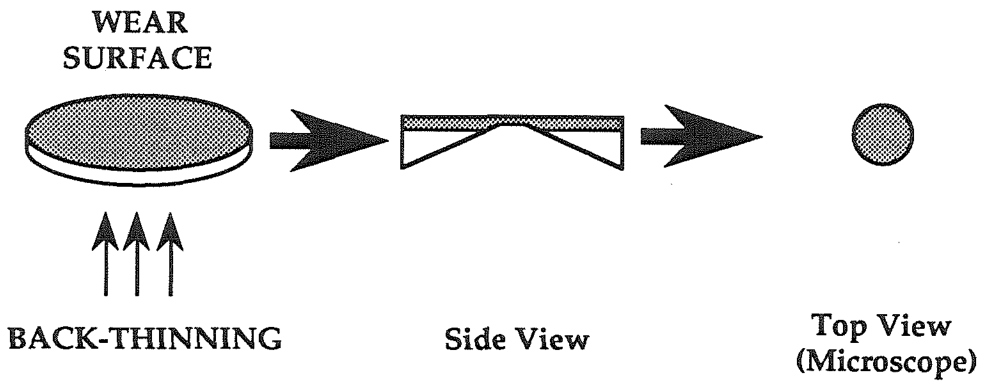

Plane-view Sample

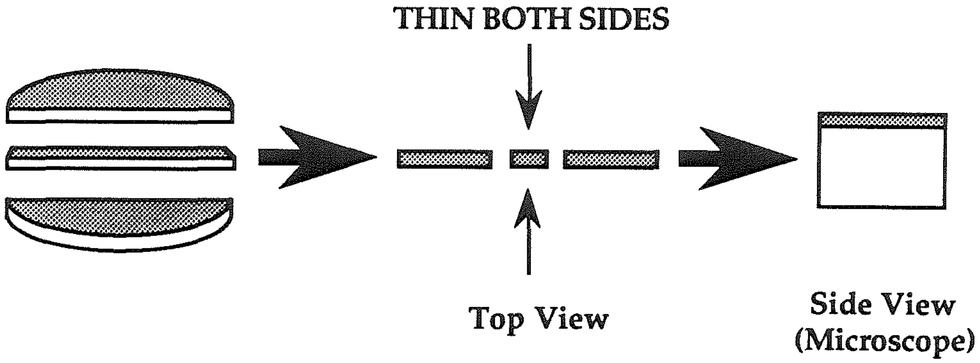

Cross-section Sample

Figure 3.6. Comparison of plane–view and cross–sectional microscopy.

complicated and difficult than for plane–view TEM, and the thin region obtained is much smaller.

The usual steps in preparing a cross–section are as follows (see Figure 3.7). First the sample is sliced about $1\frac{1}{2}$ mm parallel to the surface, or interface, in the case of multilayers (a). Two– to three–millimeter–wide strips are cut from this (b). Then a cut is made through the surface, halving the strip, and the two pieces are bonded together "bookend" style (c). This serves two purposes: it provides in effect twice the sample to view at once, and it protects the surface from damage during the thinning process. Three–millimeter–long pieces are then cut from the sample, and attached to a block (d) with crystal bond, a hard resin that melts at only 70° C. After wet sanding to 600 grit (e), the sample is polished on a Buehler Minimet orbital polisher first using 3 μm then $\frac{1}{4}$ μm grit diamond paste (f). A 3 mm TEM grid is then affixed to the sample with five minute epoxy (g). After curing, the crystal bond is removed with acetone and the sample is flipped, with the grid side now bonded to the block (h). After sanding (i), the sample/grid is removed and fastened to a dimpling block, grid side down (j). The dimpler is a machine which abrades the central section of a sample at a very slow rate, using diamond paste as above. When the sample is dimpled thin enough (k), it is put into an ion mill for final thinning (l).

Unfortunately, following this procedure to cross–section the wear samples was impossible. To begin with, two halves of the wear surface could not be bonded together to form the initial cross–section. The surface was too rough for the usual adhesives, such as M–Bond, to successfully harden in place. A more viscous glue, like five minute epoxy, was needed. However, any

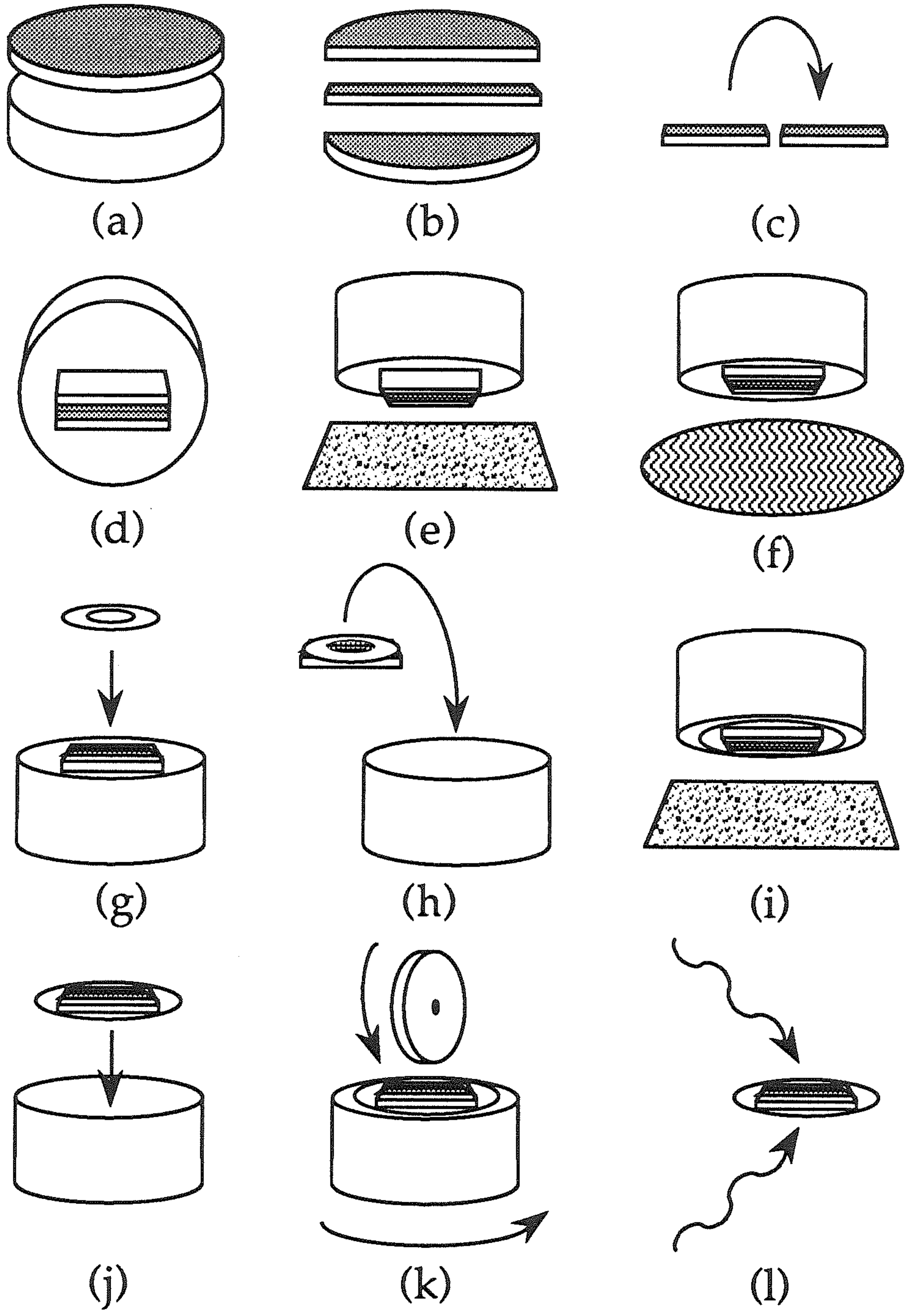

Figure 3.7. Ususal steps for preparing a TEM cross–section (see text for details).

glue used at the cross–section must be well behaved during ion milling; it cannot smear out over the sample, and should have a similar milling rate to the alloy. Unfortunately, there are no commercially available adhesives that meet these criteria. After many attempts, it was decided to abandon the attempt to bond the two wear surfaces and instead coat the sample with a substance that, when hardened, would mill at similar rates to the alloy. To this end a series of tests were made, and a likely candidate was found: Torr Seal, a low vapor pressure resin, which is normally used as an ultra–high vacuum sealant. However, after experimentation it was found that certain other steps in the process had detrimental effects on the Torr Seal. It is dissolved both by acetone, which is used to clean the crystal bond off the sample at various sample preparation stages, and by the lubricant used with the diamond paste, Metadi fluid.

Thus it was necessary to devise a modified cross–section sample preparation procedure (see Figure 3.8). The wear surface was sliced off (a) and cut into pieces, each about 3 mm long and $1\frac{1}{2}$ mm deep (b). The sample was placed into Torr Seal, wear side down, and then both were slightly heated to cure the resin (c). The side of the sample was then mounted perpendicularly to a sanding block with crystal bond (d). After wet sanding to 600 grit (e), the sample was removed from the block not with acetone but by heating to melt the crystal bond. Rather than being polished, the sample was then mounted to a dimpling block (again with crystal bond) and dimpled just until smooth (f). The abrasive/lubricant used was Syton, a colloidal silica suspension that polishes finer than $\frac{1}{4}$ μm grit diamond paste. A TEM grid was affixed to the dimpled side of the sample with five minute epoxy (g). The

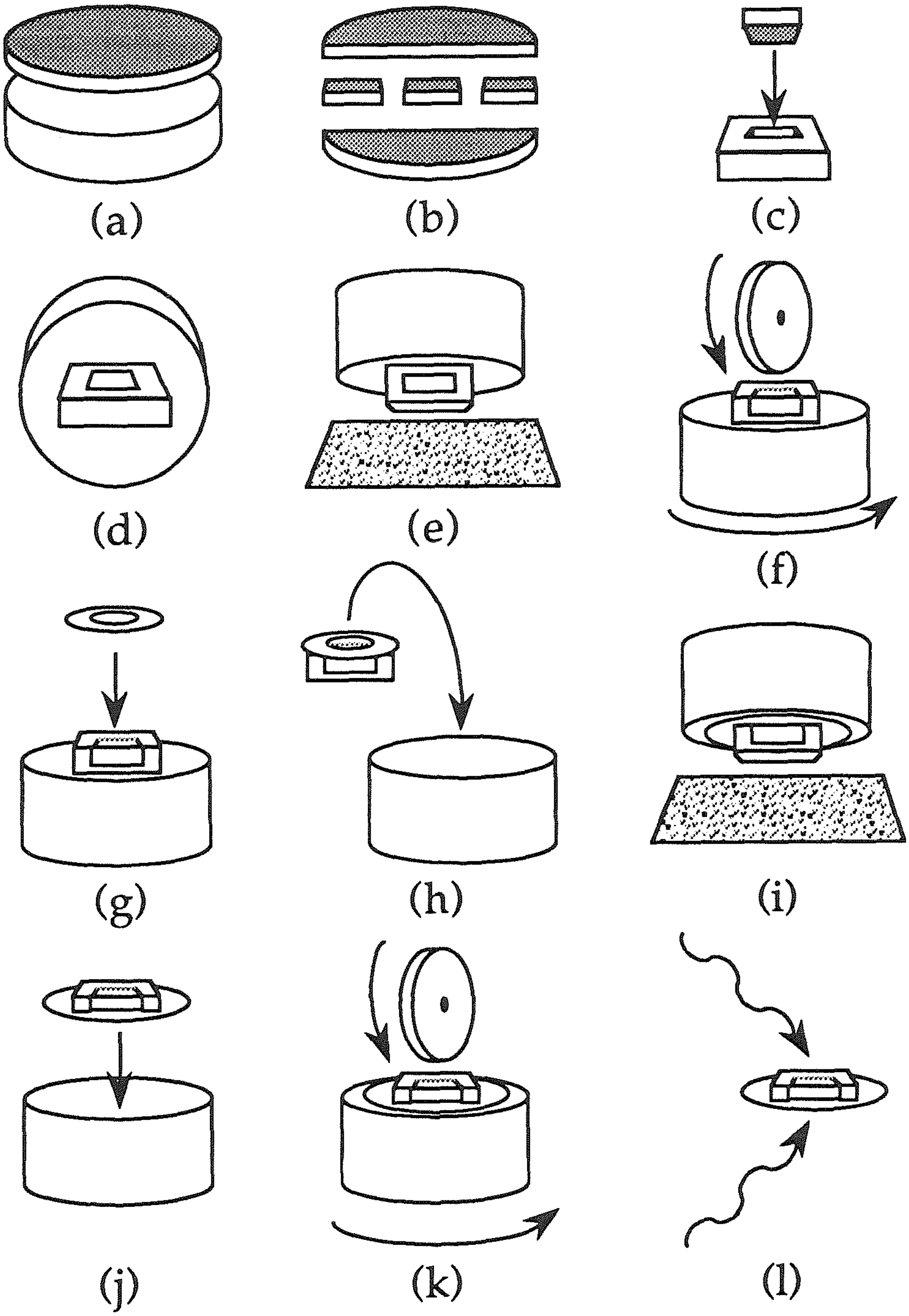

Figure 3.8. Modified procedure to produce a TEM cross–section of a wear sample (see text for details).

sample was then turned over and remounted (h); the other side was sanded down to 600 grit, until the sample was approximately 150 μm thick (i). The specimen was removed and fastened to a dimpling block, grid side down (j), and dimpled using Syton (k). Although Syton does not dissolve the Torr Seal as does Metadi fluid, it requires many more hours to thin a sample. When a small hole was produced, the sample was removed from the crystal bond, again with heat. Remaining crystal bond was attempted to be removed by careful swabbing with acetone. There was an unfortunate tradeoff between dissolving the undesirable crystal bond still covering the sample and dissolving the Torr Seal; inevitably, some crystal bond remained, while some Torr Seal was dissolved. Finally, the sample was milled in an ion mill (l) for over 12 hours; the milling conditions were 5.7 V, 0.9 mA, and 7×10^{-5} Torr at a 15° incident angle. Microscopy was performed on Philips 301 and 430 microscopes.

3.4 Transmission Electron Microscopy

3.4.1 Plane–view Microscopy

The wear surface was first examined using plane–view TEM. Figure 3.9 is a BF/DF/SAD trio of the wear surface. The microstructure at first glance appears to consist of microcrystals embedded in an amorphous matrix. The crystals range from 5 to 17 nm. The diffraction pattern is polycrystalline, with a faint amorphous halo inside the first ring. This halo can be better discerned in Figure 3.10. The structure observed is very similar to that in the previous figure. Here the crystals are 2–15 nm in size.

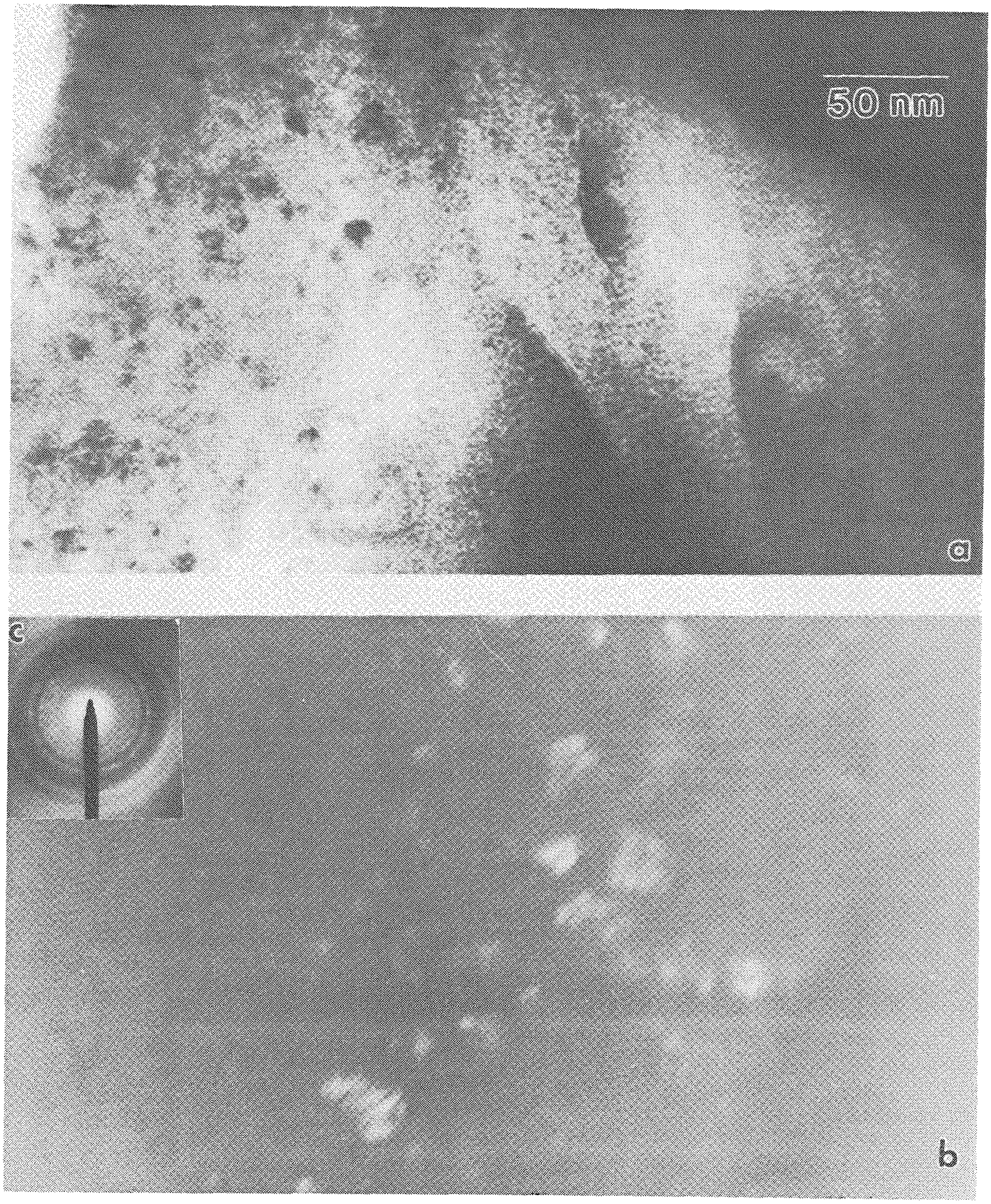

Figure 3.9. BF(a)/DF(b)/SAD(c) trio of the wear surface. Crystallite size is 5–17 nm. Blurring in (b) is due to drift during the long exposure.

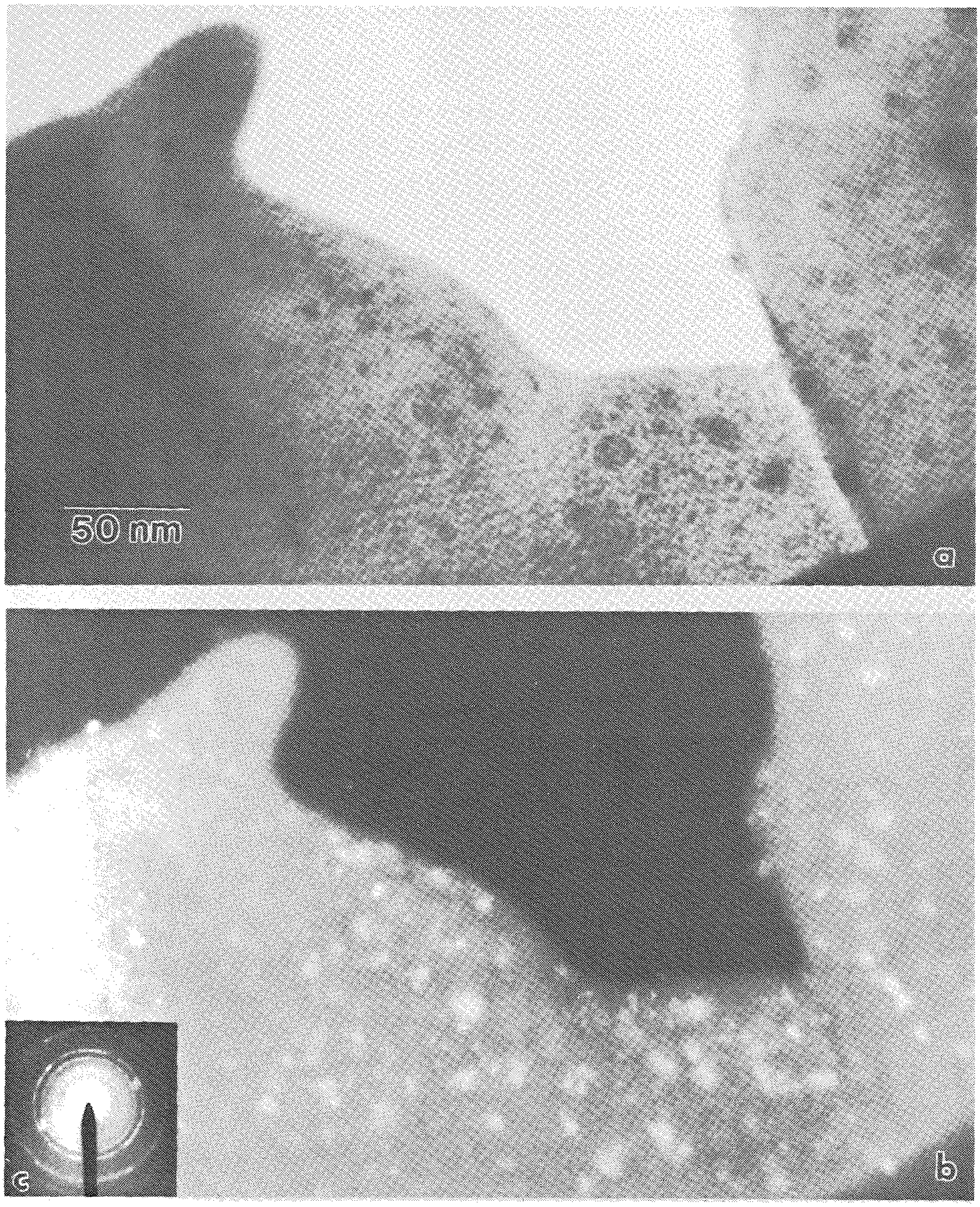

Figure 3.10. BF(a)/DF(b)/SAD(c) trio of the wear surface. Crystallite size is 2–15 nm. Note the diffuse inner halo.

In Figure 3.11 a bright–field image of the surface is accompanied by two dark–fields taken at different tilts. The first is taken from the ring faintly visible in the diffraction pattern. It shows that this area of the surface consists not only of a large single crystal (as evidenced by the spot pattern) but also many nanocrystals, less than 3 nm in size. The second dark field is taken from one of the spots in its companion SAD. This illuminates the single crystal present.

3.4.2 Cross–sectional Microscopy

Cross–sectional microscopy was performed to obtain depth information. Figure 3.12 contains a BF/SAD pair taken below the wear surface. Figure 3.12b is an overview; the arrow points to the area of the sample where the bright–field (a) was taken from, located about 65 μm from the wear surface (which is indicated by WS). There are one or two large crystals present at this depth. The SAD exhibits large amounts of diffuse scattering.

Figure 3.13 is a BF/DF set of micrographs of the wear surface itself. Torr Seal is plainly visible in the bright–field image (a); its presence indicates that is is indeed the wear surface in the picture. Figure 3.13c is an SAD of the Torr Seal; it has a very diffuse, almost continuous halo. This was recorded to insure that a halo in a diffraction pattern was from the sample and not from the Torr Seal. The dark–field picture (b) was imaged from a "spot" on the inner ring, thus illuminating any large crystal as well as nanocrystals. The broad ring is composed of two more narrow rings; however, in some places these rings appear to be broadening into a halo. The crystals present are

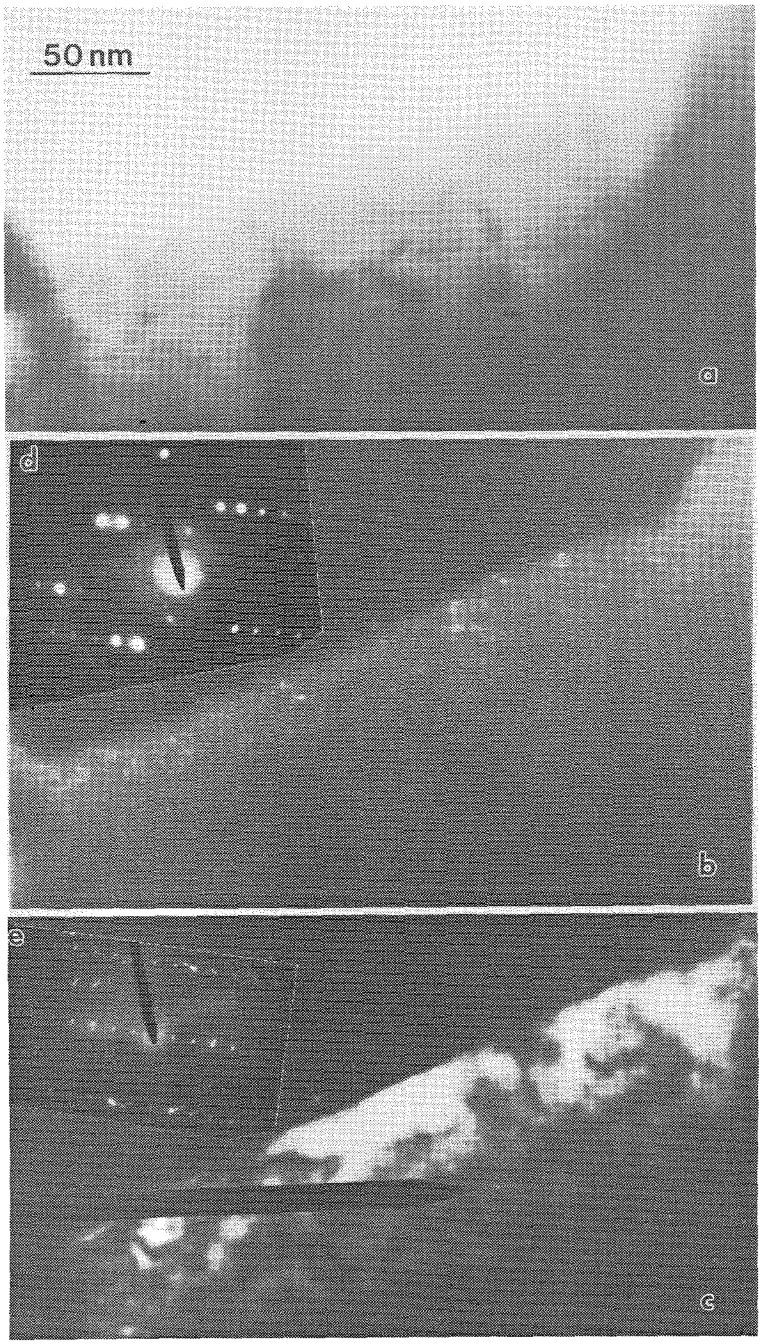

Figure 3.11. Bright–field image (a) of the wear surface and two dark–field images (b) and (c) taken at different tilts, along with their respective SAD's (d) and (e).

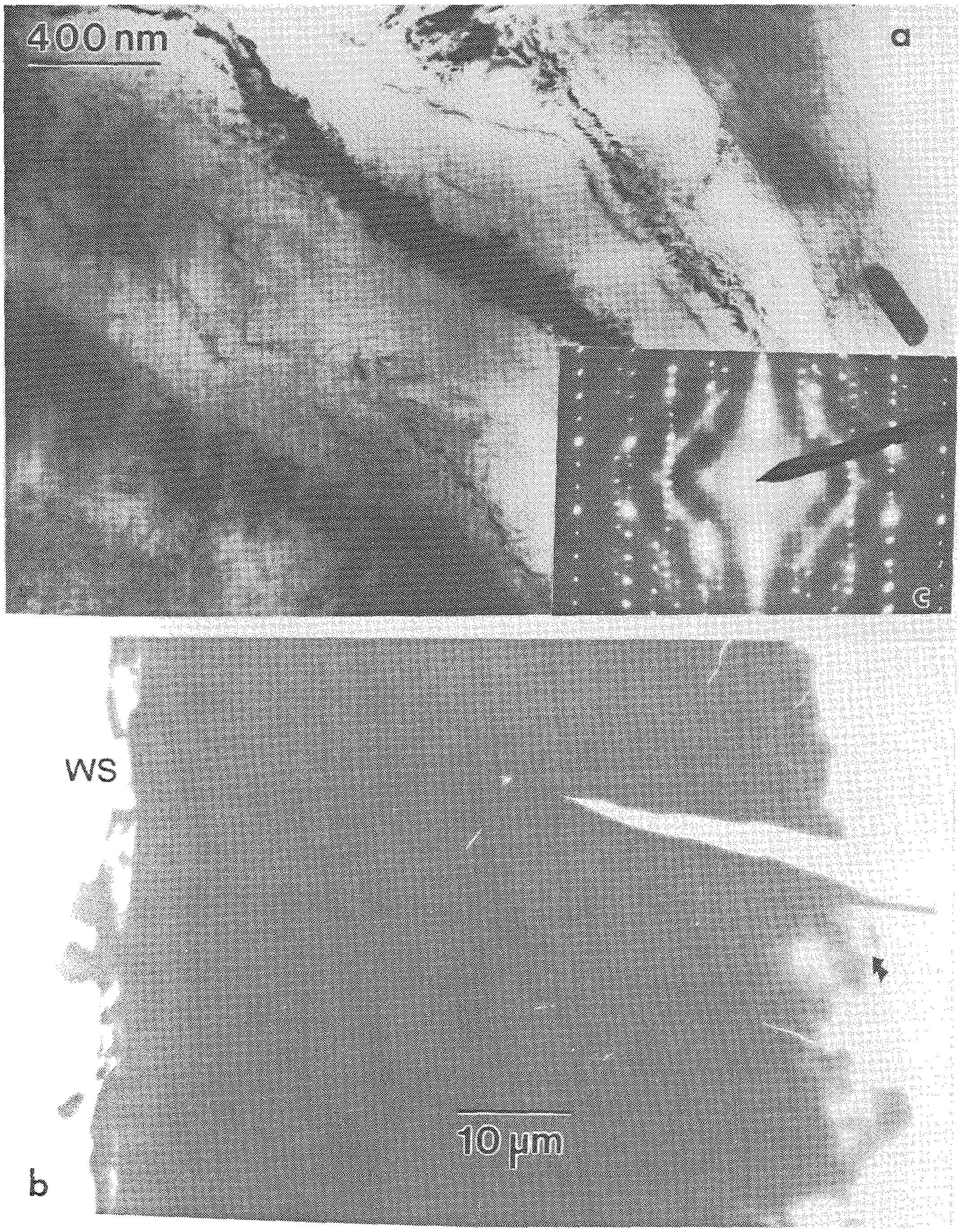

Figure 3.12. BF (a) taken 65 μm from the wear surface (denoted by "WS" on overview (b)). The location of the magnified region is indicated by the arrow in (b). Note the diffuse scattering in the SAD (c).

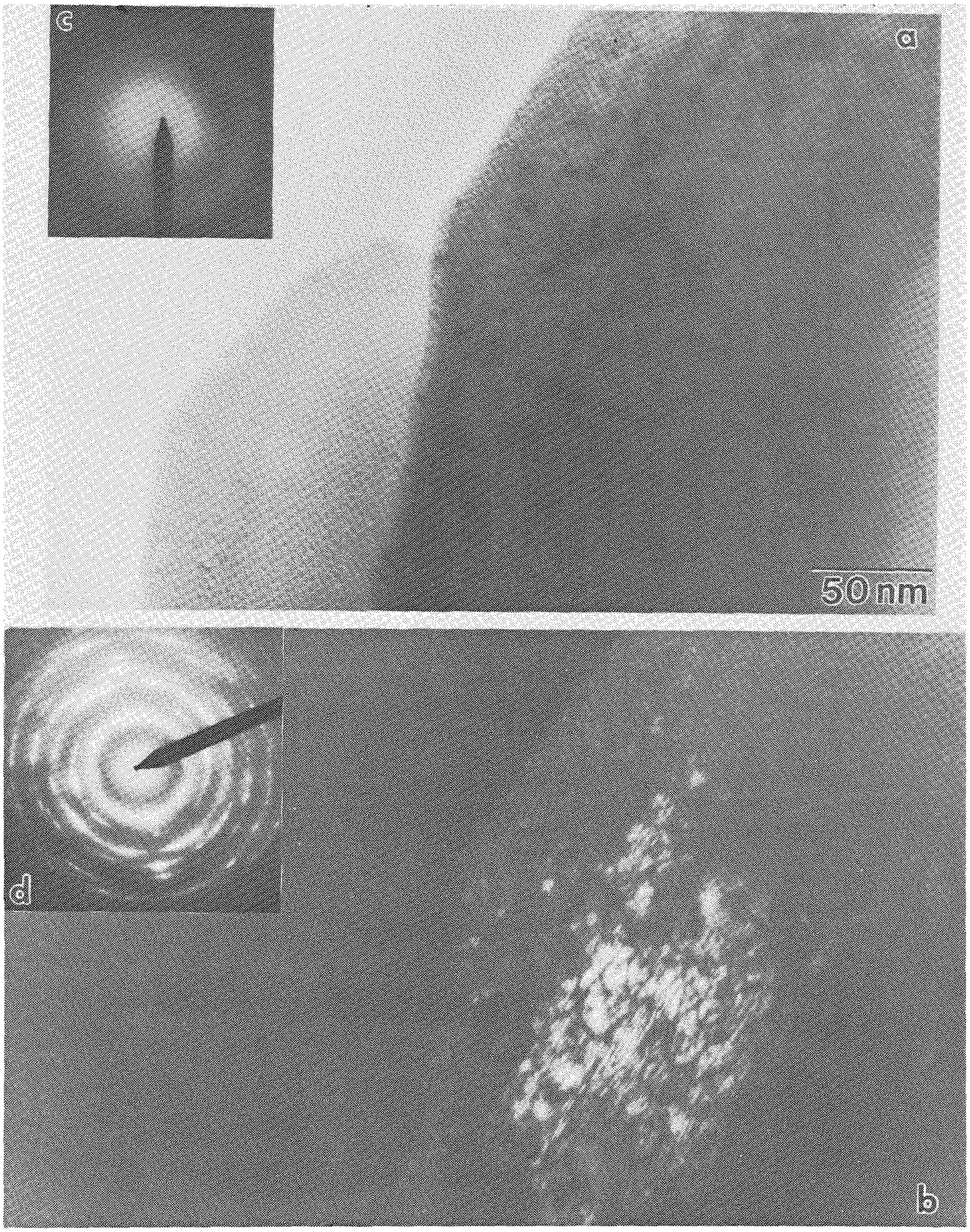

Figure 3.13. BF(a)/DF(b) pair showing Torr Seal at the wear surface. (c) is the SAD of the Torr Seal; (d) is the SAD of the sample. There is a layered structure visible, especially in (b).

anywhere from less than 2 nm to 10 nm in size. There is a layered structure visible in both the bright–field and dark–field images.

A similar microstructure is observed in Figure 3.14. The SAD contains a broad band, usually associated with the amorphous phase. Unlike Figure 3.13d, there are only faint remnants of sharper rings barely visible within the band, as well as a few isolated spots present. The structure here is extremely fine–grained, ranging from 3 nm to apparently below 10 Å.

A larger range of crystal sizes is present in Figure 3.15. Near the surface, the structure at first glance appears to be amorphous, although at least one sharp ring is visible within the broad band in the diffraction pattern. The dark–field indicates crystal sizes here of less than 10 Å; also visible are crystals up to 15 nm in size. A pair of high–resolution micrographs enlarged from this area is presented in Figure 3.16. The sample within at least 50 nm of the surface is now ostensibly seen to be nanocrystalline. The "grains" range from 16 Å to below 8 Å. Most of the lattice fringes seem to be aligned in the same general direction.

3.5 Discussion

The appearance of supposed nanocrystals less than 10 Å in size raises once again the questions of what structure constitutes the amorphous phase, and what stages a crystal goes through as it becomes a glass. The transformation of polycrystals into a nanocrystalline or amorphous phase does seem to depend on the degree and type of deformation induced. In Figure 3.12, diffuse scattering in the SAD is sharply indicated. It lies in the same

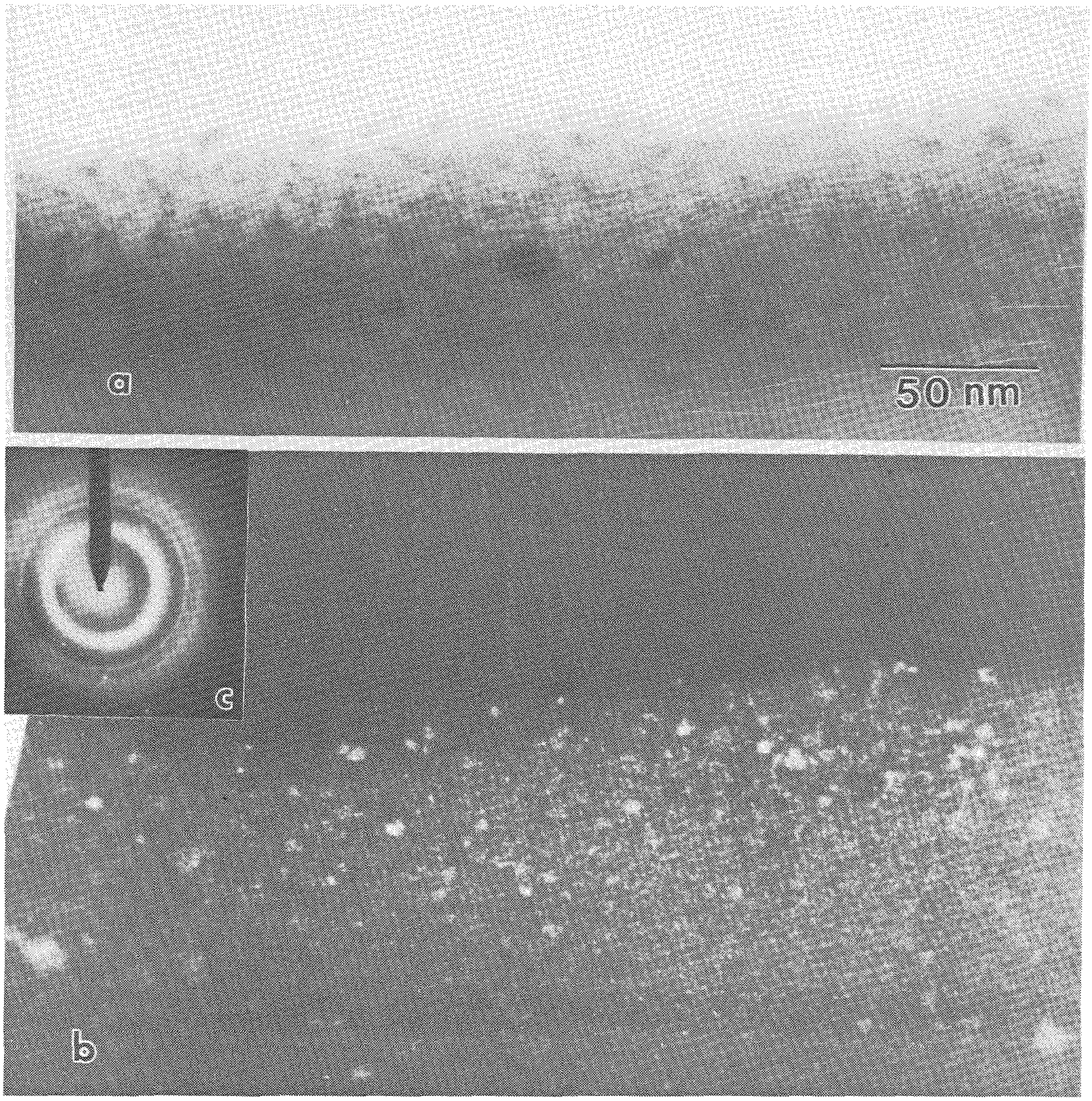

Figure 3.14. BF(a)/DF(b)/SAD(c) trio showing fine nanostructure at the wear surface. (c) contains a broad diffraction band.

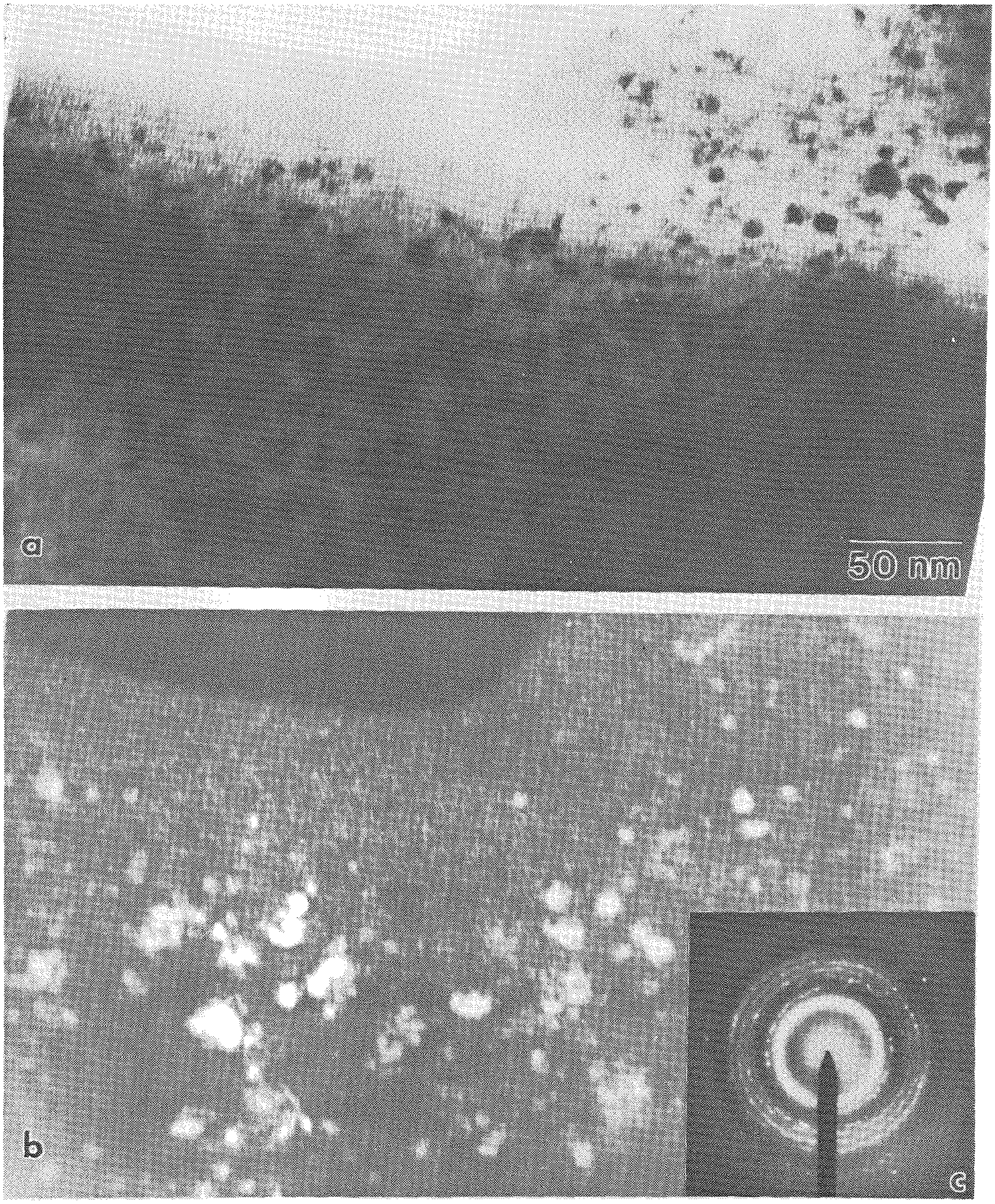

Figure 3.15. BF(a)/DF(b)/SAD(c) trio showing distribution of crystal sizes at the wear surface.

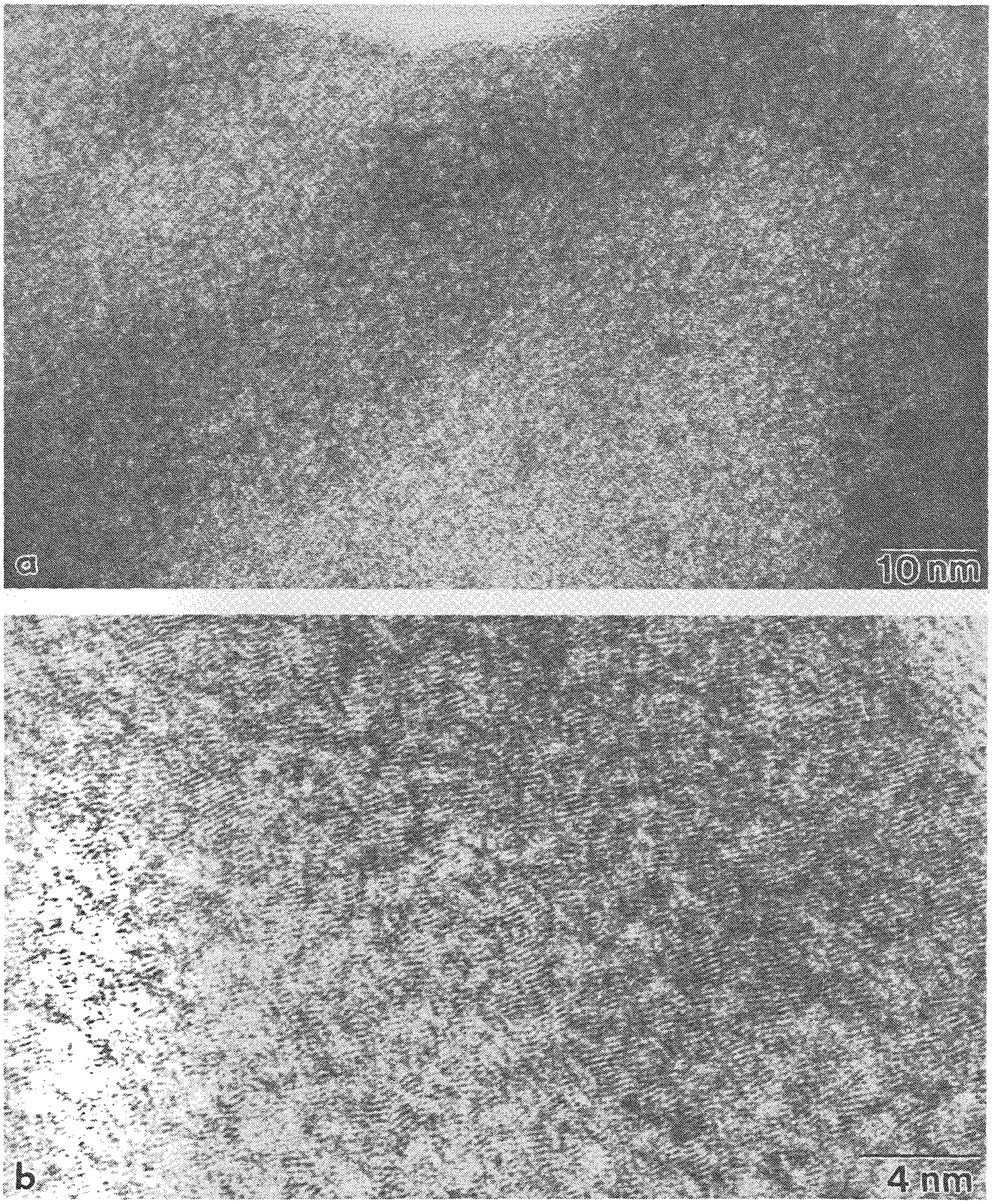

Figure 3.16. High resolution magnifications of Figure 3.15(a).

directions as the streaks discussed in Chapter Two. This crystal lies well below the wear surface; at this depth, the only wear effect is plastic deformation. It is thus not unexpected to see similar effects in both these crystals those deformed by rolling.

Near the surface, however, damage processes are more energetic; there is fracture, ploughing, and cold welding occurring, simultaneously in some regions. Here crystals may deform quite differently than those below the surface do. In addition, although the direction of wear is constant, a piece of the surface that has fractured off and cold welded back on will experience a new relative shear direction if it is oriented differently than before. Such particles may undergo conditions more similar to those that occur during ball milling.

One large surface crystal is depicted in Figure 3.11. Rather than exhibiting diffuse scattering, the single crystal spots are streaked in a circular manner. This may be a precursor to a polycrystalline ring pattern. It is possible surface strain rates are large enough so that rather than forming a somewhat stable configuration of antiphase boundaries, which would produce diffuse scattering, dislocations form pile–ups and tangles which collapse to form a grain boundary or crack.[3.13] At first, grains thus formed would be aligned; as deformation continues, their orientations would gradually become decoupled. This would result in a smearing out of the diffraction spots, similar to that seen in Figure 3.11. Continuing deformation, including fracture and cold welding, would result in smaller grain sizes and complete misorientation due to grain rotation and the accompanying formation of a ring pattern. If, however, strain rates are great enough, and grain sizes small enough, deformation may occur in such a way as to bypass continued grain boundary sliding, resulting in a fine, but aligned, grain structure.

Such fine–scale deformation structures are perhaps what are present in Figure 3.13. There are layers of some sort present, clearly visible in the dark–field micrograph. The layer spacing varies from 10 Å to 20 Å, and the layer direction is somewhat consistent. These layers may be due to deformation twinning, which is seen in all bcc transition metals deformed at high strain rates.[3.13] The smallest twinning unit consists of six [112] lattice planes. These are equivalent to [116] planes in $CuTi_2$, which have a spacing of 1.36 Å. (The disordered structure of $CuTi_2$ is bcc; see Section 2.5 for a more detailed discussion.) Thus the smallest possible layer spacing is about 8 Å, which is in agreement with observation.

These layers are similar to those seen in worn $Fe_{55}Cr_{33}B_{12}$, a good glass–forming alloy patented by Amtech Incorporated as Armacor–M^{TM} for use as a wear coating. A 3 mm thick coating of the alloy was hot welded to a steel substrate using a metal–inert–gas torch and severely worn with an unlubricated abrasive grinding wheel. The resultant wear scar was smooth enough for the conventional sample preparation procedure for cross–sectional TEM samples to be followed (see Figure 3.7). Figure 3.17 contains a BF/DF/SAD trio of a typical area of the wear surface. There is a large number of parallel layers visible, occurring at spacings down to less than 8 Å. This value roughly corresponds to the one derived from the superlattice spots visible in the Figure 3.18c, which arise from 7.26 Å structures. The lattice parameter of the bcc Fe–Cr solid solution is approximately 2.87 Å, which leads to a value of 1.17 Å for the [112] interplanar distance. This gives the

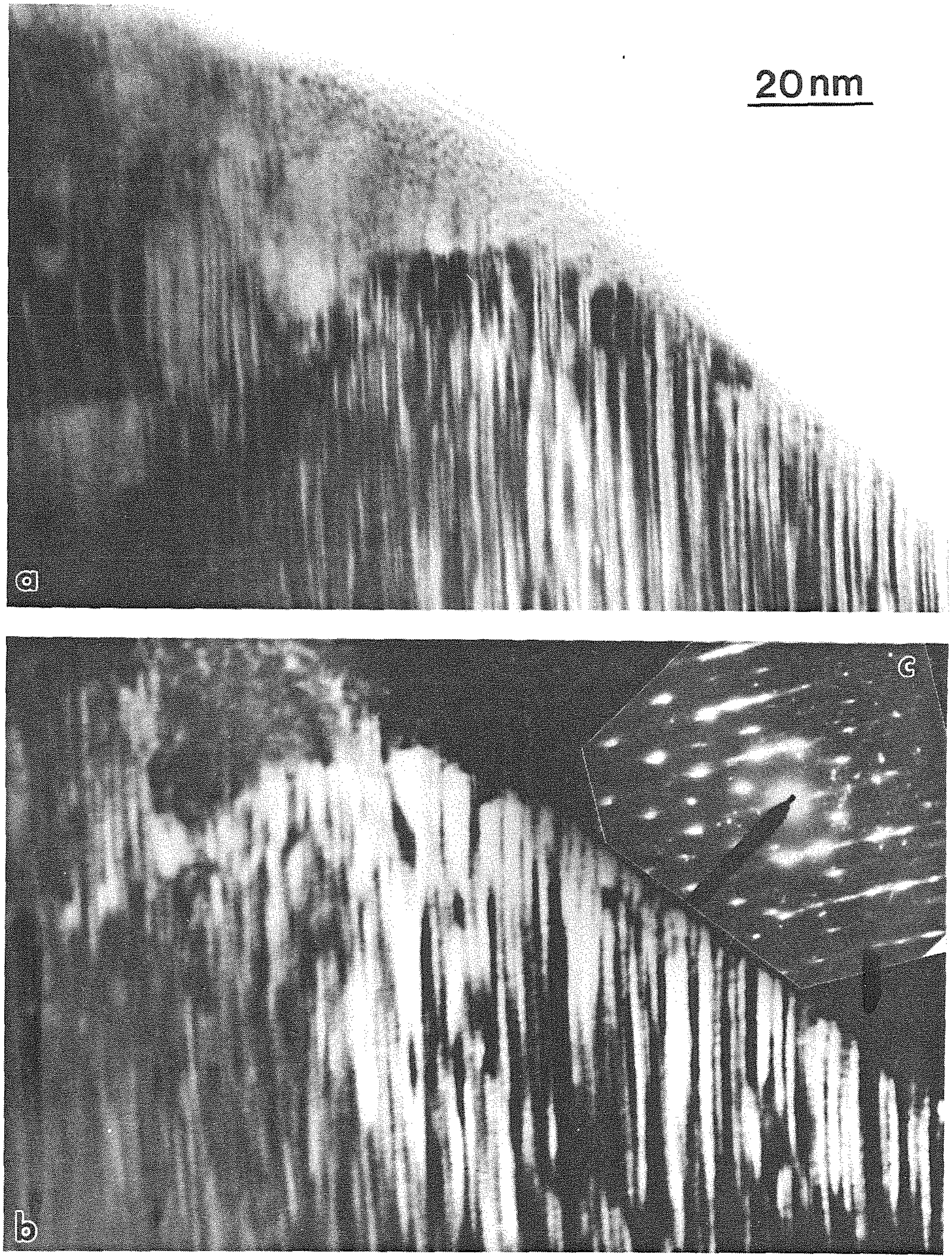

Figure 3.17. BF(a)/DF(b)/SAD(c) trio of a typical cross–section of the wear surface of Armacor–M$^{\mathrm{TM}}$. The small disordered region at the surface is probably an artifact of ion milling.

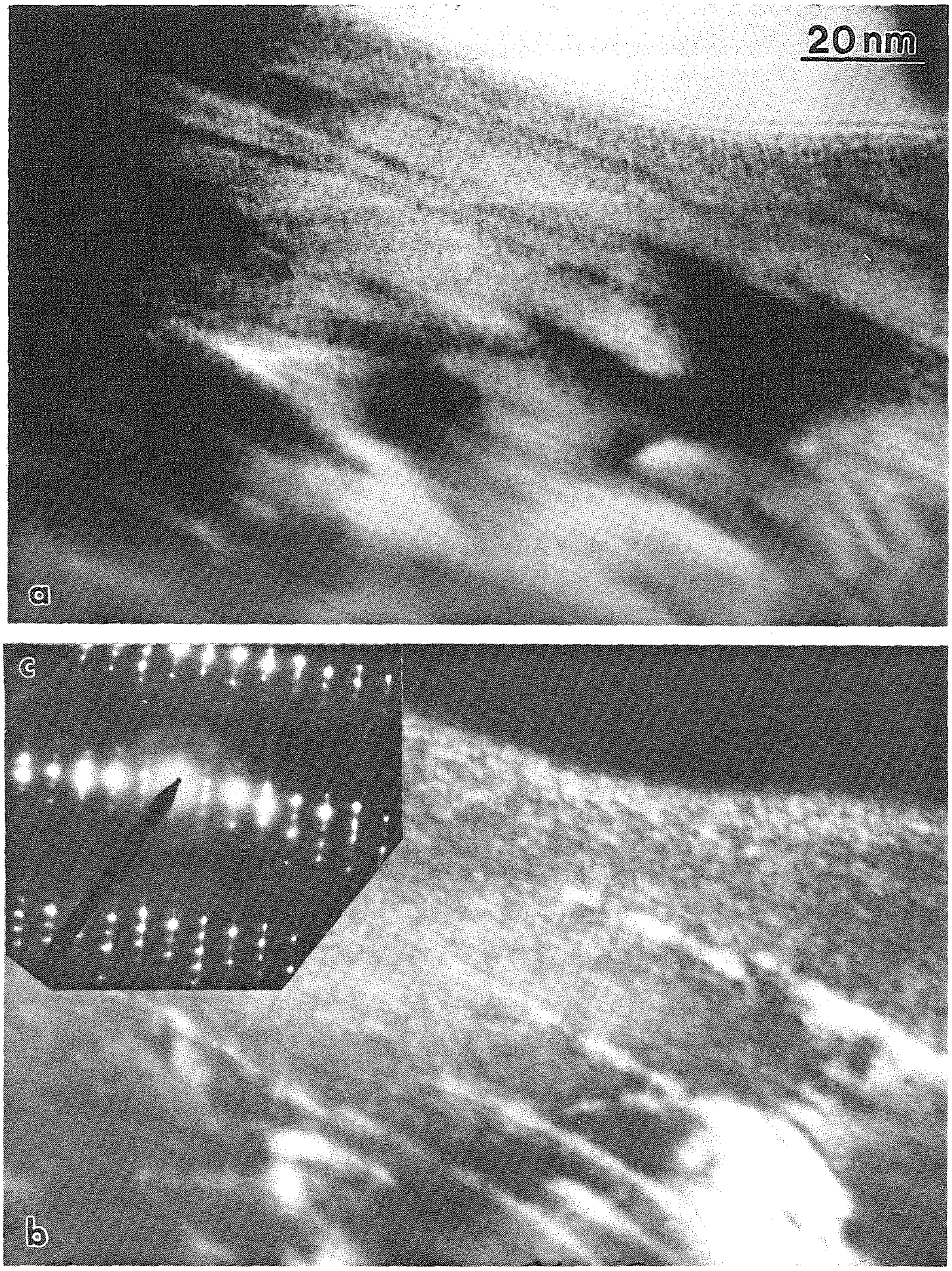

Figure 3.18. BF(a)/DF(b)/SAD(c) trio of a typical cross–section of the wear surface of Armacor–M^{TM}. Although there are few layers visible in the images, sharp superlattice spots are prominent in the SAD.

minimum twin size as 7.1 Å, in good agreement with the above numbers. Interestingly, very similar superlattice diffraction spot arrays have been observed to arise from periodic antiphase boundary structures in CuAu II.[3.14] A series of tilting and high–resolution TEM experiments should be done to determine whether or not the layers are semi–regular arrays of twins, or perhaps antiphase boundaries, and if they are effectively two dimensional sheets, which might obscure the image of the layered structure (as in Figure 3.18) if they are oriented differently with respect to the electron beam.

If twinning continues, eventually all layers would range from 8–15 Å. At this point, twins can no longer be formed, and deformation would have to be accommodated in some other way. This may result in the ultra–fine structure shown in the high–resolution micrographs in Figure 3.16. Note that the majority of the lattice fringes appear to be aligned in the same general direction. In fact, many of the fringes seem to extend over large areas of the sample, wavering slightly in direction and interrupted by small areas of disorder. The fringes are spaced 2 Å apart, which most closely matches the [112] planar spacing of 1.94 Å. Because even the smallest selected–area aperture is too large to exclude the region of larger crystals immediately below the surface fringe structure, the SAD pattern in Figure 3.15c contains typical polycrystalline rings, even though the sample is clearly textured.

It was thus necessary to examine the aligned fringe region using optical diffractogram analysis. A Fraunhofer diffraction pattern was obtained by shining a helium–neon laser through the TEM negative which had been used to produce Figures 3.15 and 3.16. The laser and the negative were mounted on an optical bench. Figure 3.19a contains the optical diffractogram of the fringe

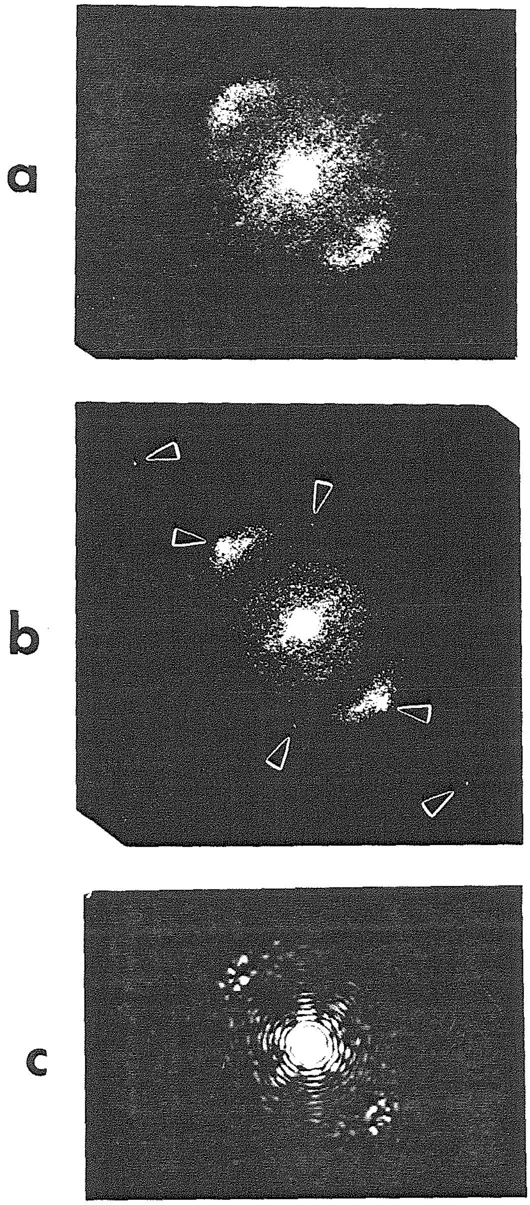

Figure 3.19. Optical diffractograms taken from the micrograph negative which was used to print Figures 3.15 and 3.16. (a) Surface fringe area, effective incident beam spot size 125 Å. (b) Polycrystalline region, 125 Å beam spot size; the arrows mark sharp diffraction spots from the crystals. (c) Surface fringe area, 27 Å beam spot size; the circular noise spectrum implies that there is little or no astigmatism present.

area; the incident beam diameter is equivalent to 125 Å. There is what appears to be a very highly textured amorphous ring visible. In fact, the pattern closely resembles one obtained from a micrograph of an amorphous sample containing a small amount of specimin drift.[3.15] However, close examination of the TEM micrograph reveals sharp cross fringes in the polycrystalline region, eliminating that possibility. Also, there is more structure observed in the bands than is present in those obtained from an amorphous sample with drift. For comparison, a diffractogram of the polycrystalline region is shown in Figure 3.19b. The arrows mark the sharp diffraction spots present. Note that there are spots present in the broad bands as well; these do not appear in any pattern taken of the fringe area. A diffractogram of the fringe region taken with an effective incident beam size of 27 Å is presented in Figure 3.19c. The circular noise spectrum visible in the center of the diffractogram confirms that the fringes visible in the micrograph are not due to astigmatism.[3.15]

The structure depicted in Figure 3.16b appears very similar to the region between a glass and a crystal that Luzzi and Meshii observed in electron irradiated Cu_4Ti_3.[3.16] They also found texture in this "mixed state", and proposed that amorphization occurs gradually, with local regions rotating slightly to accommodate lattice distortions induced by chemical disorder. A similar mechanism may account for the present observations, except the lattice distortions and chemical disorder in this case are produced by deformation. In the pictured region, the alignment of the lattice fringes implies that shear has occurred in one direction. Local atomic regions might possibly accommodate deformation by rotation in the shear direction. This would, in effect, be destroying long range order in one dimension. Remaining nanocrystalline areas would shift slightly in response to the local strains, causing the waviness in fringe direction. The sample here might thus not be thought of as strictly nanocrystalline, in the sense of having individual grains separated by grain boundaries, but as a mixture of ordered and disordered regions on a nanometer scale.

Although what might constitute a unit of local atomic rotation is not yet known, it may have something to do with chemical short–range order (CSRO). In Figure 3.10c, as well as Figures 2.17 and 2.13 which contain pictures of the rolled samples, there is an amorphous halo present that occurs inside the first polycrystalline ring. This may simply be due to an oxide; however, given its well–defined structure, it may in fact be related to the "prepeak" which Sakata et al. observed in neutron diffraction patterns of Cu–Ti glasses.[3.17] In amorphous $Cu_{35}Ti_{65}$ they found that 98% of the total structure factor was due to chemical composition fluctuations; the prepeak is the most intense peak in the pattern. At this composition the prepeak occurs at a scattering vector of approximately 2.1 $Å^{-1}$, which is in excellent agreement with the value of 2.0 $Å^{-1}$ obtained from Figure 3.10c. They correlated this prepeak with CSRO occurring at interatomic distances greater than the first nearest neighbor distance of about 3 Å. Perhaps chemically ordered clusters of atoms with an average radius on this scale are what rotate to accommodate additional deformation.

It is possible that the observed nanoscale mixture could be considered "amorphous"; lattice fringes are commonly seen in high–resolution micrographs of metallic glasses.[3.18,3.19] Given the preponderance of fringes present, however, it is perhaps more likely to be an early stage of, or a metastable precursor to, the amorphous phase. Luzzi et al. present evidence of there being different degrees of amorphization.[3.20] They irradiated CuTi at different stoichiometries and monitored the amorphization reaction with TEM. Although strain contrast in the image vanished in two cases, implying destruction of the crystal lattice, the diffraction patterns were different. In one case the pattern consisted of a broadened ring occurring at the same position as the nearest fundamental lattice reflection. In the second case, the amorphous halo is much broader, and the commonly seen second amorphous band is present. Amorphization may thus be a continuous process. In early stages, perhaps the "mixed state" of Luzzi and Meshii, the amorphous phase (or ordered regions therein) retains some "memory" of the original crystal, and the diffraction halo is close to the crystalline rings. At the earliest stages, and at the smallest scales, texture would still be present. In the later stages, amorphization is complete and the halo covers a wider extent. The volume fraction of ordered areas is minimized, and texturing disappears.

In other areas of the wear sample, there are other indications that amorphous material may be present. There is a broad diffraction halo in Figure 3.14c, and the accompanying images imply the structure consists of nanocrystals in an amorphous matrix. The nanocrystals that light up in dark field are on the order of 10 Å in size, which is the same size seen for contiguous fringe regions in Figure 3.16b. Also, the images in Figures 3.9 and 3.10 contain large regions that do not change contrast when going from bright–field to dark–field imaging, typical of a glass. However, the dark–field pictures clearly show that all of the microcrystals do not correspond to those visible in bright–field. Thus some of the "gray" areas consist of microcrystalline material.

From the above evidence it is probable that in certain areas of the wear surface there is glass present; if so, however, it would seem that complete amorphization occurs only rarely during wear. Although surface damage is more extensive than simple deformation, it is still on average not as dramatic as that which occurs during ball milling. It may be that a glass is formed only in the local areas where fracture and cold welding have happened and deformation occurs in a different direction. In that case, when grain size is small enough, long range order in at least two dimensions would be lost, and the material could then be considered amorphous. Thermodynamically speaking, once the grain boundary sliding and twinning modes of deformation are bypassed, the large grain boundary concentration and high degree of chemical disorder may raise the free energy of the nanocrystals such that further deformation makes local, perhaps unidirectional, amorphization energetically favorable.

CHAPTER FOUR: Conclusions

Mechanically induced amorphization of $CuTi_2$ has been examined by the methods of cold–rolling and wear. In the rolling experiments it was found that amorphization occurred when the sample morphology consisted of microcrystals in a glassy matrix. Polycrystalline samples did not amorphize. This is thought to be due to two mechanisms: there is no need to nucleate the amorphous phase at the crystal–glass interface, and the presence of the glass delays fracture, allowing the crystals to be deformed to a greater degree.

For future work, it is important that the nature of the diffuse scattering be examined. It would be useful to study samples with very low amounts of deformation in order to observe individual defects such as dislocations and antiphase boundaries. It may be possible to correlate the amount of deformation with the interfacial area of the antiphase boundaries created, and thus estimate how much enthalpy is stored. This would give a critical amount of deformation, below which amorphization cannot occur.

Because only crystals surrounded by an amorphous matrix amorphize during rolling, it may be useful to try to find a good glass forming system in which one of the components has an anomalously high grain boundary diffusion rate at low temperatures. If this component could saturate the grain boundaries without undergoing too much long range diffusion into the bulk, and the grain boundary concentration is high enough, an amorphous phase at the grain boundaries could be formed by a solid state reaction, with the resulting microstructure approximating the desired one.

In the wear experiments, an unusual phase was formed at the surface, consisting of a nanoscale mixture of textured crystalline regions and disordered areas. It is thought that this is a precursor to amorphization, or even an early stage thereof. It is of great interest to study the nature of the disorder that exists in this phase. A series of tilting experiments could be performed to determine whether or not the disorder is in fact only in one dimension. Correlating this direction with the direction of shear may shed light on exactly which mechanism is reponsible for accommodating deformation on these scales. In addition, if complete amorphization does occur when a particle experiences more than one direction of shear, then it would be useful to attempt to wear the sample perpendicularly to the original wear scar. This would presumably increase the fraction of completely amorphous material present at the surface.

In order to examine the status of the observed nanoscale structure with respect to the glass, standard friction and wear tests could be performed to measure any difference in the wear rate or the coefficient of friction between the structure presently observed and a fully amorphous phase, if it is possible to form both in large quantities at the wear surface. In addition, a series of experiments could be done *in–situ* with the heating stage in the electron microscope to determine whether or not the nanoscale structure is actually amorphous. At temperatures below T_x the structure, if amorphous, should relax into a more familiar glassy phase (with fewer lattice fringes, and no texture). If it is instead nanocrystalline, grain growth should occur without nucleation. At higher temperatures, nucleation as well as growth of crystals should be observed if the phase had originally been amorphous.[4.1]

Finally, in all amorphization experiments that involve deformation, including rolling, wear, and ball milling, it is important to study the effect of strain rate on the defect structures that are created. At the relatively low strain rates that both rolled samples and subsurface wear crystals undergo, the deformation produces structures whose diffraction patterns display diffuse scattering along the close–packed planes. This was not observed at the wear surface, which experiences higher strain rates. In $CuTi_2$, the beginnings of a polycrystalline ring pattern were seen instead. There may thus be at least two paths leading toward amorphization that a deformed crystal can take, depending on the strain rate it experiences. It would be interesting to ball mill powders of intermetallics that initially contain very large grains. Single crystal SAD patterns taken at very early stages of processing might show whether the relatively high strain rates give rise either to diffuse scattering or to polycrystalline rings, or to both. There is clearly much work that can be done to examine the stages a crystal undergoes during deformation–induced amorphization.

APPENDIX A: Derivation of the TTT Curve

The TTT curve is derived in detail as follows,[1.8] using classical nucleation theory. The free energy of formation of a spherical crystalline nucleus of radius r is comprised of both volume and surface energy terms. In other words, $\Delta G = -\frac{4}{3}\pi r^3 \Delta G_v + 4\pi r^2 \gamma$, where ΔG_v is the free energy per unit volume and γ is the solid–liquid interfacial free energy per unit area. Near the melting point,

$$\Delta G_v = L - T\Delta S \approx L - T\left[\frac{L}{T_m}\right] = L\frac{\Delta T}{T_m},$$

where L is latent heat of fusion per unit volume, T_m is the melting temperature, and $\Delta T = T_m - T$ is the undercooling. The critical radius is defined as the smallest radius for which the nucleus is stable. This occurs at the minimum of the free energy, i.e., where $\partial \Delta G / \partial r = 0$. Solving for r,

$$r^* = \frac{2\gamma T_m}{L\Delta T}, \text{ giving } \Delta G^* = \frac{16\pi\gamma^3 T_m^2}{3L^2 \Delta T^2}$$

as the free energy of formation for a stable nucleus. As is common with processes associated with an activation energy, the number of nuclei per unit volume is given by

$$n^* = n \cdot \exp\left[-\frac{\Delta G^*}{k_b T}\right],$$

where n is the total number of atoms (nucleation sites) per unit volume. The nucleation rate I is just n* times the frequency of atomic collisions with the (barely) sub–critical nucleus. Thus

$$I = \alpha \cdot \exp\left[-\frac{\Delta G_m + \Delta G^*}{k_b T}\right],$$

where α includes the atomic vibrational frequency, the number of surface atoms of the nucleus, a jump direction probability, and n. ΔG_m is the activation energy for atomic migration. For a constant growth rate ν, the Avrami equation gives the volume fraction f of transformed material as the following: $f = 1 - \exp\left[-\frac{\pi}{3} I \nu^3 t^4\right]$. The choice of f is arbitrary; if it is small enough, then one can write $f \approx \frac{\pi}{3} I \nu^3 t^4$. Therefore, the TTT curve can be plotted using the equation $\ln t = \frac{1}{4}\ln\frac{3f}{\pi} - \frac{3}{4}\ln\nu - \frac{1}{4}\ln I$, or

$$\ln t = \frac{1}{4}\ln\left[\frac{3f}{\pi\alpha}\right] - \frac{3}{4}\ln\nu + \frac{1}{T}\left(\frac{\Delta G_m}{4k_b} + \left[\frac{4\pi\gamma^3 T_m^2}{3k_b L^2}\right] \cdot \frac{1}{\Delta T^2}\right).$$

One must not neglect to include the temperature dependence of ν, given by[1.8]

$$\nu \propto \exp\left[-\frac{\Delta G_j}{k_b T}\right] \cdot \left(1 - \exp\left[-\frac{\Delta G_{l-x}}{k_b T}\right]\right),$$

where ΔG_j is the activation energy for an atomic jump across the growth interface, and ΔG_{l-x} is the liquid–crystal free energy difference.

REFERENCES

Chapter One

1.1 P. Chaudhari, B.C. Giessen, and D. Turnbull, *Sci. Amer.* **242**, 98 (April 1980).

1.2 W. Buckel and R. Hilsch, *Z. Phys.* **138**, 109 (1954).

1.3 P. Duwez, R.H. Willens, and W. Klement Jr., *J. Appl. Phys.* **31**, 1136 (1960).

1.4 H.A. Davies, in *Amorphous Metallic Alloys*, F.E. Luborsky, ed., Butterworths (1983), p. 8.

1.5 C.J. Lin, F. Spaepen, and D. Turnbull, *J. Non–Cryst. Sol.* **61** & **62**, 767 (1984).

1.6 M.H. Cohen and D. Turnbull, *Nature* **189**, 131 (1961).

1.7 M.G. Scott, in F.E. Luborsky, ed., *op. cit.*, p. 144.

1.8 D.A. Porter and K.E. Easterling, *Phase Transformations in Metals and Alloys*, Van Nostrand Reinhold Co. (1981), pp. 135–290.

1.9 X.L. Yeh, K. Samwer, and W.L. Johnson, *Appl. Phys. Lett.* **42**, 242 (1983).

1.10 R.B. Schwarz and W.L. Johnson, *Phys. Rev. Lett.* **51**, 415 (1983).

1.11 W.L. Johnson, *Prog. Mater. Sci.* **30**, 81 (1986).

1.12 A.R. Miedema, *Philips Tech. Rev.* **36**, 217 (1976).

1.13 M. Atzmon, K.M. Unruh, and W.L. Johnson, *J. Appl. Phys.* **58**, 3865 (1985).

1.14 C.C. Koch, O.B. Cavin, C.G. McKamey, and J.O. Scarbrough, *Appl. Phys. Lett.* **43**, 1017 (1983).

1.15 R.B. Schwarz, R.R. Petrich, and C.K. Saw, *J. Non–Cryst. Sol.* **76**, 281 (1985).

1.16 C. Politis and W.L. Johnson, *J. Appl. Phys.* **60**, 1147 (1986).

1.17 P.R. Okamoto and M. Meshii,in *Science of Advanced Materials*, Wiedersich and M. Meshii, eds., ASM International, in press.

1.18 J.L. Brimhall, H.E. Kissinger, and L.A. Charlot, *Rad. Eff.* **77**, 273 (1983).

1.19 D.E. Luzzi, H. Mori, H. Fujita, and M. Meshii, *Acta Metall.* **34**, 629 (1986).

1.20 R.C. Birtcher and T.H. Blewitt, *J. Nucl. Mater.* **69 & 70**, 783 (1978).

1.21 E.V. Kozlov, et al., in *Order–Disorder Transformations in Alloys*, H. Warlimont, ed., Springer–Verlag (1974), p. 58.

1.22 M.W. Thompson, *Defects and Radiation Damage in Metals*, Cambridge University Press (1969), p. 76.

1.23 E.P. Butler and J.F. Orchard, in *Phase Stability During Irradiation*, J.R. Holland, L.K. Mansur, and D. Potter, eds., AIME (1981), p. 315.

1.24 R.B. Schwarz, et al., *J. Less–Comm. Met.* **140** (1988), p. 171; also *Appl. Phys. Lett.* **49**, 146 (1986).

1.25 Y. Seki and W.L. Johnson, in *Solid State Powder Processing*, A.H. Clauer and J.J. deBarbadillo, eds., The Minerals, Metals & Materials Society (1990), p. 287.

1.26 Y. Abe, private communication.

1.27 D.E. Luzzi, H. Mori, H. Fujita, and M. Meshii, *Scripta Metall.* **18**, 957 (1984).

1.28 D.E. Luzzi, H. Mori, H. Fujita, and M. Meshii, in *Proc. Symp. on Beam–Solid Interactions and Phase Transformations, Boston, MA, December 1985*, G.L. Olson and J.M. Poate, eds., vol. 51, Materials Research Society, Pittsburgh, PA (1986), p. 479.

1.29 N.S. Stoloff, *Int. Met. Rev.* **29**, 123 (1984).

1.30 G. Vanderschaeve and A. Faress, in *Proc. 43rd Ann. Meeting Elec. Mic. Soc. Amer.*, G.W. Bailey, ed., San Francisco Press (1985), p.344.

1.31 M.J. Sabochick and N.Q. Lam, *Scripta Metall.* **24**, 565 (1990).

1.32 M.L. Trudeau, R. Schulz, D. Dussault, and A. Van Neste, *Phys. Rev. Lett.* **64**, 99 (1990).

1.33 J. Eckert, L. Schultz, E. Hellstern, and K. Urban, *J. Appl Phys.* **64**, 3224 (1988).

1.34 C.H. Lee, M. Mori, T. Fukunaga, and U. Mizutani, *Jap. J. Appl. Phys.* **29**, 540 (1990); also *Mater. Sci. & Eng.* **A134**, 1334 (1991).

1.35 M.B. Bever, D.L. Holt, and A.L. Titchener, *Prog. Mater. Sci.* **17**, 1 (1973).

1.36 J.E. Bailey and P.B. Hirsch, *Phil. Mag.* **5**, 485 (1960).

1.37 B. Roessler and M.B. Bever, *Tran. Met. Soc. AIME* **221**, 1049 (1961).

1.38 T.B. Massalski, ed., *Binary Alloy Phase Diagrams*, 2nd ed., ASM International, Metals Park, OH (1990), p. 1495.

1.39 J.L. Murray, *Bull. Alloy Phase Diagrams* **4**, 81 (1983).

1.40 P.J. Desré and A.R. Yavari, *Phys. Rev. Lett.* **64**, 1533 (1990).

Chapter Two

2.1 B.P. Bewlay and B. Cantor, *Int. J. Rapid Solidification* **2**, 107 (1986).

2.2 M. Atzmon, K.M. Unruh, and W.L. Johnson, *J. Appl. Phys.* **58**, 3865 (1985).

2.3 G. Dieter, *Mechanical Metallurgy*, McGraw–Hill (1976), pp. 626–7.

2.4 B.D. Cullity, *Elements of X–Ray Diffraction*, 2nd ed., Addison-Wesley, Reading, MA (1978), pp. 292–3.

2.5 B.D. Cullity, *op. cit.*, pp. 13, 189.

2.6 E. Vogt and G. Frommeyer, in *Rapidly Quenched Metals*, S. Steeb and H. Warlimont, eds., Elsevier (1985), p. 63.

2.7 C.G. Woychik and T.B. Massalski, in S. Steeb and H. Warlimont, *op. cit.*, p. 207.

2.8 P. Delavignette, in *Electron Microscopy 1982, Proc. Tenth Int. Cong. Elec. Micr.*, Deutsche Gesellschaft fur Elektronmikroskopie eV, Frankfurt (1982), p. 201.

2.9 J.L. Murray, *Bull. Alloy Phase Diagrams* **4**, 81 (1983).

2.10 E.A. Kamenetzky, P.D. Askenazy, L.E. Tanner, and W.L. Johnson, in *Proc. Symp. on Science and Technology of Rapidly Quenched Alloys, Boston MA, December 1986*, M. Tenhover, L.E. Tanner, and W.L. Johnson, eds., Vol. 80, Materials Research Society, Pittsburgh, PA (1987), p. 83.

2.11 D.E. Luzzi, H. Mori, H. Fujita, and M. Meshii, *Scripta Metall.* **18**, 957 (1984).

2.12 C Barrett and T.B. Massalski, *Structure of Metals*, Pergamon Press (1980), p. 404.

2.13 D.E. Luzzi, H. Mori, H. Fujita, and M. Meshii, *Acta Metall.* **34**, 629 (1986).

2.14 D.E. Luzzi, H. Mori, H. Fujita, and M. Meshii, in *Proc. Symp. on Beam–Solid Interactions and Phase Transformations, Boston, MA, December 1985*, G.L. Olson and J.M. Poate, eds., vol. 51, Materials Research Society, Pittsburgh, PA (1986), p. 479.

2.15 H. Jones, *Mater. Sci. and Eng.* **65**, 145 (1984).

Chapter Three

3.1 D. Landheer and A.W.J. de Gee, *MRS Bulletin* **16**, 36 (October 1991).

3.2 D.A. Rigney, L.H. Chen, M.G.S. Naylor, and A.R. Rosenfield, *Wear* **100**, 195 (1984).

3.3 T.F.J. Quinn, *Physical Analysis for Tribology*, Cambridge University Press (1991), pp. 336–359.

3.4 D.A. Rigney, *Ann. Rev. Mater. Sci.* **18**, 141 (1988).

3.5 J.J. Wert, F. Srygley, D.D. Warren, and R.D. McReynolds, *Wear* **134**, 115 (1989).

3.6 N. Jost and I. Schmidt, *Wear* **111**, 377 (1986).

3.7 S.K. Ganapathi and D.A. Rigney, *Scripta Metall.* **24**, 1675 (1990).

3.8 D.G. Morris, in *Rapidly Quenched Metals*, S. Steeb and H. Warlimont, eds., Elsevier (1985), p. 1775.

3.9 K. Miyoshi and D.H. Buckley, *Wear* **110**, 295 (1986).

3.10 H.S. Carslaw and J.C. Jaeger, *Conduction of Heat in Solids*, Oxford University Press (1959), pp. 20, 135.

3.11 P.J. Blau, *J. Tribology (Trans. ASME)* **107**, 483 (1985).

3.12 B.D. Cullity, *Elements of X–Ray Diffraction*, 2nd ed., Addison-Wesley, Reading, MA (1978), pp. 292–3.

3.13 D. Hull and D.J. Bacon, *Introduction to Dislocations*, Pergamon Press (1984), pp. 124–5, 208.

3.14 P. Hirsch, A.Howie, R.B. Nicholson, D.W. Pashley, and M.J. Whelan, *Electron Microscopy of Thin Crystals*, Robert E. Krieger Publishing Company, Malabar, Florida (1977), pp. 382–6.

3.15 P.R. Buseck, J.M. Cowley, and L. Eyring, eds., *High–Resolution Transmission Electron Microscopy and Associated Techniques*, Oxford University Press, New York (1992), pp. 543–9.

3.16 D.E. Luzzi and M. Meshii, *J. Mater. Res.* 1, 617 (1986).

3.17 M. Sakata, N. Cowlam, and H.A. Davies, in *Proc. 4th Int Conf. on Rapidly Quenched Metals, Sendai, Japan, 1981*, T. Masumoto and K. Suzuki, eds., Japan Institute of Metals, Sendai, Japan (1982), p. 327.

3.18 J.C. Barry, R.S. Timsit, and D. Landheer, in *Proc. 44th Ann. Meeting Elec. Micr. Soc. Amer.*, G.W. Bailey, ed., San Francisco Press (1986), p. 860.

3.19 J. Zweck and H. Hoffman, in *Rapidly Quenched Metals*, S. Steeb and H. Warlimont, eds., Elsevier (1985), p. 509.

3.20 D.E. Luzzi, H. Mori, H. Fujita, and M. Meshii, in *Proc. Symp. on Beam–Solid Interactions and Phase Transformations, Boston, MA, December 1985*, G.L. Olson and J.M. Poate, eds., vol. 51, Materials Research Society, Pittsburgh, PA (1986), p. 479.

Chapter Four

4.1 L.C. Chen and F. Spaepen, *Nature* **336**, 366 (1988).